Title
Synthesis and Characterization of Amorphous Carbon Films for Magnetic Storage Technology

Author
Xie, Jun

Publication Date
2015

Peer reviewed|Thesis/dissertation

Synthesis and Characterization of Amorphous Carbon Films for Magnetic Storage Technology

by

Jun Xie

A dissertation submitted in partial satisfaction of the

requirement for the degree of

Doctor of Philosophy

in

Engineering – Mechanical Engineering

in the

Graduate Division

of the

University of California at Berkeley

Committee in charge:
Professor Kyriakos Komvopoulos, Chair
Professor David B. Bogy
Professor Ron Gronsky

Fall 2015

Abstract

Synthesis and Characterization of Amorphous Carbon Films
for Magnetic Storage Technology

by

Jun Xie

Doctor of Philosophy in Engineering – Mechanical Engineering

University of California, Berkeley

Professor Kyriakos Komvopoulos, Chair

Increasing demands for high magnetic storage capacity have led to the increase of the recording area density, mainly by reducing the distance between the magnetic media on the hard disk and the magnetic transducer of the head. A factor that has greatly contributed to the profound decrease of the magnetic spacing is excessive thinning of the protective amorphous carbon (*a*-C) overcoat. However, the remarkable decrease in overcoat thickness raises a concern about its quality and protective capability. In general, *a*-C films with higher sp^3 carbon atom hybridization demonstrate higher density and better tribomechanical and corrosion properties. The sp^2 and sp^3 contents strongly depend on the film-growth conditions and deposition method.

One of the most common film deposition methods is radio-frequency (RF) sputtering. This method uses low-energy neutral carbon atoms or clusters of atoms as film precursors and has been the workhorse of storage technology for more than four decades. Typically, Ar^+ ion bombardment of the growing film during film growth is used to tailor the overcoat structure and properties without affecting its chemical environment. The substrate bias voltage is a key deposition parameter because it directly affects the ion bombardment energy. In this dissertation, the effect of the substrate bias voltage on the growth and properties of ultrathin *a*-C films was examined and the identified film structure-property interdependencies were explained in the context of an analytical model, which takes into account the effects of irradiation damage and thermal spikes.

Substrate biasing during film deposition may lead to some undesirable effects, such as the development of a high compressive residual stress, which can cause premature overcoat failure by delamination. Experimental studies of this dissertation show that alternating between biasing and non-biasing deposition conditions, multi-layer *a*-C films consisting of ultrathin hard (bias on) and soft (bias off) layers characterized by high sp^3 fraction and greatly reduced compressive residual stress can be synthesized by RF sputtering. An additional advantage is that these multi-layer *a*-C films exhibit lower surface roughness and improved tribological properties.

Different from deposition methods using neutral carbon atoms as film-forming precursors, such as RF sputtering and other physical vapor deposition methods, filtered cathodic vacuum arc (FCVA) uses energetic C^+ ions as film precursors, which is advantageous for depositing ultrathin and very smooth *a*-C films with superior nanomechanical/tribological properties. The role of important FCVA process parameters, such as substrate bias voltage, which controls the C^+ ion energy, in the film growth process were investigated, while considering various means of reducing the *a*-C film thickness without jeopardizing its structure and properties. The effect of the duty cycle of substrate pulse biasing (i.e., the ratio of the time of substrate biasing over a pulse to the pulse bias period) was examined in terms of film deposition rate, surface topography, and nanostructure. Cross-sectional high-resolution transmission electron microscopy (HRTEM) combined with the scanning transmission electron microscopy (STEM) and electron energy loss spectroscopy (EELS) studies revealed variations in through-thickness hybridization and density with duty cycle. *a*-C films with the highest sp^3 content and smallest thickness were synthesized under FCVA deposition conditions of 75% and 65% duty cycle, respectively.

EELS studies show that *a*-C films generally possess a multi-layered structure consisting of surface and interface layers of relatively low sp^3 contents and intermediate bulk layer of much higher sp^3 content, a result of the deposition mechanisms encountered during ion bombardment. When the *a*-C film thickness is reduced to only 2–3 nm, the effects of the ultrathin (1–2 nm) surface and interface layers become increasingly more pronounced, resulting in the decrease of the overall sp^3 content and, in turn, depletion of the film's protective capability. To reduce the thickness of the interface layer, a thin (<1 nm) seed carbon layer was deposited under small incidence angle and zero substrate bias to minimize the effect of C^+ ion subplantation, followed by deposition of an *a*-C film under optimal film-growth conditions resulting in high sp^3 content. The absence of substrate biasing during the initial deposition allowed the formation of a barrier between the substrate and the bombarding energetic C^+ ions. To reduce the thickness of the surface layer, post-deposition Ar^+ ion sputter etching of the synthesized *a*-C film was performed, which effectively sputtered off carbon material, reducing the thickness of the surface layer without degrading the sp^3 content of the bulk layer of the *a*-C film.

Heat-assisted magnetic recording (HAMR) is a relatively new storage technology showing great potential for further increasing the magnetic recording density. This technology utilizes a tightly focused laser beam to rapidly heat the media above the Curie temperature, temporarily reducing the coercivity of magnetic nanodomains such that the magnetic field of the read/write head can induce polarization changes. Among all other issues brought up by the HAMR technology, the thermal stability of the carbon overcoat is of great concern. In this dissertation, ultrathin hydrogenated amorphous carbon (*a*-C:H) and *a*-C films synthesized by plasma-enhanced chemical vapor deposition (PECVD) and FCVA, respectively, which are the prime deposition techniques used in current hard-disk drives, were subjected to rapid thermal annealing (RTA) of maximum temperature equal to 650 °C for 1 s. EELS results show structural changes in the PECVD *a*-C:H films involving carbon diffusion in the substrate and a decrease in sp^3 content; however, the FCVA *a*-C films show remarkable structural stability under the same RTA conditions, indicating that FCVA is an ideal film deposition process for HAMR technology.

Table of Content

List of Figures

(b) and (d) reveal the formation of crystalline nanodomains in the amorphous film structure.

Fig. 8.6 Depth distributions of normalized intensity of C-K edge and sp^3 content calculated from the C K-edge EELS spectra of ~60-nm-thick (a) single- and (b) multi-layer *a*-C films. Dashed lines indicate the boundaries between (i) Si(100) substrate, (ii) intermixing layer, (iii) bulk layer, (iv) surface layer, and (v) capping Au layer.

List of Tables

Chapter 1 Introduction

Carbon is one of the most fundamental elements and versatile materials in nature. It exists in both crystalline and disordered structure, forming from three different bonding states, i.e. tetrahedral (sp^3), trigonal (sp^2), and linear (sp^1). The most common carbon allotropes are graphite [Kelly, 1981] and diamond [Field, 1993]. With the relatively recent discoveries of C_{60} [Rohlfing et al., 1984], carbon nanotubes [Iijima, 1991], and graphene [Novoselov et al., 2004; Geim and Novoselov, 2007], carbon has become a popular research topic with direct application to various contemporary technologies, such as flexible electronics, carbon-based integrated circuits, and computer storage.

During the recent two decades, amorphous carbon (*a*-C) attracted significant attention because of its unique mechanical and tribological properties and high performance-to-cost ratio. In the absence of high temperature or high pressure, diamond-like carbon [Aisenberg and Chabot, 1971] or amorphic diamond [Collins et al., 1991; Collins et al., 1993; Davanloo et al., 1990; Davanloo et al., 1992] are alternative carbon forms possessing good mechanical properties.

One of the most common applications of *a*-C films is as protective overcoat of magnetic storage devices and microelectromechanical systems [Erdemir and Donnet, 2006; Chu and Li, 2006; Robertson, 2002] due to their high hardness and good wear resistance [Lu and Komvopoulos, 1999; Lu and Komvopoulos, 2001; Ma et al., 2003; Tsai and Bogy, 1987; Lifshitz, 1997; Robertson, 2002; Grill, 1999; Hauert, 2004]. The good properties of *a*-C originate from its unique nanostructure – the sp^2 bonding state controls the electrical and optical properties, while the sp^3 bonding state is responsible for the mechanical properties [Robertson, 2002; Diaz et al., 1996]. Carbon films with higher sp^3 content are generally harder and denser, which are important characteristics for wear and corrosion protection [McKenzie, 1996; Monteiro, 2001].

In hard-disk drives (HDDs), information is stored in the magnetic medium of the hard disk by the magnetic field of the read/write transducer embedded in the trailing edge of the flying head. To prevent damage at the head-disk interface due to intermittent asperity contact and corrosion, a continuous, smooth, ultrathin *a*-C film (overcoat) is deposited onto the magnetic head and disk surfaces [Kryder 2008, Yasui 2009]. Figure 1.1 shows a schematic of the cross-sectional structure of current HDDs. The hard disk has a multi-layer structure including glass/glass-ceramic substrate, layer of magnetic medium, *a*-C overcoat, and lubricant monolayer. The head consists of Al_2O_3-TiC ceramic (typically, 70/30 vol.%) and is also coated with a thin *a*-C overcoat for protection against corrosion, mechanical wear, and impact.

The increasing demands for high-capacity/low-cost HDDs have led to the dramatic increase of the magnetic storage density in recent years, mainly due to important breakthroughs in thin-film media and magnetic head designs [Bandic and Victora, 2008], such as giant magnetoresistance head [Baibich et al., 1988; Daughton et al., 1994], perpendicular magnetic recording [Khizroev et al., 1999], and also the profound decrease of the physical spacing [Wood et al., 2009; Anders et al., 2001], defined as the distance between the read/write element of the head to the magnetic

medium of the hard disk. According to Wallace's law, the magnetic storage density increases exponentially with the decrease of the physical spacing because the intensity of the magnetic field applied by the head increases exponentially with the decrease of the physical spacing. For instance, to achieve storage densities of 1 Tb/in^2, the physical spacing must be 6.5 nm [Yasui et al., 2009]. Thus, current demands for ultrahigh storage capacity necessitate a continuous and dense overcoat of thickness equal to ~2–3 nm.

The significant decrease of the overcoat thickness in next-generation HDDs raises serious concerns about the uniformity, structure, roughness, mechanical/tribological properties, and corrosion resistance of the overcoat, bringing more challenges in the deposition of ultrathin *a*-C films. The most widely used techniques of ultrathin film deposition are filtered cathodic vacuum arc (FCVA) [McKenzie et al., 1991; Fallon et al., 1993; Jungnickel et al., 1994; Silva et al., 1996], pulsed laser deposition [Kovarik et al.,1993; Voevodin and Donley, 1996], mass-selected ion beam (MSIB) deposition [Ishikawa et al., 1987; Lifshitz et al., 1990; Lifshitz et al., 1997], chemical vapor deposition (CVD) [Monteiro, 2001; Fung et al., 2000; Leng et al., 2000], and radio-frequency (RF) sputtering [Savvides and Window, 1985; Koening and Maissel, 1970; Coburn and Kay, 1972; Keller and Pennebake, 1979; Köhler et al, 1985; Lu and Komvopoulos, 1999; Wan and Komvopoulos, 2006]. Depending on the deposition technique, *a*-C films with different properties and nanostructure can be synthesized on various substrate materials.

Among the aforementioned deposition techniques, sputtering is the most widely used deposition technique for thin-film coating applications. This technique uses low-energy neutral atoms or clusters of atoms as film-forming precursors and has the advantages of low input energy, temperature and vacuum, making it a very efficient method for depositing thin films at low cost. The film properties can be tailored and controlled by bombarding the growing film surface with energetic inert ions. One of the important parameters that greatly affects the film properties is the substrate bias voltage, which directly controls the energy of inert ion bombardment on both the target and the substrate [Lu and Komvopoulos, 1999]. The effect of the substrate bias voltage on the hybridization and tribomechanical properties of sputtered *a*-C films is examined in Chapter 3 based on an analytical particle collision model accounting for Ar^+ ion and C atom interaction, preferential removal of weakly bonded carbon atoms, and the development of thermal spikes during film growth.

Unlike sputtering, which uses low-energy atoms as film-forming precursors, FCVA uses high-energy ions as film-forming precursors; therefore, FCVA is considered to be more effective method for synthesizing ultrathin (e.g., <5 nm), continuous, and smooth films. The bombardment of energetic ions enhances the density of the forming film. FCVA is currently the only demonstrated low-temperature deposition method for synthesizing hydrogen-free, ultrathin *a*-C films with high sp^3 content, good nanomechanical properties, and high wear resistance [Casiraghi, 2004(B); Beghi, 2002]. Because of the nature of energetic ion bombardment, the film deposited by FCVA always exhibits a layered structure with the top (surface) layer and bottom (interface) layer exhibiting relatively low sp^3 contents, which can be explained by the subplantation model [Lifshitz et al., 1989; Lifshitz et al., 1990; Robertson, 1994(B); Robertson, 1996; Hofsäss et al, 1998].

To further reduce the *a*-C film thickness, it is necessary to accordingly adjust a few process parameters, including the deposition time, arc discharge current, pulsed substrate bias voltage and duty cycle, and ion incidence angle. While decreasing the deposition time appears to be the most straightforward approach, the formation of the low-sp^3 surface and interface layers cannot be prevented. In fact, reducing the deposition time may result in overall lower sp^3 fraction because this will mainly reduce the thickness of the sp^3-rich bulk layer of the *a*-C film. In addition, plasma arcing takes some time to be stabilized and there is a minimum requirement for the arc current to successfully ignite the plasma. Increasing the substrate bias voltage is conducive to the formation of thin films because the high-energy C^+ ions sputter off atoms from the surface of the growing film. However, high ion energy could be detrimental to the integrity of the film structure because thermal relaxation commences in the high-energy region. A comprehensive examination of the duty cycle effect on the quality of FCVA *a*-C films, including the structure, composition, thickness, residual stress, and roughness, is presented in Chapter 4. The results presented in this chapter provide insight into the minimum thickness of *a*-C films that could be achieved by adjusting the FCVA deposition parameters.

It is, therefore, desirable to minimize the thickness of *a*-C overcoats under optimal deposition conditions. In view of the cross-sectional non-uniformity of *a*-C films (i.e., the surface and interface layer exhibit a gradient in sp^3 fraction and density that are both lower than those of the bulk layer), the objective is to reduce the thickness of the surface and interface layers, while maintaining the high sp^3 fraction in the bulk layer. The multi-layer film structure stems is a consequence of the deposition process. The low sp^3 content of the surface layer is due to less C^+ ion bombardment on the film surface during the end of deposition. Thus, the objective is to use inert (Ar^+) ion bombardment after film deposition to sputter off the surface layer without altering the chemical environment of the *a*-C film. The low-sp^3 intermixing layer is due to direct and recoil C^+ ion implantation into the substrate. Therefore, the objective here is to initiate film deposition under zero substrate bias to reduce the intermixing of C^+ ions with substrate atoms, subsequently turning on the substrate bias voltage to deposit under optimal conditions (i.e., energetic C^+ ions) sp^3-rich *a*-C film. With this two-step deposition technique, the thickness of intermixing layer can be controlled.

The investigation of the cross-sectional structure of ultrathin *a*-C films is challenging. First, diffraction techniques, such as X-ray diffraction, are inefficient because the amorphous film is lacking crystallinity. Second, any characterization method that has thickness sensitivity, such as X-ray reflectivity and nanoindentation, is limited because the film thickness is less than 2-3 nm. Third, techniques that only detect the overall film composition, such as X-ray photoelectron spectroscopy (XPS) and Raman spectroscopy, are not suitable because of the multi-layer film structure. Besides, when the film thickness is $\leq$3 nm, the XPS carbon signal intensity (C1s peak) and signal-to-noise ratio of the carbon signal in Raman (G and D peaks) are low, making data acquisition and analysis a challenging task. Therefore, in view of the aforementioned shortcomings, high-resolution transmission electron microscopy (TEM), spatial resolution scanning transmission electron microscopy (STEM), and electron energy loss spectroscopy (EELS) were used in this work to perform in-depth studies of the nanostructure of FCVA *a*-C films. The effect of post-deposition Ar^+ ion sputter etching and bilayer film deposition on the thickness and structure modification are examined in Chapters 5 and 6, respectively.

The competition from solid-state drives has increased the demand for higher capacity and lower cost HDD technologies. Beside the need to reduce the physical spacing discussed earlier, decreasing the magnetic grain size is also of high importance. However, as the domain size continues to shrink, thermal fluctuations could randomly flip the magnetic direction of the grain when k_BT becomes on the order of KV, where k_B is Boltzmann's constant, T is the temperature, K is the magnetic anisotropy energy density, and V is the volume, a phenomenon known as the superparamagnetic effect. Therefore, the further increase of the storage density by reducing the average size of magnetic domains is inhibited by the superparamagnetic limit. A promising solution to this problem is heat-assistant magnetic recording (HAMR), which uses a laser-optical system integrated into the magnetic head to locally heat the fine grains of the magnetic medium above its Curie temperature (defined as the temperature at which the material loses its permanent magnetic properties), enabling the magnetic field of the head to accordingly polarize individual bits. Rapid cooling of the laser-heated medium restores the high coercivity, locking the induced magnetization of the grains.

The new HAMR technology brings up new issues. One of them is whether the *a*-C overcoat can withstand high temperature rises and remain stable under the envisioned laser heating conditions. The mechanical and tribological properties of the *a*-C overcoat may be attenuated if it undergoes oxidation, graphitization ($sp^3 \rightarrow sp^2$ rehybridization), carbon loss, or other structure changes, which can negatively impact the overcoat's protection capability. Therefore, the thermal stability of the *a*-C film is of high importance. However, because the laser heating time is on the order of a few nanoseconds and the laser spot is <100 nm, direct measurement of the temperature rise and *in-situ* characterization of changes in the film properties is difficult, if not impossible. As an alternative, rapid thermal annealing is used to examine the structural stability of *a*-C films deposited by plasma enhanced chemical vapor deposition (PECVD) and FCVA in Chapter 8. The results reveal significant differences in the structural stability of carbon overcoats deposited by PECVD and FCVA.

In addition to the HDD technology, thin *a*-C films are also used in other technologies. For example, *a*-C films are used as coating materials in total joint replacements and cardiovascular implants because of their unique tribological properties, good biocompatibility, and hemocompatibility [Hauert, 2008]. One of the problems with relatively thick *a*-C films is the development of a high compressive residual stress during deposition due energetic ion bombardment, which may lead to film delamination, buckling, agglomeration, or other modes of failures [Ohring, 1992; Lu and Komvopoulos 2001; Srolovitz, 1995]. Therefore, controlling the evolution of intrinsic stresses during film growth and depositing relatively thick, hard, and smooth films are of great importance. Several methods can be used to reduce residual stresses. Common methods include post-deposition thermal annealing, implantation of foreign elements in the amorphous matrix, modification of the bonding structure, and deposition of alternating hard and soft layers of the film material to reduce the extend of energetic ion bombardment. In Chapter 8, a multi-layer structure containing alternating hard and soft *a*-C layers is analyzed in light of tribomechnical properties (coefficient of friction), cross-sectional structure, and residual stress results.

The main objectives of this dissertation are to investigate the nanostructure and mechanical/topographical properties of ultrathin *a*-C films used in magnetic storage devices, and evaluate their efficacy and stability as protective overcoats for the HAMR technology.

The dissertation is organized as following:

Chapter 1 introduces the background and the motivation of this dissertation, in the context of protective *a*-C overcoats for high-capacity HDDs, with main requirements very small thickness, high smoothness, continuity, good tribomechanical properties, and thermal stability.

Chapter 2 provides an overview of the *a*-C film deposition methods and characterization techniques used in the experimental studies of this dissertation.

Chapter 3 is devoted to the synthesis of thin *a*-C films under low-pressure RF sputtering conditions of varying substrate bias voltage in pure Ar atmosphere. The surface roughness and tribomechanical properties of the *a*-C films were measured with an atomic force microscope (AFM) and a surface force microscope (SFM). Insight into sp^3 and sp^2 hybridization was obtained from the deconvoluted C1s core-level XPS peak. Energetic particle collision theory was used to correlate hybridization and tribomechanical properties to low-pressure plasma discharge conditions, including the Ar^+ ion flux, sputtering yield of target carbon atoms, and kinetic energy of surface carbon atoms.

Chapter 4 provides insights into the duty cycle of substrate pulse biasing effect on the structure (hybridization), thickness, residual stress, and roughness of *a*-C films deposited by FCVA in the light of HRTEM, cross-sectional EELS, Raman spectroscopy, residual stress, and AFM measurements. It is shown that the optimum duty cycle of pulsed substrate biasing yields the best quality *a*-C films that combine smoothness, ultra-small thickness, and high sp^3 content. The results presented in this chapter are of critical importance to the longevity and reliability of HDDs.

Chapter 5 shows how post-deposition Ar^+ ion sputter etching can be used to reduce the thickness of the sp^2-rich surface layer, while maintaining the sp^3 fraction and thickness of the bulk layer of carbon films deposited by PECVD and FCVA. The results show that the *a*-C films deposited by FCVA exhibit a smaller thickness reduction of both surface and intermixing layers compared with PECVD films. The sp^3 fraction and thickness in the bulk layer can be maintained for a certain time of Ar^+ ion sputter etching. A further increase of the etching time may negatively impact the sp^3 content and thickness of bulk layer of the overcoat.

Chapter 6 is focused on the synthesis of bilayer *a*-C films and the decrease of the thickness of the intermixing layer to improve the uniformity of the cross-sectional film structure. TEM and EELS were used to identify cross-sectional structure changes of ultrathin *a*-C films deposited by FCVA. The results show that bilayer *a*-C film deposition is an effective method for reducing the thickness of the intermixing layer and increase the thickness of the bulk layer, while retaining its desirable properties, such as high sp^3 content.

Chapter 7 presents a TEM/EELS study of the effect of rapid thermal annealing on the structure of hydrogenated amorphous carbon (*a*-C:H) and *a*-C ultrathin films deposited by PECVD and FCVA, respectively. It is shown that FCVA *a*-C films demonstrate superior thermal stability compared with PECVD *a*-C:H films. Therefore, FCVA *a*-C films are prime candidates for protective overcoats in applications where rapid heating is of concern, such as HAMR technology.

Chapter 8 illustrates how the multi-layer structure of *a*-C films deposited by alternating between on and off substrate bias voltage can effectively reduce the film roughness and coefficient of friction. Moreover, it is shown that the overall residual stress in the multi-layer *a*-C film is significantly reduced without affecting the sp^3 content compared to a single-layer *a*-C film of similar thickness deposited under optimum FCVA deposition conditions.

Chapter 9 summarizes the main findings of this dissertation.

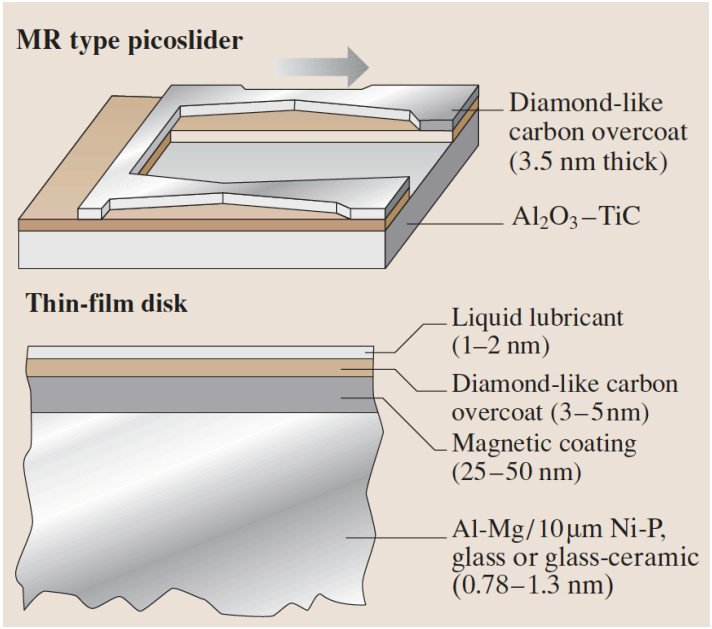

Fig. 1.1 Cross-sectional architecture of contemporary HDDs [Bhushan, 2010].

Chapter 2 Experimental procedure

2.1 Introduction

Greatest efforts of this dissertation have been made on the experimental studies of the ultrathin *a*-C films. Experimental work is the base and value of this dissertation. Film deposition techniques, such as RF sputtering, FCVA and PECVD, and film characterization techniques, such as AFM, XPS, Raman spectroscope, triboscope, TEM and EELS, are used in multiple parts of this dissertation. Therefore, an introduction of the techniques in general in this chapter is essential and important.

2.2 Carbon film deposition technique

It is possible to produce *a*-C film by a wide range of deposition techniques. Based on the deposition mechanisms, they can be divided into two different catalogues. One is physical vapor deposition (PVD), and chemical vapor deposition (CVD). The differences lie in the fact that in CVD process, films are formed by chemical reactions on the surface of the substrate while in PVD process, films are formed by ions/atoms from sources directly. PVD processes can further be categorized as to what kinds of elements that form the film: highly energetic ions or low energy neutral atoms as film forming precursor.

Different deposition methods and parameters will result in *a*-C films with various structure and properties. The main focus will be on the rf sputtering, FCVA, and PECVD deposition techniques. Other deposition methods will be briefly introduced.

2.2.1 Radio-frequency (RF) Sputtering

Sputtering techniques are widely used to deposit thin films of various thickness ranging from a few to hundreds of nm. Low pressure radio-frequency sputtering [Savvides & Window, 1985; Koening & Maissel, 1970; Coburn & Kay, 1972; Keller & Pennebake, 1979; Köhler et al., 1985] uses graphite target as the carbon source with the bombardment of Ar+ ion plasma. The inert ions strike the graphite target and knock out the carbon atoms by momentum transfer. Then the carbon atoms or cluster of atoms with low kinetic energy on the order of a few eV to tens eV travel through the chamber and finally deposit onto the substrate surface. In the meantime, the ions can be accelerated through the chamber from target by applying a negative substrate bias voltage. By controlling the absorbed rf power, substrate bias voltage, deposition time, working pressure, and flow rate of process gas, ultrathin a-C films with sp^3 contents higher than 50 at% and nanohardness of ~39 GPa can be synthesized under optimum rf sputtering conditions [Lu and Komvopoulos 1999].

A Perkin-Elmer Randex-2400 model low-pressure sputtering system without magnetron shown schematically in Fig 2.1. The plasma is excited and maintained by a rf power supply through a rf

coupling coil and capacitive tuning network shown in Fig 2.2. The substrate bias voltage is applied by the bias tuning technique and the target is negatively self-biased. The geometry of the chamber in the system is symmetric, with the target surface area equal to the substrate area, both is 20 cm in diameter. The spacing between the target and substrate electrodes is 7 cm. During the Ar gas discharge, the chamber is pumped down to a low base pressure ~2×10^{-6} Torr (measured by a Granville-Philips ion gauge) to remove any residual gases adsorbed onto the chamber walls. The temperature of target and substrate are maintained at room temperature by water cooling. The working pressure is adjusted by a throttle valve and the gas flow rate is adjusted by MKS flow ratio controller. Because of the impedance mismatch between the rf power supply and the plasma, the absorbed power, which sustains the discharge is not equal to the forward power, and the difference is the reflected rf power.

2.2.2 Filtered cathodic vacuum arc (FCVA)

Unlike the deposition techniques that the atoms are the film forming precursor, FCVA is a low-temperature thin film deposition method, equipped with a high power electric arc discharged at the target material and blasted some material away into highly ionized vapor. Those ions will be guided through the chamber by magnetic coils and finally deposited onto the substrate. With a high purity (99.99%) graphite cathode, the carbon plasma is formed by explosive emission process, starting from the cathode spots, where the arc current is concentrated. The cathode spot is only 1-10 μm in size but the current density is as high as 10^6-10^8 A/cm^2 [Brown, 1998] A pulsed substrate bias voltage can be applied to accelerate the ions, bombarding the film-forming surface, and densify the film. With the optimum substrate bias at ~100 V, the hydrogen-free a-C films with a high sp^3 fraction at ~87.5% [Xu et al., 1996; Pharr et al.,1996, Anders, 2002] can be synthesized.

Figs. 2.3(a) and 2.3(b) shows the schematics of the in-house FCVA system operated in direct current mode. The plasma generated by the arcing between the cathode coil and the upstream coil is guided through the upstream, auxiliary, and downstream coils toward the substrate holder. The out of plane S-shaped electromagnetic coils are used to filter out microdroplets and macroparticles ensure that only the carbon ions arrive the substrate and contribute to the carbon growth. The chamber base pressure is kept below 5×10^{-7} Torr with the cryopump. Plasma arcing is induced at the cathode surface with a mechanical striker and stabilized by applying a cusp-configuration magnetic field to the cathode [Zhang & Komvopoulos, 2008]. The magnitude, frequency, and duty cycle of the pulsed bias is adjusted by a dc voltage source and an electrical chopper (Spark-le V, Advanced Energy Industries).

2.2.3 Plasma-enhanced chemical vapor deposition (PECVD)

RF-PECVD is another common used deposition technique if hydrogen content in the a-C films is required. A carbon containing gas is introduced into the chamber and decomposed by the rf plasma into film forming hydrocarbon free radicals that can be adsorbed onto the substrate via chemical bonding to other atoms on the surface. The glow discharge can activate almost any reaction at relatively low substrate temperature compared to the traditional thermal CVD. The

most popular precursor includes CH_4, C_2H_2, C_2H_4, etc and the carbon coatings deposited by PECVD usually contain hydrogen up to 50%. [Bhushan et al., 1992; Grill et al.,1990]

2.2.4 Other deposition techniques

Except those deposition techniques introduced earlier, *a*-C films can be deposited by other methods, including the ion beam deposition, pulsed-laser deposition, etc.

In a typical ion-beam deposition system [Aisenberg and Chabot, 1971], carbon ions are either produced by plasma sputtering of a graphite cathode in an ion source or extracted from an ionized hydrocarbon gas in a plasma. Negative bias is applied to the substrate to accelerate positive ions.

In pulsed laser deposition [Kovarik et al.,1993], A short but intense energetic laser pulses can be used to ablate the graphite target and vaporize materials as an intense plasma. The plasma then expands to the substrate and grows the film. Due to the high energy of the laser plasma and nonequilibrium process, the properties and structures of the synthesized *a*-C films are similar to those from FCVA method.

2.3 Film characterization techniques

To characterize the topography of *a*-C films, AFM is used to measure the surface roughness. The thickness of the film is confirmed by cross-sectional TEM. XPS and Raman are used to detect and compare the overall sp^3 fraction in the film; while a more detailed analysis on the nanostructure of the film is conducted by EELS.

2.3.1 Atomic force microscope (AFM)

AFM is a high-resolution type of scanning probe microscopy (SPM) firstly invented in 1986 (Binnig et al., 1986). Thereafter it has been widely used in the scientific and academic fields as a common method to examine the surface topographical properties and morphology, and even manipulate atoms.

AFM scans the surface of the sample using a compliant piezoelectric cantilever with a sharp tip at the end. When the tip is in proximity of the sample surface, the cantilever will deflect by the forces between the tip and sample, which can be measured by a laser spot reflected from the cantilever surface to an array of photodiodes. By detecting the interatomic interaction between the tip and the sample, AFM can sharply correspond to the height of the current scanning point and render the contours of the surface by scanning a specific area on the sample. The schematics of basic AFM operation are shown in Fig. 2.4.

An AFM (NanoScope II, Digital Instrument) system is used to measure the topography of *a*-C films in this dissertation. The AFM images is obtained in the tapping mode with Si tip of nominal radius of curvature < 10 nm. For statistical analysis, at least three different surface

locations on the sample are imaged and the root-mean-square (rms) surface roughness are calculated.

2.3.2 X-ray photon spectroscope (XPS)

XPS is a non-destructive surface-sensitive analytical technique to measure the elemental composition within a material based on the photoelectric effect. The spectrum is obtained by irradiating the material with X-ray beam while simultaneously measuring the kinetic energy and number of core electrons that escape from the top surface (~10 nm depth) in the material. The electrons absorb the energy of X-ray photon ($h\nu$), get out of the material surface with energy E_k, the difference will be used to predict the binding energy of the core electron, with the Ernest Rutherford (1914) relationship:

$$E_b = h\nu - E_k - \phi \tag{2.1}$$

Where E_b is the binding energy of the electron, $h\nu$ is the X-ray photon energy, E_k is the kinetic energy of photoelectron measured by the energy analyzer, ϕ is the work function, which the photoelectrons would give up as it becomes absorbed by the detector. There is a small shift (0.9 eV) of the C core level spectra between diamond and graphite due to the slightly shorter bond length of sp^2 bonds than sp^3 bonds that sp^2 sites have a slightly deeper potential than sp^3 sites. This difference is used to determine the fraction of sp^2/sp^3 sites in *a*-C films.

The PHI 5400 ESCA/XPS system (Physocal Electronics, Chanhassen, MN) is used in this dissertation. It works with a nonmonochromatic Al-Kα X-ray source of 1486.6 eV energy and work function of 5.7 eV, under a vacuum pressure of less than 5×10^{-9} Torr. It features a spatial resolution of 0.5 mm, energy resolution of 0.7 eV, and atomic percent sensitivity of ~1 at%.

The C1s core-level spectra in the range of 280-292 eV were acquired to determine the sp^3 content, using a 0.1 eV energy step and acquisition time fixed at 50 ms/step. To preserve the original surface chemical characteristics, the samples were not cleaned by Ar^+ ion bombardment before the XPS analysis. After performing background noise subtraction with the Shirley method [Shirley, 1972], the C1s core level XPS spectra of the *a*-C films were fitted with six 90% Gaussian–10% Lorentzian (GL) distributions and the sp^3 and sp^2 hybridization contents were calculated with a standard least–squares algorithm. Each GL distribution was associated with a certain chemical state of a characteristic binding energy. The C1s-1, C1s-2, and C1s-3 peaks were corresponding to sp^1, sp^2, and sp^3 C-C hybridizations, respectively, and C1s-4, C1s-5 and C1s-6 representing high-order C–O, C=O, and HO-C=O bonds, respectively. Atomic percentages of each constituent were calculated as the areas under the corresponding GL distributions.

2.3.3 Raman spectroscope

Raman spectroscope is also a popular, non-destructive tool for structural characterization of carbons by detecting the vibrational, rotational and other low-frequency modes [Smith & Dent, 2005]. It uses the inelastic scattering of the laser interacting with a sample, resulting a frequency shift of reemitted laser photons compared with the original photons that has been absorbed by the

sample. Those shift (Strokes Raman scattering for up shift and Anti-Strokes Raman scattering for down shift) can be used to characterize the structure and composition of a-C films.

A visible Raman spectroscope (WiRE, Renishaw Raman Imaging Microscope) that equipped with a 514.5-nm Ar^+ ion laser focused to a spot of <4 μm in diameter is used to examined the film structure in the dissertation. Raman spectra were recorded in the range of 850–1950 cm^{-1}, featuring a D peak at 1350 cm-1 and the G peak at 1550 cm-1 due to the A_{1g} breathing mode of sp^2 bonds in aromatic rings only and the E_{2g} in-plane bond stretching vibration mode of all sp^2 bonds existing in both aromatic rings and linear chains, respectively [J. Robertson, 2002]. The structure and disorder level can be assessed by analyzing the shape and intensity of the two peaks. For statistical analysis, Raman spectra were collected from at least three different locations on each film surface.

2.3.4 Transmission Electron Microscope (TEM)

2.3.4.1 Sample preparation

Cross-sectional HRTEM samples were prepared by mechanical grinding, dimpling, and surface finishing by ion milling. To distinguish the *a*-C film from the epoxy glue and to ensure that the EELS carbon signal was only due to the *a*-C film, a thin Au capping layer was sputtered onto the surface before sample bonding. The film samples were first cleaved into two halves and glued face-to-face with M-bond 610 epoxy. After curing at 160 ℃ for 90 min, additional Si(100) was glued to both sides of the sandwiched film samples to increase the thickness to >3 mm. Then, the samples were sectioned into ~500-mm-thick slices by a diamond blade and saw-cut to 3-mm-diameter disks. Finally, the disks were thinned down to a thickness of <20 μm at the center by double-side dimpling and ion milled from top and bottom with Ar^+ ion guns (PIPS II, Gatan) operated at 4.5 kV. An Ar^+ ion incidence angle of 5° was used to produce a through-thickness hole across the sample/epoxy/sample interface. The specimen preparation process is illustrated in Fig. 2.5.

2.3.4.2 High-resolution transmission electron microscopy (HRTEM)

HRTEM is an imaging mode of TEM that renders atomic resolution images. The HRTEM images are reconstructed from the phase contrast, which arises from the interference of electron waves of direct and diffracted beams that pass through the specimen.

The 200 kV FEI monochromated F20 UT Tecnai microscope is used to obtain HRTEM images and perform EELS studies. The spherical aberration C_s is 0.5 mm and the chromatic aberration C_c is 1.1 mm. With monochromator off, the information limit is 0.12 nm for HRTEM, spatial resolution is 0.14 nm for STEM, and energy resolution is 500 meV for EELS. The image of the Tecnai is shown in Fig. 2.6.

HRTEM images and EELS spectra were obtained with a FEI Tecnai (F20 UT) microscope operated at 200 kV, equipped with a CCD camera (2048 × 2048 pixels) positioned 42 mm

behind the Gatan imaging filter. A 9.3-mrad C2 semi-angle and a 150-μm C2 aperture were used in this study. The EELS collection semi-angle was set at 16.3 mrad. Using the full width at half maximum (FWHM) of the zero-loss peak, the energy resolution was found to be equal to 0.58 eV, which is sufficiently low for distinguishing sp^2 from sp^3 hybridization, considering the band gap difference between sp^2 and sp^3 is ~0.8–0.9 eV.

2.3.4.3 Electron energy loss spectroscope (EELS)

Electron energy loss spectroscopy is a useful tool for analyzing the nanostructure of various materials in high resolution. The incoming electrons pass through the specimen, accompanied by momentum change, energy transfer, and electron scattering due to the interaction with the specimen atoms. The interaction is categorized as elastic and inelastic scattering.

In elastic scattering event, the incident electron interacts with the atomic nucleus. The energy exchange is small and normally undetectable because the mass of electron is much smaller than the mass of nucleus. On the other hand, in the inelastic scattering event, the incoming electrons interact with the electrons in the specimen material. The energy loss in this case can range from a few to hundreds of eV because of the similar masses.

The amount and energy distribution of electrons that pass through the specimen is measured by the EELS, which shows the number of electrons as a function of the energy loss. It reflects statistical change of inelastic scattering event happening, which mostly comes from the photon excitation, plasmon excitation, and core electron excitation. Among those events that are highly related to the chemistry bonding structure of the atoms in the specimen, the inner shell ionization is usually used to detect the elemental components of a material. The Fig. 2.7 shows different C K-edge EELS spectra of carbon allotropes including graphite, diamond, *a*-C, hydrogenated *a*-C (*a*-C:H) and tetrahedral a-C (*ta*-C). The strong pre-peak at 285 eV identifies the K shell electrons transfer into the empty π^* states which is only in sp^2 graphite-like bonding, while the K edge starting from 290 eV shows the transition into σ^* states in both sp^2 hybridization graphite-like bonding and sp^3 hybridization of diamond-like bonding. Therefore, the structure of *a*-C, which contains both sp^2 and sp^3 bonding can be quantified by analyze the EELS spectra of the specimen.

2.3.5 Triboscope

The tribomechanical properties of the *a*-C films (i.e. the nanohardness, reduced elastic modulus, and coefficient of friction) can be studied with a surface force microscope equipped with a force transducer (Triboscope, Hysitron) interfaced with an AFM (NanoScope II, Digital Instruments). With the instrument, the nanoindentation test and nanoscratch tests are conducted to obtain the nanohardness and reduced elastic modulus, and coefficient of friction, respectively.

2.3.5.1 Nanoindentation and hardness

The film mechanical properties including the hardness and reduced elastic modulus can be measured with a pyramidal diamond tip with a nominal radius of curvature equal to ~40 nm. The tip shape function is obtained and calibrated by indenting a standard sample of ultra-smooth fused quartz of bulk hardness equal to 10 GPa, based on the assumption that the Young's modules is independent of indentation depth. The indentation force is applied in an incremental fashion, using an isosceles triangular loading and unloading force profile. During a nanoindentation test, the probe is driven into the sample and then withdrawn by decreasing the applied force. The applied load P and the depth of penetration h into the sample are continuously monitored. A load vs. displacement curve can be generated from the collected data. Fig. 2.8 is a typical load vs. displacement response curve, from which the hardness and reduced elastic modulus of the *a*-C films can be determined by the following equations:

$$H = \frac{P_{max}}{A} \tag{2.2}$$

$$E_r = \frac{S\sqrt{\pi}}{2\sqrt{A}} \tag{2.3}$$

where P_{max} is the load magnitude, A is the resultant projected contact area, S is the stiffness, which is derived from the slope of the unloading curve dP/dh at the maximum displacement that the load P and the depth h follows the power relation [Oliver & Pharr, 1992, 2004].

$$P = k(h - h_f)^m \tag{2.4}$$

A can be expressed as a function of contact depth h_C from the calibrated tip shape function:

$$A = C_0{h_C}^2 + C_1 h_C + C_2{h_C}^{1/2} + C_3 h^{1/4} + C_4 h^{1/8} + C_5 h^{1/16} \tag{2.5}$$

E_r is the reduced elastic modulus, containing information of both sample and indenter that:

$$\frac{1}{E_r} = \frac{1-{\upsilon_i}^2}{E_i} + \frac{1-{\upsilon_s}^2}{E_s} \tag{2.6}$$

where subscript i and s indicates properties of indenter and specimen. ν is the Poisson's ratio. For a standard diamond indenter probe, E_i is 1140 GPa and ν_i is 0.07.

At least five indentations were performed at different locations of each film surface.

2.3.5.2 Nanoscratch and coefficient of friction

Tribological tests were carried out with a conical diamond tip of nominal radius of curvature 1 or 20 μm based on the specimens. In these tests, the lateral force is detected while the normal force is applied and can be varied. The coefficient of friction is defined as the ratio of the measured friction force to the applied normal force, which was calculated as the average of 300 coefficient of friction measurements obtained along the sliding track for statistical accuracy.

2.3.6 Film stress measurement

Film residual stress usually builds when the energetic ion bombardment takes place during the deposition. Normally the higher the sp^3 fraction, the higher the residual stress. Film stress measurements are obtained with a Flexus system (KLA-Tencor FLX-2320). It uses a laser

interferometer to accurately measure the changes in the radius of curvature of the substrate caused by the deposition of a stressed thin film on the substrate. The residual stress σ in the films is obtained from Stoney's equation:

$$\sigma = \left(\frac{E}{1-\nu}\right)\frac{h^2}{6Rt} \tag{2.7}$$

where $E/(1-\nu)$ is the biaxial elastic modulus of the substrate (180.5 GPa for Si(100)), h and t are the thickness of the substrate and the film, respectively, and R is the measured radius of curvature of the coated substrate.

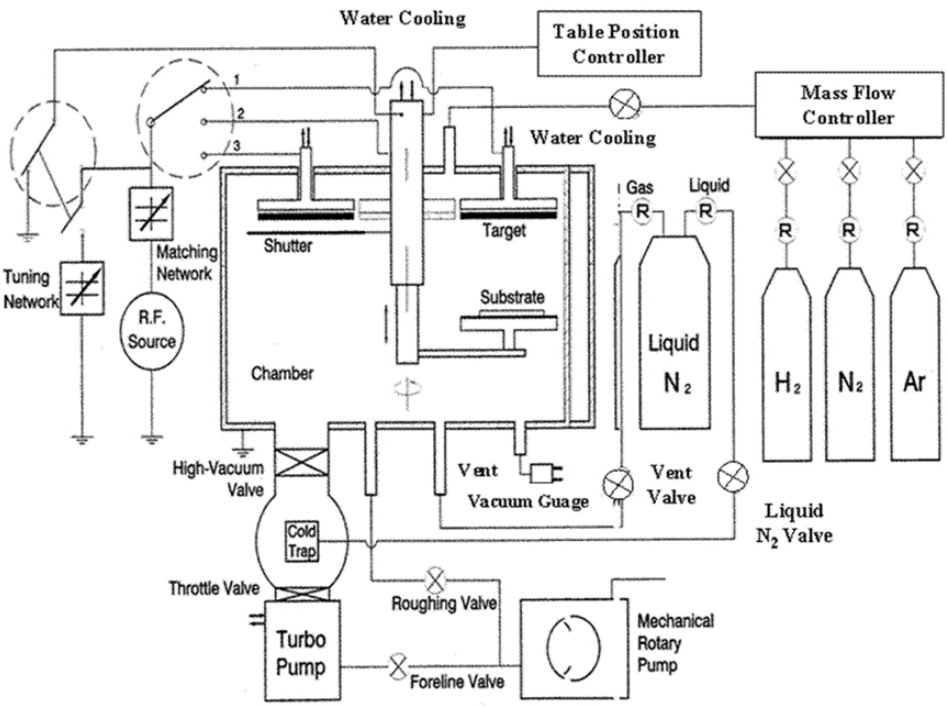

Fig. 2.1 Schematics of RF sputtering system.

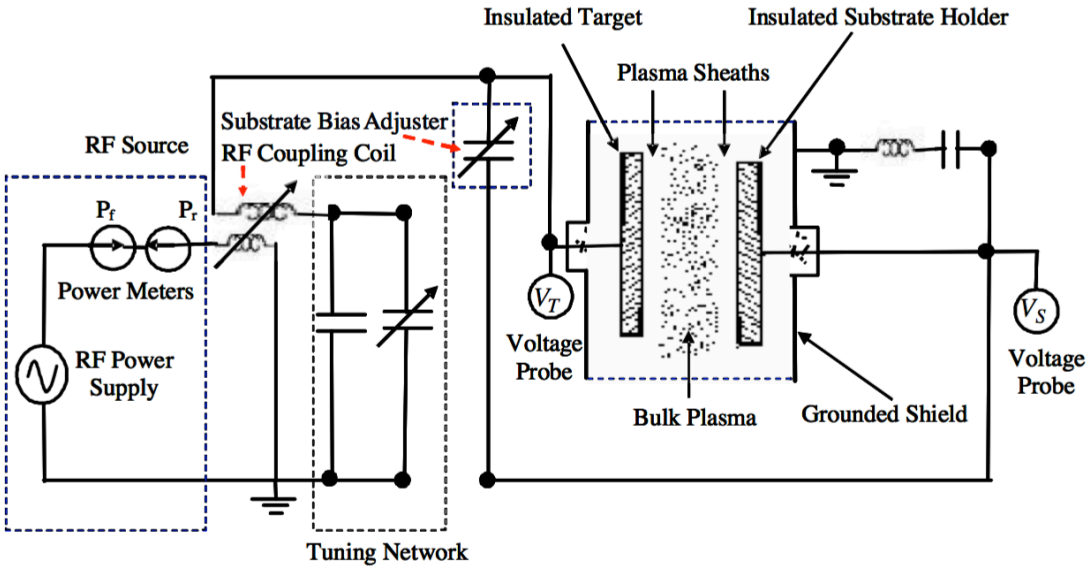

Fig. 2.2 Schematics of electrical power matching network.

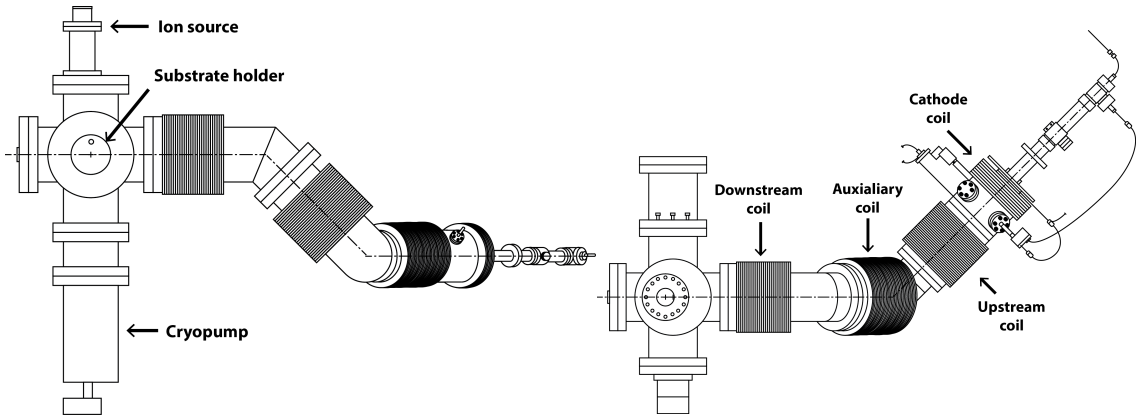

Fig. 2.3 Diagram of FCVA system front view (left), and top view (right).

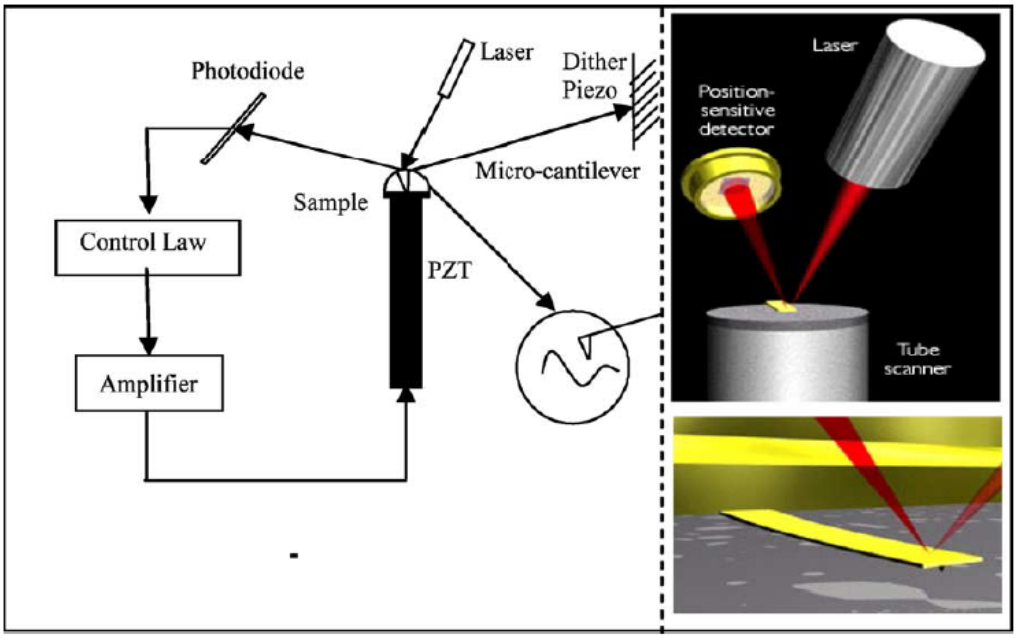

Fig. 2.4 Schematics of basic AFM operation (left), real micro-cantilever and component (right) [Jalili & Laxminarayana, 2004].

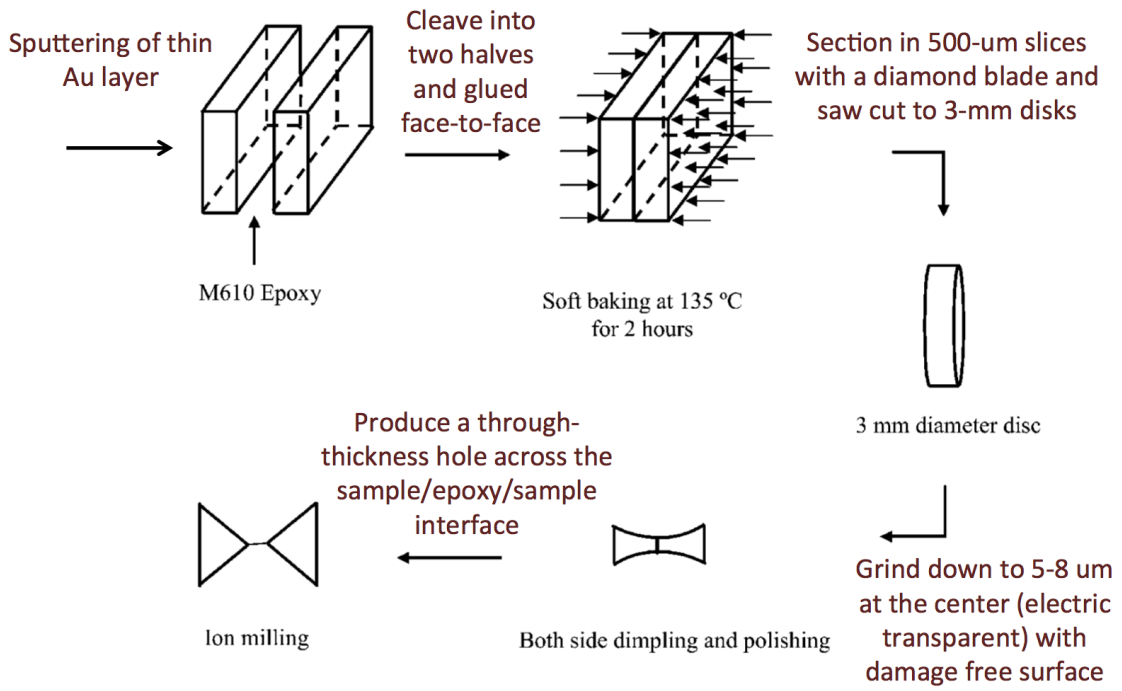

Fig. 2.5 Cross-section TEM specimen preparation procedure. [Wan & Komvopoulos, 2004]

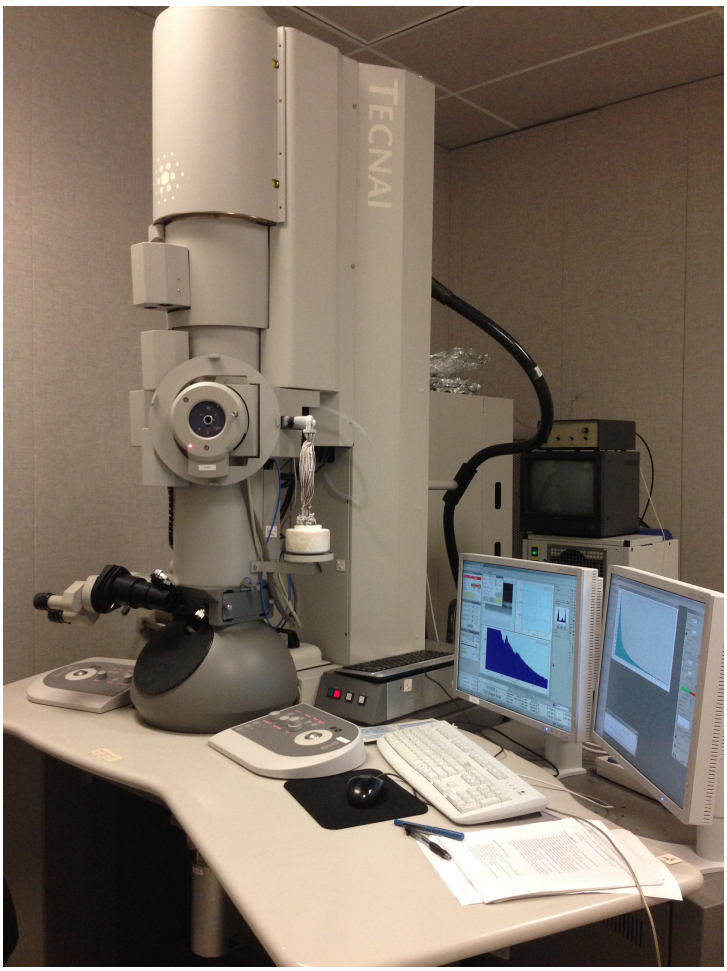

Fig. 2.6 Images of the Tecnai TEM system.

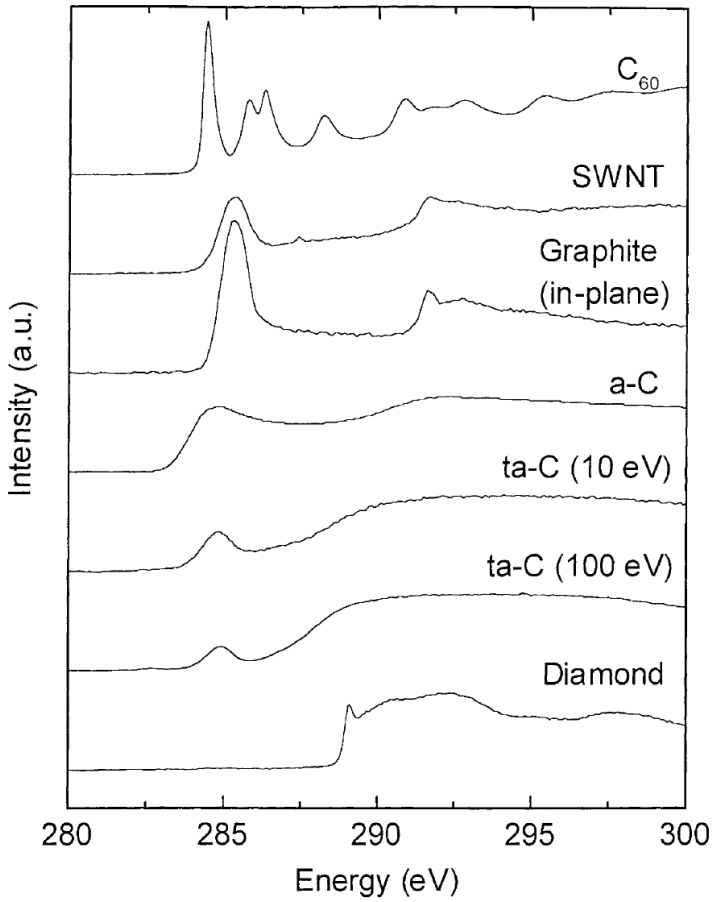

Fig. 2.7 C K-edge EELS spectra of carbon allotropes including graphite, diamond, *a*-C, hydrogenated *a*-C (*a*-C:H) and tetrahedral *a*-C (*ta*-C) [Robertson, 2002].

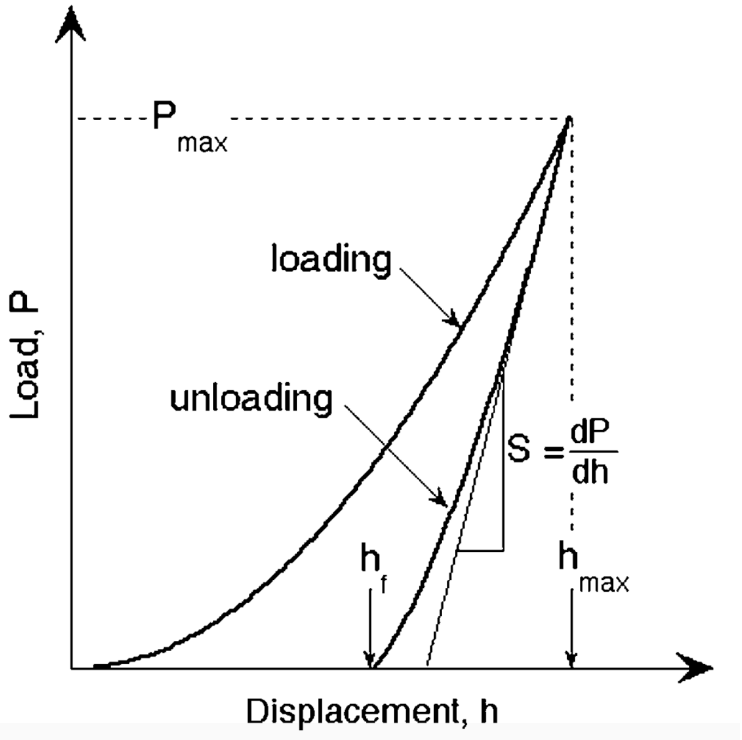

Fig. 2.8 Schematics of indentation load vs. displacement response curve [Oliver & Pharr, 2004].

Chapter 3 The effects of substrate bias voltage on the growth and properties of *a*-C films deposited by radio-frequency sputtering

3.1 Introduction

Amorphous carbon (*a*-C) films have been at the frontline of thin-film research for a long time mainly because of the excellent physical properties, chemical inertness, transparency, and potential as protective overcoats of these films in several leading technologies, such as hard-disk drives and microelectromechanical devices [Erdemir & Donnet, 2006; Chu & Li, 2006; Robertson, 2002]. Among various carbon film deposition methods [Lifshitz, 1999], mass-selected ion-beam deposition [Ishikawa, 1987], filtered cathodic vacuum arc [McKenzie et al., 1991], and laser ablation [Kovarik et al., 1993] use energetic carbon ions as film-forming precursors. Tetrahedral (sp^3) carbon atom hybridization due to energetic carbon ions leads to the formation of a three-layer film structure consisting of an interface layer, the bulk film, and a surface layer [Davis et al., 1998], which can be explained by the subplantation model [Robertson, 2002].

Conversely to deposition methods using ionized film-forming precursors, radio frequency (rf) sputtering, one of the most common film deposition techniques, uses low-energy neutral carbon atoms or clusters of atoms to form *a*-C films. Sputtering is an advantageous thin-film deposition process because of its intrinsic low levels of input energy, temperature, and vacuum compared to deposition methods using energetic ions as film-forming precursors. Inert ion bombardment of the growing film surface during sputtering enables tailoring of the film properties without altering the chemical environment of the film. By controlling the absorbed rf power, substrate bias voltage, deposition time, working pressure, and flow rate of process gas, ultrathin *a*-C films with sp^3 contents higher than 50 at% and nanohardness of ~39 GPa can be synthesized under optimum rf sputtering conditions [Lu & Komvopoulos, 1999]. The substrate bias voltage is a key deposition parameter because it directly affects the ion bombardment energy. While the hardness of *a*-C film increases with the bias voltage, above a critical substrate bias voltage (about –150 V) the film hardness decreases due to relaxation due to thermal spikes produced from intense ion bombardment [Lu & Komvopoulos, 1999]. The very low roughness of *a*-C films deposited under rf sputtering conditions of –200 V substrate bias voltage has been attributed to the enhancement of carbon atom diffusion at the film surface, whereas film roughening for substrate bias voltage above –200 V has been associated with re-sputtering and irradiation damage by the highly energetic Ar^+ ions [Wan & Komvopoulos, JAP, 2006(A)].

Although the effect of plasma discharge conditions (in particular, the substrate bias voltage) on the growth and properties of sputtered *a*-C films has been investigated in previous studies, knowledge of the hybridization mechanisms and film structure-property interdependencies is sparse. Although insight into sp^3 hybridization under different substrate bias conditions has been provided by a previous probabilistic analysis of carbon atom hybridization in rf sputtered *a*-C films [Wan & Komvopoulos, 2006(B)], the effects of irradiation damage and thermal spikes

were not considered and the substrate bias voltage was not varied above –200 V. Therefore, an in-depth study of the underlying hybridization mechanisms in the presence of thermal spikes on the structure of sputtered *a*-C films is timely and of high importance not only to the properties but also the stability of such ultrathin films.

The objective of this study is to elucidate the effects of plasma discharge conditions generated under different substrate bias voltages on the surface roughness, structure, and tribomechanical properties of ultrathin *a*-C films deposited by rf sputtering. The interdependence of surface topography (roughness), structure (hybridization), hardness, reduced elastic modulus, and coefficient of friction of sputtered *a*-C films on plasma discharge conditions is discussed in the light of atomic force microscope (AFM), surface force microscope (SFM), and X-ray photoelectron spectroscopy (XPS) measurements and results derived from particle collision analysis.

3.2 Experimental procedure

3.2.1 Film deposition

Ultrathin *a*-C films were deposited on Si(100) substrates by sputtering a pure (~99.99%) graphite target with Ar^+ ions in a low-pressure sputtering system (Perkin-Elmer, Randex-2400 model). The vacuum chamber was first pumped down to a low base pressure (~2×10^{-6} Torr) to remove any residual gases adsorbed onto the chamber walls. The graphite target was then sputtered for 5–20 min, depending on the time of its exposure to the atmosphere, whereas the Si(100) substrate was sputtered for 3 min to remove an ~45-nm-thick surface layer, under conditions of working pressure p = 3 mTorr, forward rf power P_f = 250 W, and Ar gas flow rate f = 20 sccm. Film deposition was subsequently performed under plasma discharge conditions of adsorbed rf power P_a = 745–750 W, substrate bias voltage V_s between 0 and –300 V, and all other process parameters fixed, i.e., p = 3 mTorr, f = 20 sccm, and deposition time t = 0.4 min. *a*-C films deposited under these plasma discharge conditions have been found to demonstrate optimum properties [Lu & Komvopoulos, 1999; Lu & Komvopoulos, 2001].

3.2.2 Atomic force microscopy

The film surface roughness was measured from 2 × 2 μm^2 images acquired with an AFM (NanoScope II, Digital Instruments), which was operated in tapping mode. All AFM images were obtained with silicon tips of nominal radius of curvature equal to ~10 nm. The root-mean-square (rms) surface roughness of the *a*-C films was calculated as the mean value of at least four measurements obtained from different AFM images of each film surface.

3.2.3 Tribomechanical testing

The tribomechanical properties of the *a*-C films (i.e., nanohardness, reduced elastic modulus, and coefficient of friction) were studied with an SFM consisting of a special force transducer

(Triboscope, Hysitron) interfaced with an AFM (NanoScope II, Digital Instruments). The film mechanical properties were measured with a pyramidal diamond tip with a nominal radius of curvature equal to ~40 nm and tip shape function obtained by indenting a standard sample of ultra-smooth fused quartz of bulk hardness equal to 10 GPa. The indentation force was applied in an incremental fashion, using an isosceles triangular force profile of 20 μN peak force and loading/unloading times fixed at 6 s. The hardness and reduced elastic modulus of the *a*-C films were determined from the indentation force versus depth response, as detailed elsewhere [Lu & Komvopoulos, 1999; 2001; Wan & Komvopoulos, 2006(A); Wan & Komvopoulos, 2006(B)]. At least five indentations were performed at different locations of each film surface.

Tribological tests were carried out with a conical diamond tip of nominal radius of curvature equal to 1 μm. In these tests, the normal force was varied in the range of 40–160 μN, whereas the sliding speed and the lateral displacement were fixed at 0.4 $\mu m \cdot s^{-1}$ and 4 μm, respectively. The coefficient of friction (defined as the ratio of the measured friction force to the applied normal force) was calculated as the average of 300 coefficient of friction measurements obtained along the sliding track.

3.2.4 X-ray photoelectron spectroscopy

XPS spectra were acquired with a PHI model 5400 ESCA/XPS system. All of the XPS studies were performed under a vacuum pressure of $<5 \times 10^{-9}$ Torr using an Al-Kα anode X-ray source of 1486.6 eV energy, 0.1 eV energy step, and 0.025 eV analyzer energy resolution. After performing background noise subtraction with the Shirley method [Shirley, 1972], the C1s core level XPS spectra of the *a*-C films were fitted with 90% Gaussian–10% Lorentzian (GL) distributions and the sp^3 and sp^2 hybridization contents were calculated with a standard least–squares algorithm. Each GL distribution was associated with a certain chemical state of a characteristic binding energy. Atomic percentages of each constituent were calculated as the areas under corresponding GL distributions. To preserve the original surface chemical characteristics, the samples were not cleaned by Ar^+ ion bombardment prior to the XPS analysis. The very low intensity of the C peak in the XPS spectrum of the uncoated Si substrate confirmed that airborne carbonaceous substances (e.g., adventitious carbon) were effectively desorbed from the film surfaces under the low working pressure of XPS.

3.3 Results and discussion

It has been previously shown [Wan & Komvopoulos, 2006(A)] that the film thickness h mainly depends on the sputtering rate β of the target material (which is equal to the sputtering yield γ multiplied by the Ar^+ ion flux J_{Ar^+}) and the deposition time, i.e., $h \propto \beta t$. As shown below, the sputtering rate can be fixed by controlling the rf power and substrate bias voltage. In this case, the film thickness is almost linearly proportional to the deposition time, and the thickness of ultrathin films can be determined by a linear extrapolation of the thickness data corresponding to thicker films (i.e., $t > 3$ min with all other plasma discharge conditions fixed). Using this approach, the thickness of the *a*-C films deposited under plasma discharge conditions of P_a= 745–750 W, V_s = –200 V, and t = 0.4 min was found to be equal to 4.64 nm.

Fig. 3.1(a) shows the film roughness as a function of substrate bias voltage. The decrease in film roughness with the variation of the substrate bias voltage between 0 and –200 V is attributed to the intensification of Ar^+ ion bombardment onto the growing film surface. The smoothest film corresponds to plasma discharge conditions of V_s = –200 V. The increase in film roughness due to the change in V_s beyond –200 V is a result of excessive sputtering and irradiation damage. The film nanohardness and reduced elastic modulus were obtained from indentation force versus displacement responses for indentation depth fixed at ~2.8 nm. Figs. 3.1(b) and 3.1(c) show that the highest hardness and reduced elastic modulus correspond to V_s = –200 V, suggesting that *a*-C films deposited under these plasma discharge conditions exhibit the highest sp^3 content. The enhancement of the film nanomechanical properties with the variation of V_s from 0 to –200 V can be related to the beneficial effect of Ar^+ ion bombardment, whereas degradation of the film properties with the variation of V_s beyond –200 V is due to the excessive irradiation damage caused by the highly energetic Ar^+ ions.

The indirect effect of substrate bias voltage on the mechanical properties of *a*-C films may be explained by considering the dependence of mechanical properties on the carbon-carbon bond strength of different hybridizations. The outermost s and p orbitals of carbon atoms form π and σ bonds in sp^2 hybridizations, but only σ bonds in sp^3 hybridizations. The stronger σ bonds in sp^3 hybridizations control the mechanical properties, whereas the weaker π bonds are mainly responsible for the electrical and optical properties [Robertson, 2002]. The elastic modulus E of the *a*-C films can be related to the mean coordination <*r*> of carbon-carbon bonds by $E = E_0(\langle r\rangle - 2.4)^{3/2}$, where E_0 is the elastic modulus of diamond, $\langle r\rangle = (2n_2 + 3n_3 + 4n_4)/(n_2 + n_3 + n_4)$, and n_i is the number of atoms with i bonds [He & Thorpe, 1985; Robertson, 1994(A)]. For *a*-C films, n_2, n_3, and n_4 represent the number of carbon atoms in sp^1, sp^2, and sp^3 bonding configurations, respectively. Moreover, the film hardness H can be approximately related to the elastic modulus by $H \approx E/10$ [Robertson, 1992]. The former elastic modulus and hardness relations indicate an increase in film stiffness and plastic flow resistance with increasing coordination, implying an improvement of the film mechanical properties with increasing sp^3 fraction.

Fig. 3.2 shows the variation of the coefficient of friction of *a*-C films with substrate bias voltage and normal force. The decrease of the coefficient of friction with increasing normal force for fixed V_s suggests predominantly elastic film deformation under the present test conditions. This is because the coefficient of friction of elastically deformed surfaces is inversely proportional to the cubic root of the normal force and the friction force is mainly due to the effects of adhesion and surface roughness [Lu & Komvopoulos, 2001]. The lowest coefficient of friction corresponding to V_s = –100 V, regardless of applied normal force, is attributed to film shear resistance and surface roughness effects on the friction characteristics. Considering that the main friction mechanisms in smooth-surface sliding are adhesion and plowing, which depend on the shear resistance and hardness of the interacting surfaces, respectively (the *a*-C film in the present tests since the diamond tip is relatively rigid), the lowest coefficient of friction corresponding to V_s = –100 V represents a compromise in sp^3 hybridization in favor of sp^2 hybridization, yielding a moderate decrease in film plastic shear resistance and hardness, which reduces the contributions of adhesion and plowing to the coefficient of friction.

Ion bombardment not only improves the mechanical and tribological properties of the *a*-C films, but also increases film adhesion to the substrate through the formation of an intermixing layer by the knock-on effect of bombarding Ar^+ ions. Transmission electron microscopy and electron energy loss spectroscopy studies of *a*-C films deposited on Si(100) have shown the existence of a thin (~3.5 nm) interfacial layer consisting of C, Si, and, possibly SiC [Wan & Komvopoulos, 2004]. This intermixing layer, which is intrinsic of film deposition under substrate bias conditions, is conducive to the enhancement of film adhesion.

Fig. 3.3 shows the effect of substrate bias voltage on the C1s core level XPS spectrum of *a*-C films. The six GL peaks fitted to the spectra represent different types of carbon-carbon and carbon-oxygen bonding. GL distributions 1–3 correspond to sp^1-, sp^2-, and sp^3-coordinated carbon bonding (peaks at 282.5, 283.8, and 285.1 eV, respectively), whereas GL distributions 4–6 correspond to different binding states of carbon atoms with oxygen atoms, chemisorbed onto the film surface upon exposure to the ambient, i.e., C–O and/or C–OH (286 eV), C=O (287 eV), and HO–C=O (288.5 eV), respectively. The full width at half magnitude of GL distributions 1–3 and 4–6 is in the range of 1.4–1.6 eV and 2.85–2.95, respectively. The spectra demonstrate significant intensification of GL distribution 3 for V_s = –200 V, suggesting an increase in sp^3 fraction due to energetic Ar^+ ion bombardment. Because the tribomechanical properties of carbon are controlled by the strong σ bonds existing only in sp^3 carbon configurations [Tsai & Bogy, 1987; Robertson, 1992; Robertson, 2002; Lu & Komvopoulos, 1999], it may be inferred that energetic ion bombardment enhanced sp^3 carbon hybridization and, in turn, the film mechanical and tribological properties.

Fig. 3.4 shows the effect of substrate bias voltage (energetic Ar^+ ion bombardment) on sp^2 and sp^3 hybridization. The statistical data included in this figure were calculated from XPS spectra obtained from three different surface locations of each film. The sp^3 fraction increases whereas the sp^2 fraction decreases with the variation of V_s from 0 to –200 V; however, an opposite trend is observed with V_s varied between –200 and –300 V.

Table 3.1 gives statistical results of the rms roughness R_q, hardness H, reduced elastic modulus $E^* = E/(1-\nu^2)$, coefficient of friction μ, and sp^3 and sp^2 hybridization contents of *a*-C films for V_s between 0 and –300 V. The lowest roughness (R_q = 0.1 nm) and best mechanical properties, i.e., highest hardness (H = 34.2 GPa), reduced elastic modulus (E^*= 190.5 GPa), and sp^3 content (~50 at%), correspond to V_s = –200 V (film C), whereas the lowest coefficient of friction ($\mu \approx 0.15$) corresponds to V_s = –100 V (film B). The smoothness and better mechanical properties of film C correlate with the high sp^3 content, attributed to the bombardment of energetic Ar^+ ions, whereas the low coefficient of friction of film B correlates with the increase of the sp^2 content.

The results shown in Figs. 3.3 and 3.4 and Table 3.1 can be explained in the context of thermodynamic principles governing carbon atom hybridization in *a*-C films synthesized by low-pressure plasma discharges and the significant effect of the Ar^+ ion bombardment intensity, which strongly depends on the potential difference between the substrate and bulk plasma [Wan & Komvopoulos, 2007]. Under film deposition conditions of relatively intense Ar^+ ion bombardment, the relatively weaker sp^2 configurations are preferentially removed from the three-dimensional *a*-C network, increasing the percentage of stronger sp^3 configurations.

However, above a critical ion kinetic energy, excessive irradiation damage (thermal spikes) induced by the highly energetic Ar^+ ions degrades the film quality. Thus, for the plasma discharge conditions of this study (P_a = 745–750 W, $p \approx 0.4$ Pa, f = 20 sccm, and t = 0.4 min), optimum film deposition conditions occurred for V_s = –200 V, leading to the formation of high-quality *a*-C films.

Thin-film deposition by sputtering comprises three main stages: (a) sputter-off of film-forming atoms from a high-purity target material by impinging energetic Ar^+ ions, (b) transport of sputtered off atoms or clusters of atoms through the plasma space, and (c) atom diffusion on the growing film surface, resulting in chemical bonding with existing surface atoms. Therefore, to interpret the dependence of the structure and tribomechanical properties of *a*-C films on plasma discharge conditions, it is instructive to consider the characteristics of low-pressure rf plasma discharges, particularly the significance of power, working pressure, substrate bias voltage, and substrate surface temperature in each of the aforementioned stages of film synthesis.

The carbon atom flux onto the growing film surface depends on the flux of incident Ar^+ ions J_{Ar^+} onto the target surface and sputtering yield γ of target carbon atoms (defined as the number of carbon atoms ejected from the bombarded target surface per incident Ar^+ ion). For parallel-plate, capacitive, electropositive low-pressure Ar discharges, such as those of the present study, J_{Ar^+} is given by [Wan & Komvopoulos, 2006(A)]

$$J_{Ar^+} = \frac{P_a}{eA[2V_p - (V_t + V_s)]} \tag{3.1}$$

where e is the electron charge, A is the electrode area (= 324 cm^2 for both the target and the substrate of the present system), and V_p, V_t, and V_s are the time-average voltage of the bulk plasma, target, and substrate, respectively. For fixed working pressure, $V_p \approx 10$ eV and $V_t + V_s$ is almost constant (Table 3.2); hence Eq. (3.1) yields that $J_{Ar^+} \propto P_a$.

It is known that the sputtering yield depends on the energy of impinging Ar^+ ions [Ohring, 1992]. Based on the sputtering theory introduced by Sigmund [Sigmund, 1969], Matsunami et al. [Matsunami et al., 1984] estimated the sputtering yield for various ion-target combinations and derived an empirical formula of ion-induced sputtering yield Y given by

$$Y = 0.42 \frac{\alpha^* Q K s_n(\varepsilon)}{U_s[1 + 0.35 U_s s_e(\varepsilon)]} \left[1 - \left(\frac{E_{th}}{E_i}\right)^{1/2}\right]^{2.8} \tag{3.2}$$

where α^* and Q are empirical parameters, K is a conversion factor, s_n and s_e are the reduced nuclear and electronic stopping cross sections, respectively, ε is the reduced ion energy, U_s is the sublimation energy of the target material, E_{th} is the threshold energy for sputtering, and E_i is the kinetic energy of the incident Ar^+ ions (expressed in eV). For graphite, Q = 3.1 ± 0.9 and U_s = 7.37 eV [Matsunami et al., 1984; Yamamura et al. 1983]. For dominant nuclear stopping, α^* and E_{th} are given by [Matsunami et al., 1984]

$$\alpha^* = 0.08 + 0.164 \left(\frac{M_2}{M_1}\right)^{0.4} + 0.0145 \left(\frac{M_2}{M_1}\right)^{1.29} \tag{3.3a}$$

$$\frac{E_{th}}{U_s} = 1.9 + 3.8 \left(\frac{M_2}{M_1}\right)^{-1} + 0.134 \left(\frac{M_2}{M_1}\right)^{1.24} \tag{3.3b}$$

whereas s_n, s_e, ε, and K are given by [Lindhard et al., 1963(A), 1963(B), 1968]

$$s_n = \frac{3.44\varepsilon^{1/2} \ln(\varepsilon + 2.718)}{1 + 6.355\varepsilon^{1/2} + \varepsilon(-1.708 + 6.882\varepsilon^{1/2})} \tag{3.3c}$$

$$s_e = 0.079\left[\frac{(M_1+M_2)^{3/2}}{M_1^{3/2}M_2^{1/2}}\right]\left[\frac{Z_1^{2/3}Z_2^{1/2}}{\left(Z_1^{2/3}+Z_2^{2/3}\right)^{3/4}}\right]\varepsilon^{1/2} \tag{3.3d}$$

$$\varepsilon = \left[\frac{0.03255}{Z_1Z_2\left(Z_1^{2/3}+Z_2^{2/3}\right)^{1/2}}\right]\left[\frac{M_2}{M_1+M_2}\right]E_i \tag{3.3e}$$

$$K = 8.478\left[\frac{Z_1Z_2}{\left(Z_1^{2/3}+Z_2^{2/3}\right)^{1/2}}\right]\left[\frac{M_1}{M_1+M_2}\right] \tag{3.3f}$$

where M_1, Z_1 and M_2, Z_2 are the mass and atomic number of incident energetic Ar^+ ions and carbon atoms, respectively.

Equations (3.1)–(3.3) were used to calculate J_{Ar^+} and γ under the present plasma discharge conditions. Table 3.2 shows the effect of process parameters (i.e., P_a, V_t, and V_s) on J_{Ar^+} and γ. Although J_{Ar^+} is essentially insensitive to variations in V_t and V_s, γ decreases as V_t and V_s change from –1750 to –1400 V and from 0 to –300 V, respectively.

The atom flux on the growing film surface depends on the sputtering rate of target atoms $\beta = \gamma J_{Ar^+}$ and scattering intensity of film-forming atoms travelling through the plasma space, which is inversely proportional to λ/L, where L is the target-substrate distance and λ is the mean free path of travelling atoms, given by [Ohring, 1992]

$$\lambda = \frac{k_BT}{\sqrt{2}\pi d^2p} \tag{3.4}$$

where k_B is the Boltzmann constant, T is the bulk plasma temperature (much higher than room temperature) [Lieberman & Lichtenberg, 1994], and d is the atom diameter (<3 Å for carbon). For a target-substrate distance L = 7 cm (fixed in this study) and p = 0.4 Pa, Eq. (3.4) yields $\lambda >$ 10 cm. Thus, carbon atom scattering in the Ar plasma was not an important factor during film deposition under the present plasma discharge conditions because $\lambda/L > 1$.

The kinetic energy E_C transferred to carbon atoms on the growing film surface by elastic collisions with impinging Ar^+ ions is given by [Lieberman & Lichtenberg, 1994]

$$E_C = \frac{4M_1M_2}{(M_1+M_2)^2}E_i\sin^2\left(\frac{\theta}{2}\right) \tag{3.5}$$

where θ is the ion incidence angle. Thus, the average kinetic energy of surface carbon atoms $\bar{E}_C$, obtained by substituting M_1 = 39.9 and M_2 = 12 in Eq. (3.5) and integrating, is given by

$$\bar{E}_C = 0.355\bar{E}_i \tag{3.6}$$

where $\bar{E}_i$ is the average kinetic energy of bombarding Ar^+ ions.

Excited carbon atoms may collide with other carbon atoms on the film surface. The probability of this event is proportional to the nuclear stopping cross section S_n given by [Winterbon et al., 1970]

$$S_n = \frac{C_m\bar{E}_C^{(1-2m)}}{1-m}\left[\frac{4M_1M_2}{(M_1+M_2)^2}\right]^{(1-m)} \tag{3.7}$$

where C_m is a constant depending on m, which can be obtained from the Thomas-Fermi screen function for different ranges of reduced ion energy ε [Winterbon et al., 1970]. At the surface of a sputtered a-C film, $\varepsilon < 0.2$ and m =1/3 [Wan & Komvopoulos, 2006(B)]; hence, $S_n = \xi\bar{E}_C^{1/3}$, where $\xi = 6.05 \times 10^{-19}$ m^2.

The energy of surface carbon atoms excited by impinging Ar^+ ions may be dissipated by collisions with other surface carbon atoms, resulting in the removal of weakly bonded carbon atoms and, consequently, the formation of *a*-C films with high sp^3 content. The number of collisions of an excited carbon atom with other surface carbon atoms is given by $N = J_C/J_{Ar^+} = \gamma J_{Ar^+}/J_{Ar^+} = \gamma$, where J_C is the carbon atom flux. The energy of excited carbon atoms may also be dissipated in the form of thermal spikes, a process resulting in thermal relaxation that is conducive to sp^2 hybridization. The number of surface carbon atoms migrating from high- to low-density domains per incident carbon atom is approximately given by $\eta \approx 0.016(\bar{E}_C/3.1)^{5/3}$ [Robertson, 1993]. A carbon atom arriving at the growing film surface may bounce of the surface, sputter N weakly bonded surface carbon atoms, or generate thermal spikes causing the migration of η surface carbon atoms. The removal of weakly bonded carbon atoms increases the sp^3 fraction, whereas thermal spikes increase the sp^2 fraction. For equal probabilities of these two phenomena, $sp^3/(sp^2 + sp^3) \propto N/(N + \eta)$. Thus, considering that sp^3 hybridization also depends on J_{Ar^+} and S_n, which control the total number of collisions between incident Ar^+ ions and surface carbon atoms and the probability of such a collision event, respectively, the sp^3 fraction can be expressed as

$$\frac{sp^3}{sp^2+sp^3} \propto J_{Ar^+} S_n \frac{N}{N+\eta} \tag{3.8}$$

For low-pressure rf sputtering without magnetron, J_{Ar^+} depends on P_a; thus, the Ar^+ ion flux on the growing film surface is almost the same with that on the target surface [Eq. (3.1)]. Substitution of $S_n = \xi \bar{E}_C^{1/3}$, $N = \gamma$, and $\eta \approx 0.016(\bar{E}_C/3.1)^{5/3}$ into Eq. (3.8) gives

$$\frac{sp^3}{sp^2+sp^3} \propto \xi J_{Ar^+} \bar{E}_C^{1/3} \frac{\gamma}{\gamma+0.016(\frac{\bar{E}_C}{3.1})^{5/3}} \tag{3.9}$$

The validity of Eq. (3.9) can be assessed by comparing the measured sp^3 content of *a*-C films deposited under plasma discharge conditions of different substrate bias voltage with analytical results obtained from Eq. (3.9). As shown in Fig. 3.5, the experimental and analytical predictions of the sp^3 fraction follow a similar trend. (Eq. (3.9) gives results in units of eV/s because J_{Ar^+} and S_n are expressed in units of atoms/m^2·s and eV·m^2, respectively.) For $V_s = 0$ (insignificant Ar^+ ion bombardment), the removal of weakly bonded carbon atoms on the growing film surface is negligible and Eq. (3.9) yields $sp^3/(sp^2 + sp^3) \propto \bar{E}_C^{1/3}$, implying low sp^3 content for low $\bar{E}_C$. Optimum plasma discharge conditions occur for $V_s = -200$ V, because weakly bonded carbon atoms are effectively sputtered off by bombarding Ar^+ ions without causing any damage to the film structure. The present analysis predicts a maximum sp^3 fraction for substrate bias voltage of –183 V, which is close to the experimental value (–200 V) of optimum bias voltage.

3.4 Conclusion

The effect of substrate bias voltage on the tribomechanical properties and hybridization of ultrathin *a*-C films synthesized by low-pressure plasma discharges was examined in this study. For discharge conditions of substrate bias voltage equal to –200 V, *a*-C films demonstrate minimum surface roughness and maximum reduced elastic modulus, hardness, and sp^3 fraction,

whereas films deposited under discharge conditions of –100 V substrate bias voltage exhibit minimum coefficient of friction. These results reveal a strong substrate bias (energetic Ar^+ ion bombardment) effect on carbon atom hybridization. A particle collision analysis was used to explain the effect of ion bombardment on the sp^3 content of the deposited *a*-C films. The analysis yields a proportionality relation of the sp^3 fraction with the average kinetic energy of surface carbon atoms, Ar^+ ion flux, and sputtering yield, which shows a similar trend with the variation of experimentally measured sp^3 fraction with substrate bias voltage and yields an optimum substrate bias voltage, which is in good agreement with the experimental result. The findings of this study confirm the dependence of the tribomechanical properties of *a*-C films on sp^3 content and provide insight into competing effects, such as re-sputtering, irradiation damage, and thermal spikes caused by impinging energetic Ar^+ ions, on the structural integrity of *a*-C films deposited under low-pressure plasma discharge conditions.

Table 3.1 Surface roughness, mechanical properties, coefficient of friction, and carbon atom hybridization of *a*-C films versus substrate bias voltage in RF sputtering.

Film	V_s (V)	R_q (nm)	H (GPa)	E^* (GPa)	μ	sp^3 (at%)	sp^2 (at%)
A	0	0.160 ± 0.023	22.96 ± 4.70	163.38 ± 19.24	0.185 ± 0.010	9.2 ± 1.0	63.2 ± 1.9
B	–100	0.132 ± 0.012	25.45 ± 6.12	174.75 ± 32.86	0.153 ± 0.015	36.6 ± 4.6	38.4 ± 4.0
C	–200	0.100 ± 0.007	34.20 ± 9.17	190.50 ± 25.35	0.173 ± 0.021	49.9 ± 0.2	30.3 ± 2.3
D	–300	0.114 ± 0.002	19.78 ± 5.82	143.28 ± 17.62	0.182 ± 0.008	26.8 ± 6.5	49.0 ± 5.4

Table 3.2 Effect of plasma discharge conditions on Ar^+ ion flux and sputtering yield in RF sputtering.

Film	P_a (W)	V_t (V)	V_s (V)	J_{Ar+} ($\times 10^{15}$ ions/cm^2 ·s)	γ
A	748	–1750	0	8.15	0.95
B	745	–1500	–100	8.87	0.90
C	750	–1450	–200	8.66	0.88
D	748	–1400	–300	8.39	0.80

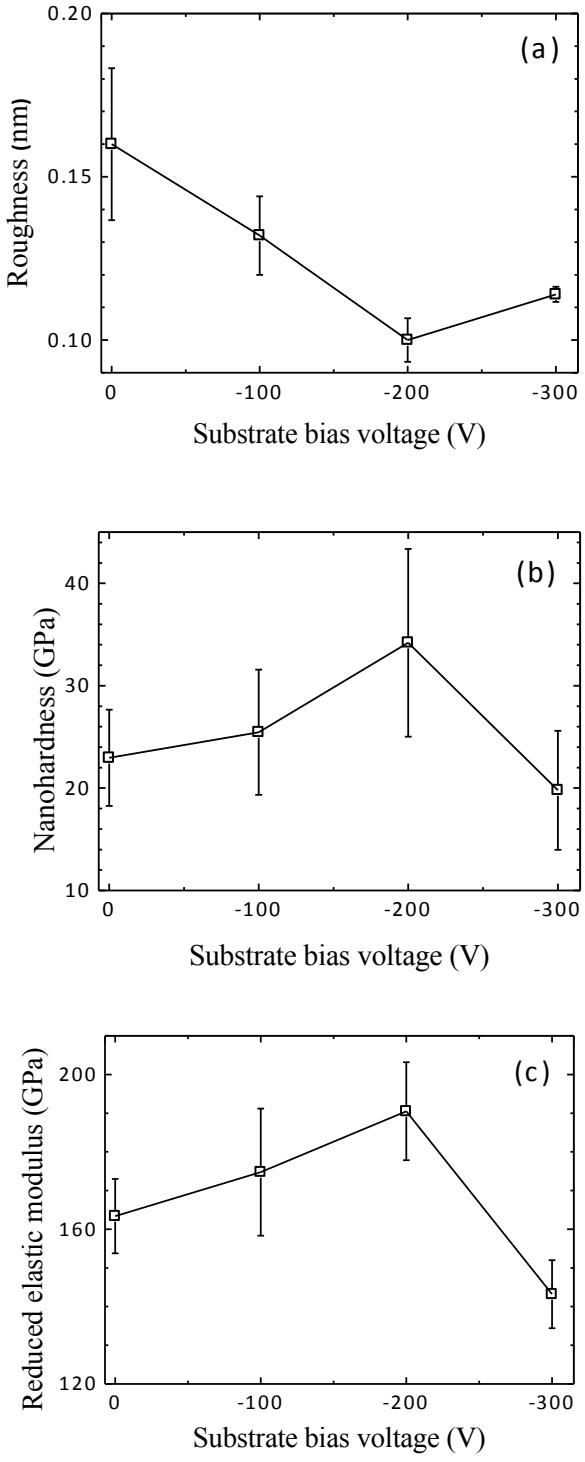

Fig. 3.1 Effect of substrate bias voltage on (a) (rms) surface roughness, (b) nanohardness, and (c) reduced elastic modulus of *a*-C films deposited under plasma discharge conditions of P_f = 750 W, p = 3 mTorr, f = 20 sccm, and t = 0.4 min.

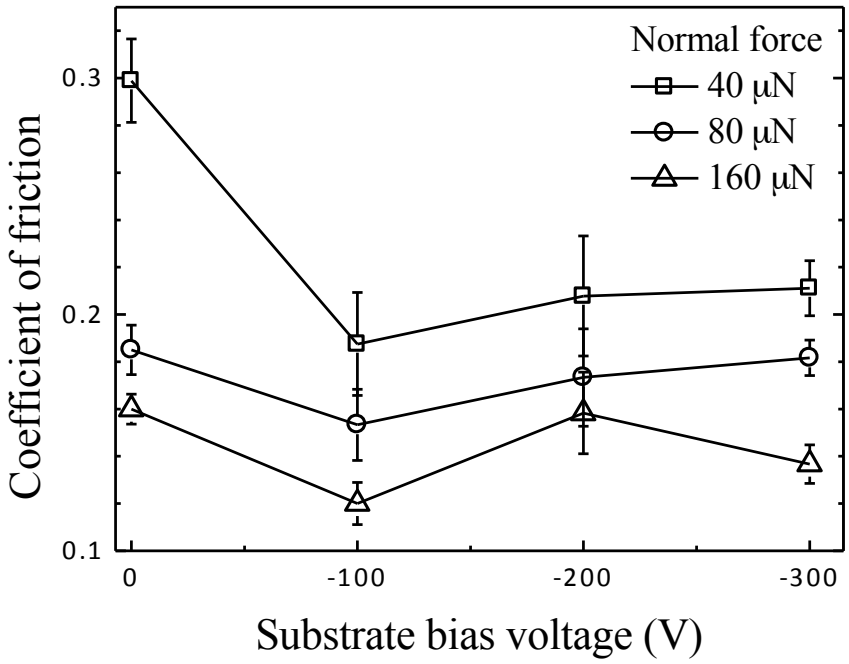

Fig. 3.2 Effect of substrate bias voltage on coefficient of friction of *a*-C films deposited under plasma discharge conditions of P_f = 750 W, p = 3 mTorr, f = 20 sccm, and t = 0.4 min for normal force equal to 40, 80, and 160 μN.

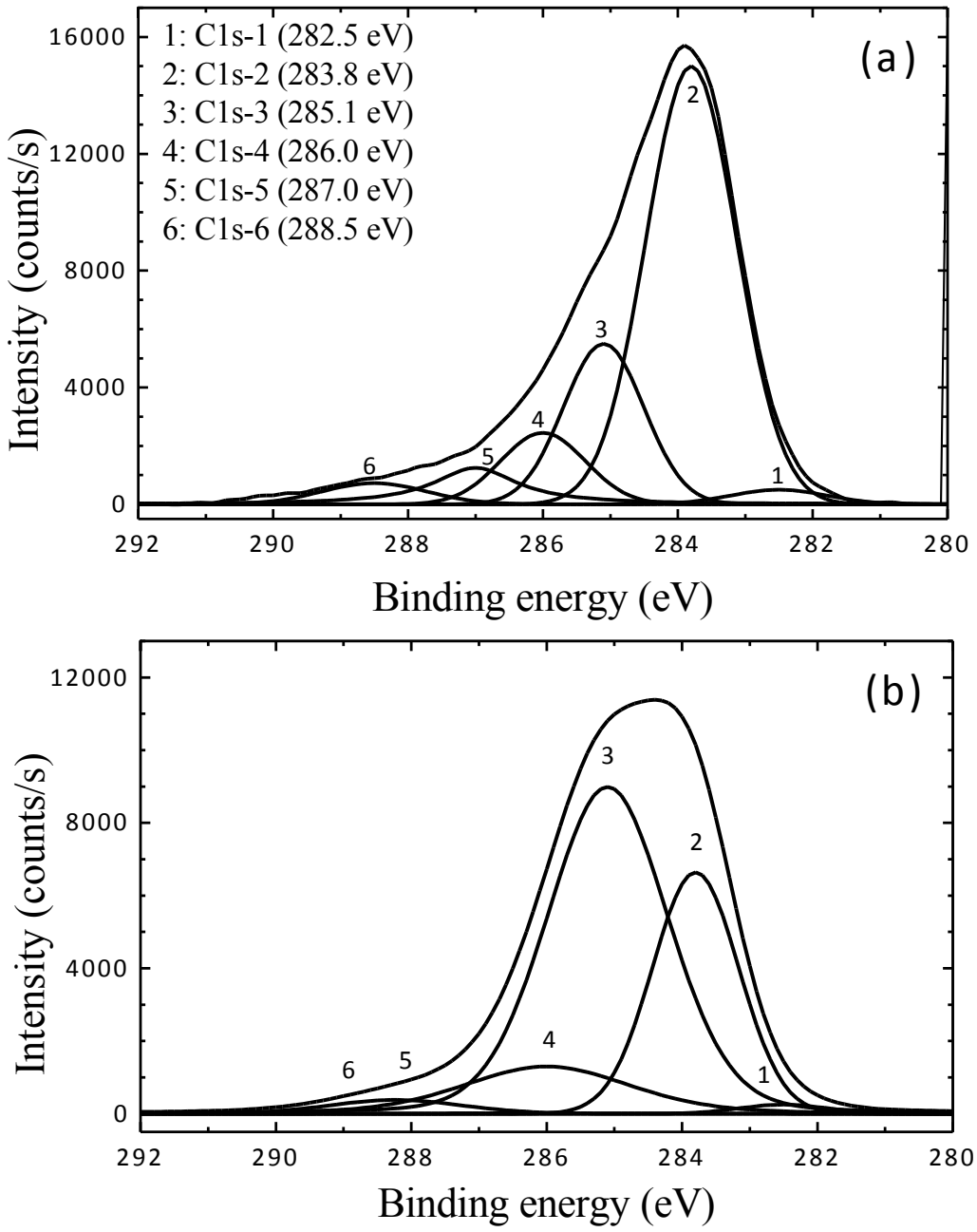

Fig. 3.3 C1s core level XPS spectra of *a*-C films deposited under plasma discharge conditions of (a) V_s = 0 and (b) V_s = –200 V and all other deposition parameters fixed (P_f = 750 W, p = 3 mTorr, f = 20 sccm, and t = 0.4 min). Each spectrum is fitted with six GL distributions corresponding to different types of carbon bonding.

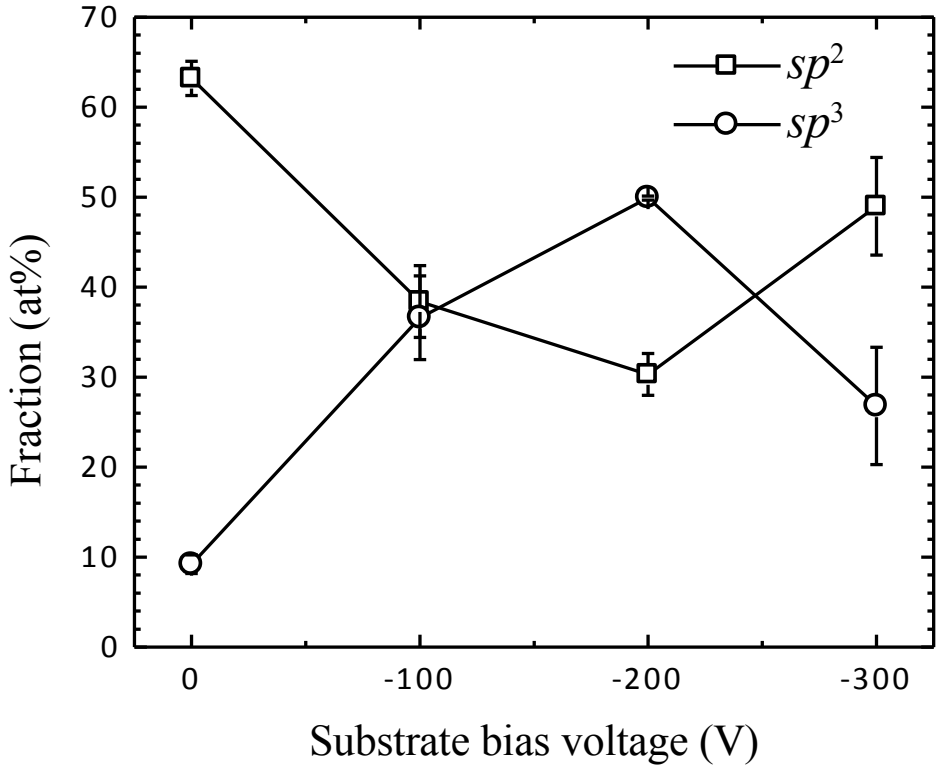

Fig. 3.4 Effect of substrate bias voltage on sp^3 fraction of *a*-C films deposited under plasma discharge conditions of P_f = 750 W, p = 3 mTorr, f = 20 sccm, and t = 0.4 min.

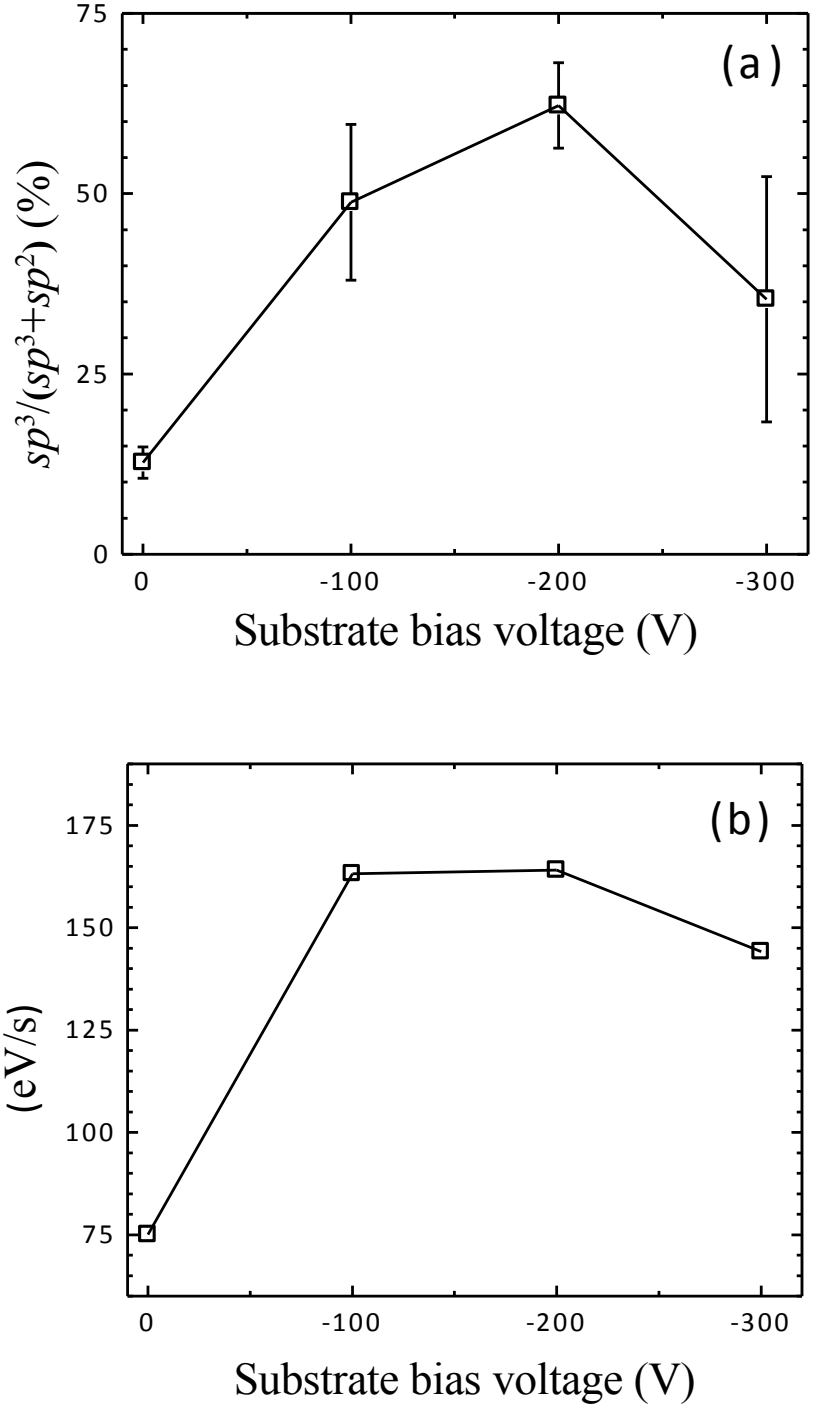

Fig. 3.5 (a) Experimental and (b) analytical results showing the effect of substrate bias voltage on the sp^3 content of *a*-C films deposited under plasma discharge conditions of P_f = 750 W, p = 3 mTorr, f = 20 sccm, and t = 0.4 min.

Chapter 4 The role of duty cycle of substrate pulse biasing in filtered cathodic vacuum arc deposition of amorphous carbon films

4.1 Introduction

According to the Wallace law [Wallace, 1951], the data storage density increases exponentially with the decrease of the distance between the magnetic medium and the read-write element of the magnetic head. Therefore, the carbon overcoat thickness has been greatly reduced in contemporary HDDs [Goglia et al. 2001; Ferrari, 2004; Robertson, 2003; Casiraghi et al., 2004(A); Casiraghi et al., 2004(B); Zhong et al., 2009]. Unfortunately, traditional physical vapor deposition methods, such as the sputtering method introduced in the previous chapter, fail to produce continuous *a*-C films of thickness <5 nm because of the film forming precursors involving is the low energy neutral atoms. Currently, filtered cathodic vacuum arc (FCVA) using ionized film-forming precursors is demonstrated as the only low-temperature deposition method for synthesizing hydrogen-free ultrathin *a*-C films with high sp^3 content, good nanomechanical properties, and high wear resistance [Casiraghi et al., 2004(B); Beghi, 2002].

Increasing demands for HDDs with even higher storage densities (i.e., >10 Tbit/in^2) [Bandic & Victora, 2008; Wood, 2009; Yuan et al., 2009] have motivated the development of new information storage technologies, which are not limited by the superparamagnetic effect, such as heat-assisted magnetic recording (HAMR) [Kryder et al., 2008]. However, repetitive laser heating may destabilize the carbon overcoat structure of HAMR hard disks [Kalish et al., 1999; Grierson et al., 2010]. Recent studies have shown that *a*-C films deposited by FCVA exhibit superior thermal stability under intense and rapid thermal heating and cooling conditions [Wang & Komvopoulos, 2011], which may be attributed to the predominantly sp^3-hybridized structure of the resulting *a*-C films.

The film precursors in FCVA are energetic C^+ ions as opposed to atoms and/or clusters of atoms in traditional physical and chemical vapor deposition methods. Thus, depending on the FCVA deposition conditions (e.g., pulsed bias voltage), C^+ ion bombardment of the substrate surface results in deposition alternating with direct and recoil implantation. In view of the high-quality plasmas generated by FCVA, the ion bombardment energy can be easily modulated by applying a bias voltage to the substrate, which increases the ion kinetic energy. High-energy ions can sputter off atoms from the film surface, producing thinner films compared to less energetic ions [Zhang & Komvopoulos, 2008]; however, highly intense ion bombardment may be detrimental to the integrity of the film structure. For example, while high C^+ ion energy intensifies the collisions between impinging carbon ions and surface carbon atoms, thus enhancing sp^3 hybridization, it can also induce thermal relaxation, which is conducive to sp^2 hybridization and $sp^3 \rightarrow sp^2$ re-hybridization. Because of these competing processes, there is an optimum C^+ ion kinetic energy (typically, ~120 eV) for depositing *a*-C films with high sp^3 content [Pharr et al., 1996; Robertson, 2002]. Changes in the ion kinetic energy may also be detrimental to the film properties [Brown, 1998; Robertson, 2002; Zhu et al., 2008; Zhang & Komvopoulos, 2009].

Therefore, controlling the film thickness and properties by adjusting the ion incidence angle and/or duty cycle of substrate pulse biasing are more desirable approaches because the resulting effect on the film structure is secondary compared to the ion kinetic energy. While the effect of the ion incidence angle on the roughness and structure of FCVA *a*-C films has been examined [Wang & Komvopoulos, 2012], a comprehensive study of the duty cycle effect on the quality of *a*-C films deposited under FCVA conditions of substrate pulse biasing has not been reported yet.

There are two main advantages of substrate pulse biasing compared to dc biasing. First, the surface potential of a non-conductive film can be controlled by applying a pulsed bias voltage, whereas dc bias produces surface charges resulting in significantly different surface potential than the applied bias voltage [Wang et al., 2010]. Second, substrate pulse biasing enables the adjustment of the duty cycle of pulsed bias voltage (defined as the ratio of the time of substrate biasing to the pulsed bias period) so that to control the contributions of ion bombardment and deposition, which significantly affect the film/substrate interface characteristics and overall film properties.

The effect of the duty cycle of substrate pulse biasing on the growth and properties of films deposited by sputtering [Wang et al., 2010], ion plating [Hsu et al., 2010], plasma immersion ion implantation [Zeng et al., 2000], plasma-enhanced chemical vapor deposition [Kumar et al., 1999], and FCVA [Anders et al., 1994] has been the objective of several earlier studies [Anders et al., 1994; Sheeja et al., 2002; Wu et al., 2007]. According to the subplantation mechanism [Lifshitz et al., 1990], energetic ion bombardment due to substrate pulse biasing leads to the formation of a three-layer film structure consisting of interface, bulk, and surface layers [Zhu et al., 2008; Siegal et al., 2000; Davis et al., 1995; Davis et al., 1998]. Therefore, the properties of thin films deposited by FCVA are expected to differ from those of thick films due to the more pronounced effects of the interface and surface layers to the overall film properties compared to thick FCVA films. Despite valuable information about the effect of substrate pulse biasing on carbon film growth derived from previous investigations, the reported results are for relatively thick films (>30 nm) and insight into the duty cycle effect on the film structure is sparse. Therefore, an in-depth investigation of the duty cycle effect on the structure and properties of ultrathin *a*-C films deposited under FCVA conditions of substrate pulse biasing is of high scientific and technological interest.

The principal objective of this study is to elucidate the dependence of the structure, composition, thickness, residual stress, and roughness of ultrathin *a*-C films deposited by FCVA on the duty cycle of substrate pulse biasing. The film surface topography (roughness) and cross-sectional structure were examined by atomic force microscopy (AFM) and high-resolution transmission electron microscopy (HRTEM), respectively, whereas the overall and cross-sectional elemental film structure were studied by analytical Raman spectroscopy and electron energy loss spectroscopy (EELS), respectively, and the average film stress was determined based on the curvature method. Results are contrasted to elucidate the effect of duty cycle of substrate pulse biasing on the quality of ultrathin *a*-C films, to determine the optimum duty cycle for FCVA film deposition under optimum substrate bias voltage conditions [Anders et al., 1994; Zhang & Komvopoulos, 2009], and to provide insight into the minimum thickness of *a*-C films that could be achieved under such FCVA conditions.

4.2 Experimental procedure

4.2.1 Film deposition

Silicon substrates (10 × 10 mm^2) cut from commercially available p-type Si(100) wafers were cleaned by rinsing in acetone for 10 min and isopropanol also for 10 min before coating with ultrathin *a*-C films in a custom-made FCVA system [Zhang & Komvopoulos, 2008 & 2009]. Briefly, film deposition comprised the following main steps: (i) the vacuum chamber was pumped down to a low base pressure (<5 × 10^{-7} Torr) to remove any residual gases adsorbed onto the chamber walls, (ii) Ar gas was introduced into the chamber until the working pressure increased to 2 × 10^{-4} Torr, (iii) the Si substrate was subjected to a 2-min bombardment of 500-eV Ar^+ ions (generated by a 64-mm Kaufman ion source) impinging onto the silicon substrate at a 60° incidence angle from the normal to the substrate surface to remove the native SiO_2 layer, (iv) the base pressure was decreased to <5 × 10^{-7} Torr, and (v) plasma arcing was induced at the cathode (99.99% pure graphite) surface by a mechanical striker. The plasma was stabilized by applying to the cathode a cusp-configuration magnetic field [Zhang & Komvopoulos, 2008]. The magnetic field generated by out-of-plane S-shaped electromagnetic coils was used to inhibit the deposition of macroparticles and/or droplets ejected from the cathode. The current of the auxiliary, upstream, and downstream coils was set at 30.5, 30.9, and 29.6 A, respectively, as in previous studies [Zhang & Komvopoulos, 2008; Zhang & Komvopoulos, 2009; Zhang & Komvopoulos, 2012]. Under these current plasma conditions, only high-purity (~99.99%) C^+ ions are produced at the filter exit. In all film depositions, the ion incidence angle was equal to 90^o (i.e., ion impingement perpendicular to the film surface), the ion flux was set at 1.48 × 10^{19} ions/m^2s, and the deposition time was fixed at 30 s, i.e., constant ion dose of 4.44 × 10^{20} ions/m^2. To control the C^+ ion energy during film deposition, an optimum pulsed bias voltage of –100 V [Anders et al., 1994; Robertson, 2002; Zhang & Komvopoulos, 2008; Zhang & Komvopoulos, 2009] was applied to the substrate, which was rotated at 60 rpm to enhance the film uniformity.

4.2.2 Microanalysis methods

As we are investigating the ultrathin carbon films with thickness on order of several nm, conventional thickness measurement methods such as mechanical stylus, ellipsometry cannot meet the requirements in terms of resolution. Thus, Cross-sections of films deposited at duty cycles in the range of 50-95% were examined with the high-resolution TEM (Tecnai) to measure the film thickness. Details about the TEM sample preparation and the TEM system can be found in chapter 2.

The film structure was also examined with a 514.5-nm Ar^+ ion laser Raman spectroscope. Raman spectra were recorded in the range of 850–1950 cm^{-1}. After background noise subtraction, the spectra were deconvoluted by fitting two Gaussian distributions at the *D* peak and *G* peak [Robertson, 2002]. For statistical analysis, Raman spectra were collected from at least three different locations on each film surface. Details about the Raman spectroscope can be found in chapter 2.

4.2.3 Roughness and thickness measurements

Film roughness measurements were obtained from 2 × 2 μm^2 images acquired with an AFM (NanoScope II, Digital Instruments) operated in the tapping mode. All AFM scans were performed with sharp Si tips of nominal radius of curvature equal to ~10 nm. For statistical analysis, the root-mean-square (rms) roughness was calculated as the mean value of at least four measurements obtained from different AFM surface scans of each film.
The thickness of each layer in the multilayer cross-sectional film architecture was determined from cross-sectional EELS analysis. To validate the thickness measurement approach, measurements of the total thickness (i.e., sum of all layer thicknesses) obtained from three different cross-sectional HRTEM images of each film were compared with total thickness measurements obtained from EELS.

4.2.4 Residual stress measurement

In these studies, 4-inch-diamter p-type Si(100) wafers were used to deposit 50-nm-thick *a*-C films under FCVA conditions identical to those of the thinner *a*-C films. The residual stress σ in the films deposited under FCVA conditions of different duty cycles of –100 V substrate bias voltage was obtained from Stoney's equation (Eq. 2.7 in Chapter 2).

4.3 Results and discussion

4.3.1 Cross-sectional structure

Fig. 4.1 shows cross-sectional HRTEM images of *a*-C films for different duty cycles of substrate pulse biasing. (The different layers in each cross-sectional image are distinguished by white interfaces and labeled in Fig. 4.1(d).) The periodic array in the top region (1) of all images is indicative of the single-crystal Si(100) substrate. The structure periodicity decreases close to the interface of the Si(100) substrate with the intermixing layer (2) and, eventually, disappears into the film (3), revealing an amorphous structure for both the intermixing layer and the carbon film. Structure and contrast differences in the HRTEM images reveal a three-layer specimen architecture consisting of crystalline Si(100) substrate, intermixing layer, and *a*-C film. The Au capping layer (4) and epoxy glue (5) are also visible in all the images. A comparison of the HRTEM images shown in Fig. 4.1 indicates that the thinnest *a*-C films correspond to a duty cycle of substrate pulse biasing of 65% (Fig. 4.1(b)).

4.3.2 Composition

The overall composition of the film structures shown in Fig. 4.1 was examined by visible Raman spectroscopy. This method can be used to interpret sp^3 hybridization because it preferentially excites the π states existing only in sp^2 hybridizations. Fig. 4.2 shows Raman spectra of *a*-C films for a duty cycle of substrate pulse biasing in the range of 50 to 95%. The spectra were fitted with two Gaussian distributions assigned to *D* and *G* peaks centered at ~1350 and ~1550

cm^{-1}, respectively. The position and intensity of the *D* and *G* peaks in visible Raman spectra can be affected by several factors, including sp^2 cluster size, bond-length/angle disorder, and sp^2/sp^3 ratio.

Fig. 4.3 shows the *G*-peak position and FWHM versus duty cycle of substrate pulse biasing. It is known that the decrease of the sp^3 fraction correlates with the shift of the *G* peak to higher wavenumbers [Chung et al., 2007; Shin et al., 2001] and that the *G*-peak FWHM increases with the film density [Rose et al., 2014]. Fig. 4.3(a) indicates that the *a*-C film with the highest sp^3 fraction corresponds to a 75% duty cycle, whereas Fig. 4.3(b) shows that the highest *G*-peak FWHM corresponds to a 75% duty cycle. These results suggest that *a*-C films deposited under FCVA substrate pulse biasing conditions of 75% duty cycle have the highest sp^3 content.

More direct and detailed information about the cross-sectional composition of FCVA *a*-C films can be obtained from analytical EELS, which uses the energy loss of electrons passing through the specimen to determine the chemical composition and structure. Electron energy loss is mainly due to inelastic electron-electron collisions [Williams & Carter, 2009; Egerton, 2011]. Beam electrons interacting with electrons of the conduction and/or valence bands of the specimen material are detected in the low-energy-loss range (<50 eV), whereas the high-energy-loss range (>50 eV) provides information about inelastic interactions between beam electrons and inner (core-shell) electrons. Therefore, information about the elemental composition can be extracted from ionization edges.

Fig. 4.4 shows high-energy-loss spectra of C K-edge obtained from different locations across the Si(100)/a-C interface for a duty cycle of substrate pulse biasing equal to 75%. The location corresponding to each spectrum is indicated by a circle in the STEM image shown on the right of Fig. 4.4. Following background subtraction, all spectra were calibrated by centering the π^* peak at 285 eV. As expected, spectrum (a) is featureless because it corresponds to the Si(100) substrate. Spectra (b) and (c) consist of a well-defined π^* peak and a small σ^* peak, indicating the presence of carbon in the intermixing layer, whereas spectra (d) and (e) reveal high carbon concentration in the bulk *a*-C film. Spectrum (f) shows a decrease in carbon intensity and increased contribution of the π^* peak, indicating that the film surface is rich in sp^2 hybridization. Spectrum (g) does not show any carbon signal because it is from the Au capping layer, while spectrum (h) shows the existence of a strong π^* peak and a relatively weak σ^* peak revealing the presence of carbon, which is expected because this spectrum corresponds to the epoxy layer.

Fig. 4.5 shows a representative high-energy-loss spectrum of C K-edge obtained from the bulk layer of *a*-C film deposited under FCVA conditions of 75% duty cycle of substrate pulse biasing. The location corresponding to the spectrum is marked by a circle in the STEM image shown on the right. Similar EELS spectra were obtained in the range of 280–305 eV and were analyzed to determine the sp^2 and sp^3 fractions in the *a*-C film. The pre-edge peak at 285 eV is due to the excitation of electrons from the ground-state 1s core level to the vacant π^*-like anti-bonding states, whereas electron excitations to the higher lying σ^* states occur above 290 eV [Cuomo et al., 1991]. The π^* peak is fitted with a Gaussian distribution, while the σ^* peak is integrated in the small energy range from 290 to 305 eV to minimize plural scattering effects. The area ratio of these two peaks is proportional to the relative number of π^* and σ^* orbitals, which is 1/3 for 100% sp^2 and 0/4 for 100% sp^3.

The fraction x of sp^2 bonded carbon atoms is given by [Cuomo et al., 1991]

$$\frac{(\pi^*/\sigma^*)_{\text{film}}}{(\pi^*/\sigma^*)_{\text{std}}} = \frac{3x}{4-x} \tag{4.2}$$

where the standard (std) sample is graphitized evaporated carbon with 100% sp^2 carbon bonding.

Fig. 4.6 shows the effect of duty cycle of substrate pulse biasing on normalized carbon intensity obtained by integrating the EELS spectrum from 280 to 305 eV and sp^3 depth profiles calculated from the C K-edge spectra using Eq. 4.2. After background subtraction, all C K-edge spectra were calibrated by centering the π^* peak at 285 eV. Regardless of the duty cycle of substrate pulse biasing, the sp^3 fraction and carbon concentration reveal the existence of six distinct regions: (i) *substrate* – the carbon signal intensity is almost zero because the signal is from the Si(100) substrate; (ii) *interface layer* – the carbon concentration increases sharply, whereas the sp^3 fraction increases moderately; (iii) *buffer layer* – the carbon intensity further increases, while the sp^3 content increases sharply, consistent with previous studies [Davis et al., 1995, Wang & Komvopoulos, 2013]; (iv) *bulk layer* – the carbon concentration stabilizes at ~100% and the sp^3 fraction remains almost constant; (v) *surface layer* – both carbon concentration and sp^3 fraction decrease sharply; and (vi) *capping layer* – the low-intensity carbon signal is attributed to adventitious carbon. It is noted that the intermixing layer (layer (2) in Fig. 4.1) consists of interface and buffer layers. The various interfaces were determined from the normalized C-K edge intensity, the sp^3 content, or the slope of the sp^3 depth profile (Table 4.1).

Fig. 4.7 shows the average sp^3 fraction in the bulk layer of *a*-C films versus duty cycle of substrate pulse biasing. The sp^3 content increases with the increase of duty cycle up to 75%, thereafter remaining relatively constant. This trend is attributed to energetic C^+ ions impinging onto the growing film surface. Ion bombardment results in film densification and the development of a compressive mechanical environment, which is conducive to sp^3 hybridization. Because in all deposition experiments the total number of C^+ ions impinging onto the film surface was fixed (ion dose = 4.44×10^{20} ions/m^2) and the duty cycle affects only the fraction of low- and high-energy C^+ ions, the fraction of high-energy C^+ ions impinging onto the film surface under fixed substrate bias voltage conditions increased with the duty cycle, thereby enhancing sp^3 hybridization. The variation of sp^3 hybridization with duty cycle of substrate pulse biasing shown in Fig. 4.7 is consistent with the interpretation of the Raman spectra (Figs. 4.2 and 4.3).

4.3.3 Thickness

Fig. 4.8 shows the thickness of different layers (measured from Fig. 4.6) comprising the multilayer film structure versus duty cycle of substrate pulse biasing. The sum of the thicknesses of the surface, bulk, buffer, and interface layers is referred to as the total thickness. The fairly good agreement between HRTEM and EELS results of the total thickness validates the thickness measurement approach used in this study. The minimum total thickness (~10 nm) corresponds to a 65% duty cycle, which is consistent with HRTEM imaging (Fig. 4.1) and EELS analysis (Fig. 4.6). Importantly, the 65% duty cycle also produces the thinnest (~3.9 nm) bulk layer, whereas the 75% duty cycle yields the thickest (~5.7 nm) intermixing layer consisting of ~2.7-nm-thick interface layer and ~3.0-nm-thick buffer layer. These results indicate that ion sputtering and

subplantation are particularly effective under FCVA conditions corresponding to a duty cycle of 65% and 75%, respectively. Table 4.2 gives the total *a*-C film thickness measured from HRTEM images and cross-sectional EELS spectra.

The variation of the film thickness with duty cycle of substrate pulse biasing shown in Fig. 4.8 and Table 4.2 can be explained by considering the simultaneous effects of deposition, direct/recoil implantation, and sputtering. Although the C+ ion flux and deposition time were fixed, the time ratio of high- to low-energy ion bombardment increased with the duty cycle, affecting the contributions of former processes. The fraction of high-energy ions impinging onto the film surface during a pulse period increases with the duty cycle while the fraction of low-energy ions decreases. High-energy ions enhance direct/recoil implantation and sputtering, whereas low-energy ions favor deposition. Direct/recoil implantation pushes carbon atoms to deeper locations increasing the film thickness, whereas sputtering removes surface carbon atoms, resulting in the decrease of film thickness. Because of the different effects of duty cycle of substrate pulse biasing on the deposition, implantation, and sputtering processes, deposition and sputtering dominated film growth in the 50%–65% duty cycle range, whereas direct/recoil implantation was the dominant process in the 65%–95% duty cycle range.

4.3.4 Residual stress

Further insight into the duty cycle effect on the quality of FCVA *a*-C films can be obtained from residual stress measurements. The film stress can be correlated to the dominant mode of carbon atom hybridization. According to the subplantation mechanism, the origin of the compressive residual stress is the penetration of the *a*-C film surface by energetic C^+ ions undergoing quenching at deeper locations and resulting in localized density gradients conducive to sp^3 hybridization. Consequently, the higher the sp^3 fraction of *a*-C films, the higher the compressive residual stress [Robertson, 2002; McKenzie et al., 1991; Davis, 1993]. Fig. 4.9 shows the residual stress of *a*-C films versus duty cycle of substrate pulse biasing. The residual film stress intensifies with the increase of the duty cycle up to 75% and thereafter remains relatively constant. This trend is in good agreement with the variation of the sp^3 fraction in the bulk layer of *a*-C films (Fig. 4.7) and previous studies reporting a correlation between residual film stress and sp^3 fraction [Shin et al., 2001; Robertson, 1994(A)].

4.3.5 Roughness

In addition to the structure and composition, the roughness of the carbon overcoat is also of critical importance because it controls the probability of asperity-asperity interaction at the head-disk interface. Both the intensity and frequency of asperity contact events increase with film roughness. Fig. 4.10 shows the rms roughness of *a*-C films versus duty cycle of substrate pulse biasing. The film roughness increases with the increase of duty cycle above 65% because longer time of substrate biasing during the pulse period enhances sputter etching of the film (i.e., roughening) by impinging C^+ ions. Alternatively, film roughening under FCVA conditions of relatively low duty cycle (i.e., 50%) is due to the dominance of film deposition. A balance between sputtering and deposition occurs for 65% duty cycle, resulting in minimum film

roughness (rms ≈ 0.13 nm), which is essentially equal to the roughness of the Si(100) substrate (rms ≈ 0.12 nm).

The results of this study indicate that *a*-C films of minimal thickness, high smoothness, and predominantly sp^3 hybridized structures can be produced under FCVA deposition conditions of 65% duty cycle of optimum substrate bias voltage (–100 V). This is attributed to the equilibrium of sputtering, direct/recoil implantation, and deposition. These processes can produce different effects on the film structure and properties. Specifically, while the sp^3 fraction and residual compressive stress increase monotonically with the increase of duty cycle, the film thickness and roughness first decrease to a minimum (corresponding to 65% duty cycle) and then increase with further increasing the duty cycle of substrate pulse biasing.

A further decrease in film thickness can be achieved by varying the deposition time and ion incidence angle (set at 30 s and 90^o, respectively, in the present study) and by post-process Ar^+ ion bombardment of the *a*-C films. For example, the thicknesses of the interface, buffer, and bulk layers can be decreased by increasing the ion incidence angle, whereas the thickness of the sp^2-rich surface layer can be reduced by post-deposition Ar^+ ion sputter etching. Results from studies revealing these effects on the thickness and overall quality of *a*-C films deposited by FCVA is presented in the next two chapters.

4.4 Conclusion

The effect of the duty cycle of substrate pulse biasing on the structure, composition, thickness, residual stress, and roughness of FCVA *a*-C films was examined in the light of HRTEM, EELS, Raman, residual stress, and AFM results. It was shown that a 65% duty cycle of substrate pulse biasing produces smoother and thinner *a*-C films with relatively high sp^3 content, whereas a 75% duty cycle of substrate pulse biasing yields *a*-C films with the highest sp^3 content and residual stress and also thicker interface and buffer layers. These findings reveal a strong effect of the duty cycle of substrate pulse biasing on carbon atom hybridization and growth, residual stress, and roughness of FCVA *a*-C films. The results of this study indicate that *a*-C films of thickness only a few nanometers can be deposited under optimum substrate pulse biasing FCVA conditions of 65% duty cycle. Even thinner *a*-C films can be synthesized under optimum FCVA conditions of 65% duty cycle of substrate pulse biasing by adjusting other FCVA process parameters, such as the ion incidence angle, and post-deposition Ar^+ ion sputtering.

Table 4.1 Determination of layer interfaces in *a*-C films by EELS.

Interface	Range
capping layer/surface layer	normalized C-K edge intensity range of 0.3–0.4
surface layer/bulk layer	normalized C-K edge intensity range of 0.85–0.95
bulk layer/buffer layer	normalized C-K edge intensity range of 0.9–1.0
buffer layer/interface layer	change in slope of sp^3 depth profile from 0.3–3.6 to 8.6–17.3 %/nm
interface layer/Si substrate	sp^3 <5% or C-K edge normalized intensity <0.05

Table 4.2 Total film thickness measured from HRTEM images and cross-sectional EELS spectra versus duty cycle of substrate biasing in FCVA deposition. [(a)]

Duty cycle (%)	50	65	75	95
Total film thickness from TEM (nm)	16.51	10.13	14.88	17.79
Total film thickness from EELS (nm)	14.50	10.20	14.70	16.80

[(a)]All other deposition parameters are fixed, i.e., deposition time = 30 s, incidence angle = 90° (measured from to the surface plane), and substrate bias voltage = –100 V.

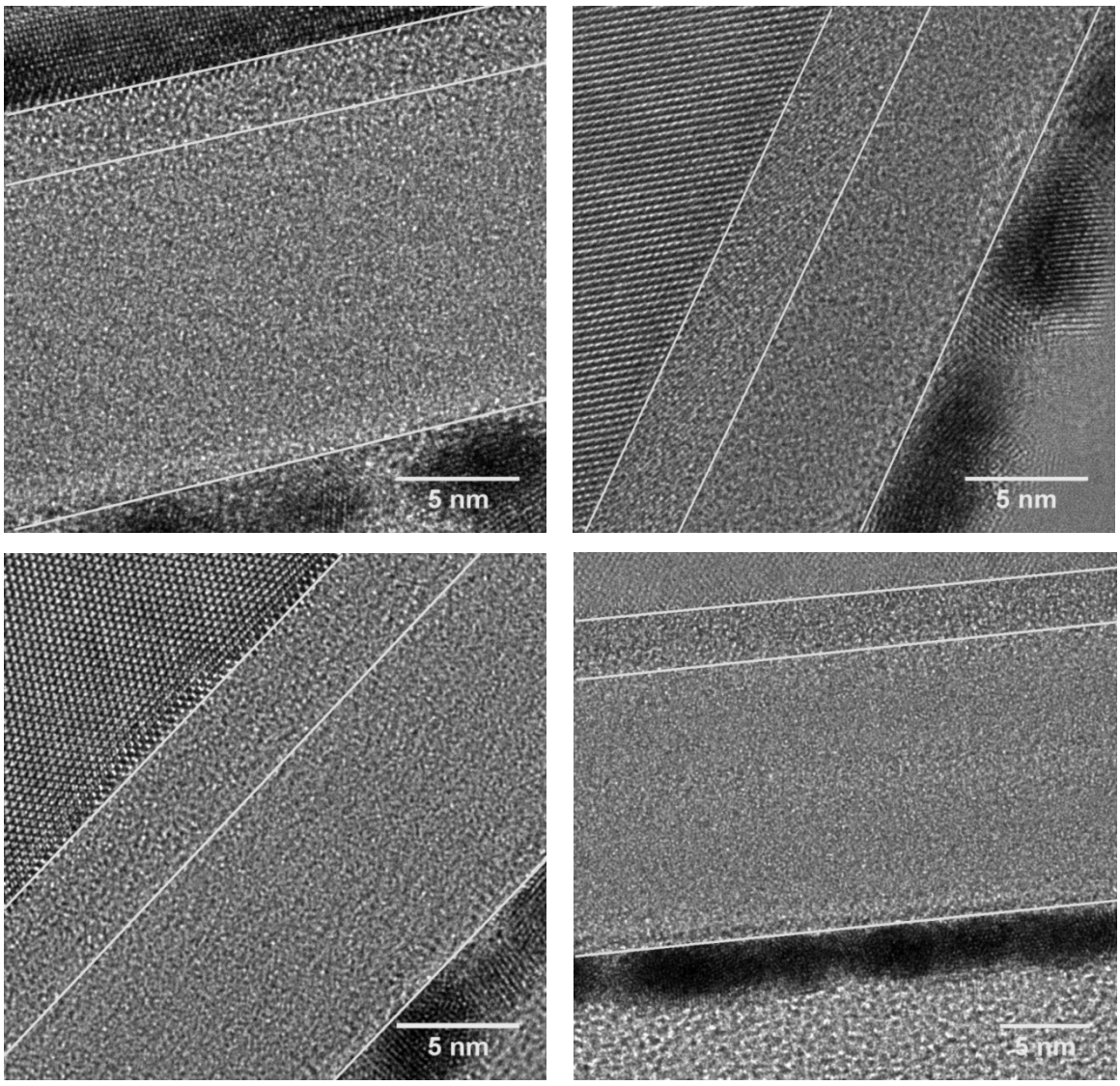

Fig. 4.1 Cross-sectional HRTEM images of *a*-C films deposited under FCVA conditions of duty cycle of substrate pulse biasing equal to (a) 50%, (b) 65%, (c) 75%, and (d) 95%. Contrast and structure differences reveal: (1) Si(100) substrate, (2) intermixing layer, (3) bulk film, (4) Au capping layer, and (5) epoxy mounting material.

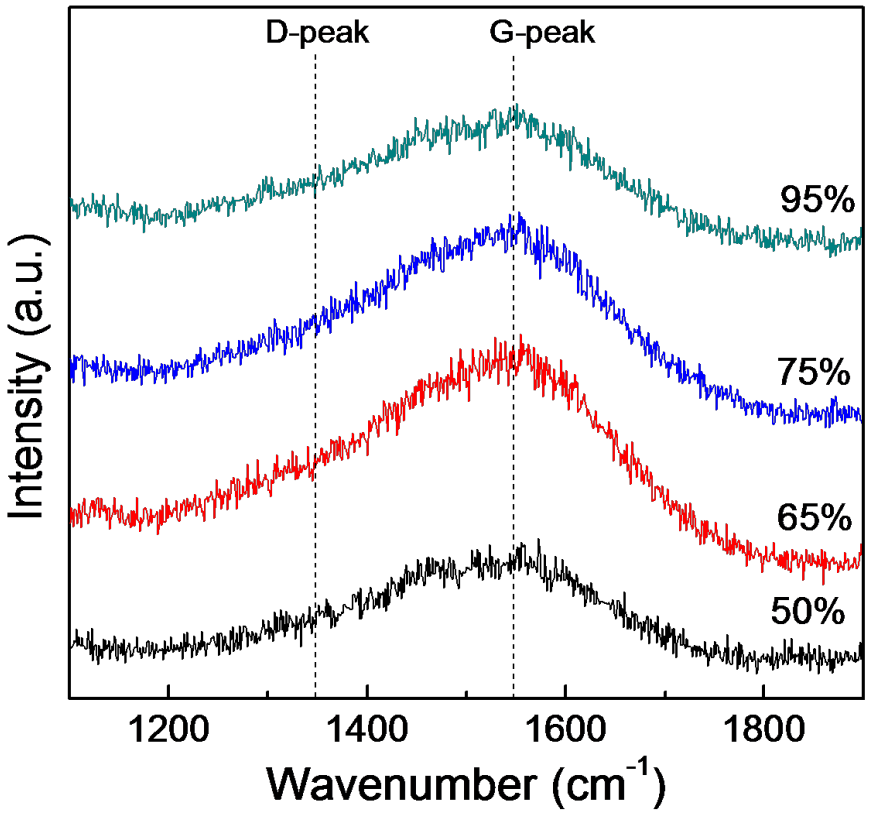

Fig. 4.2 Visible Raman spectra of *a*-C films deposited under FCVA conditions of duty cycle of substrate pulse biasing between 50% and 95%. For clarity, the spectra have been shifted in the vertical direction. The *D*- and *G*-peak positions are shown by dashed lines.

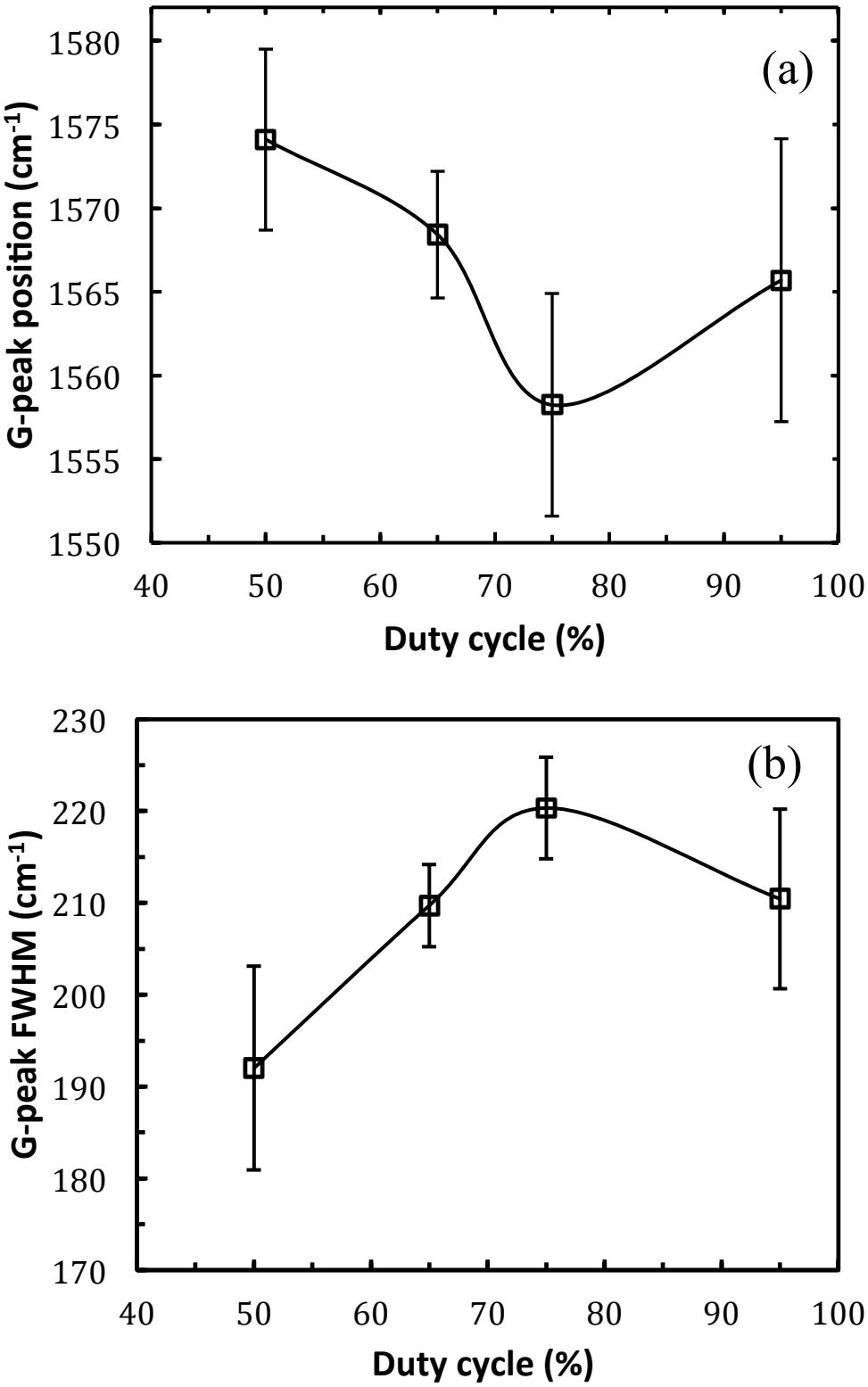

Fig. 4.3 (a) *G*-peak position and (b) *G*-peak FWHM versus duty cycle of substrate pulse biasing.

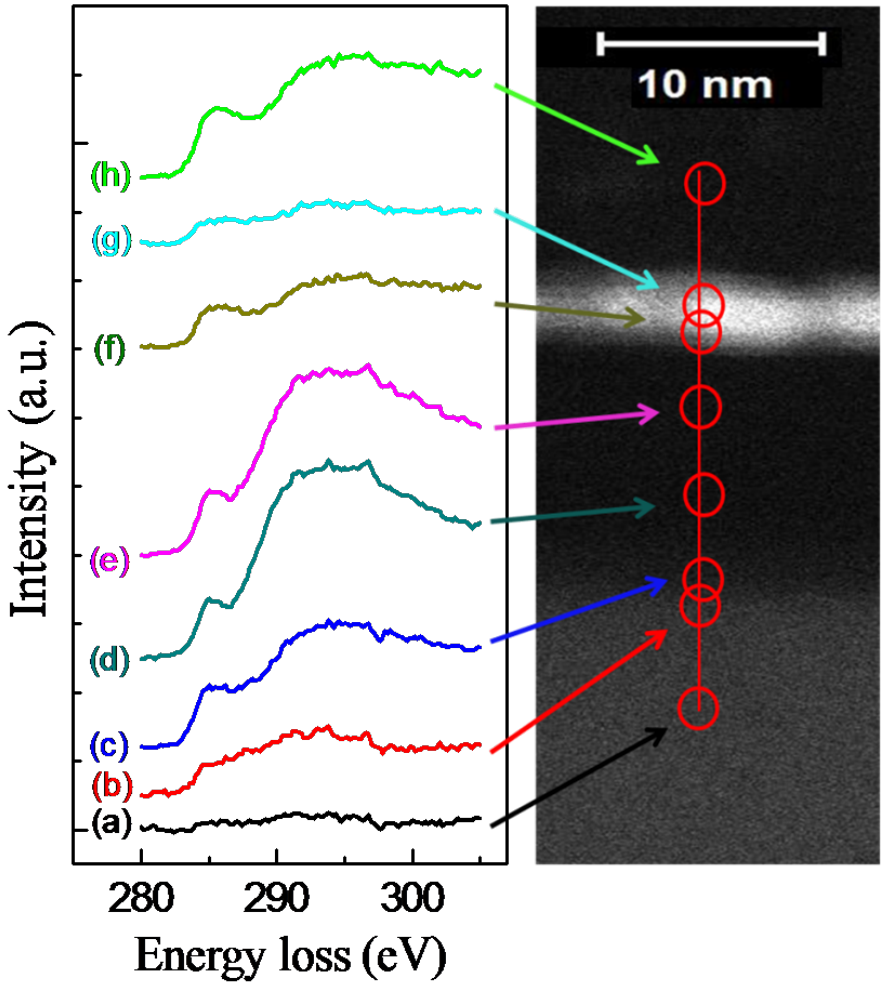

Fig. 4.4 C K-edge EELS spectra obtained from different locations across the interface of Si(100) substrate and *a*-C film deposited under FCVA conditions of 75% duty cycle of substrate pulse biasing. The location corresponding to each spectrum is marked by a circle in the STEM image shown on the right. The spectra were calibrated by shifting the π^* peak of all C K-edge spectra to 285 eV after background subtraction.

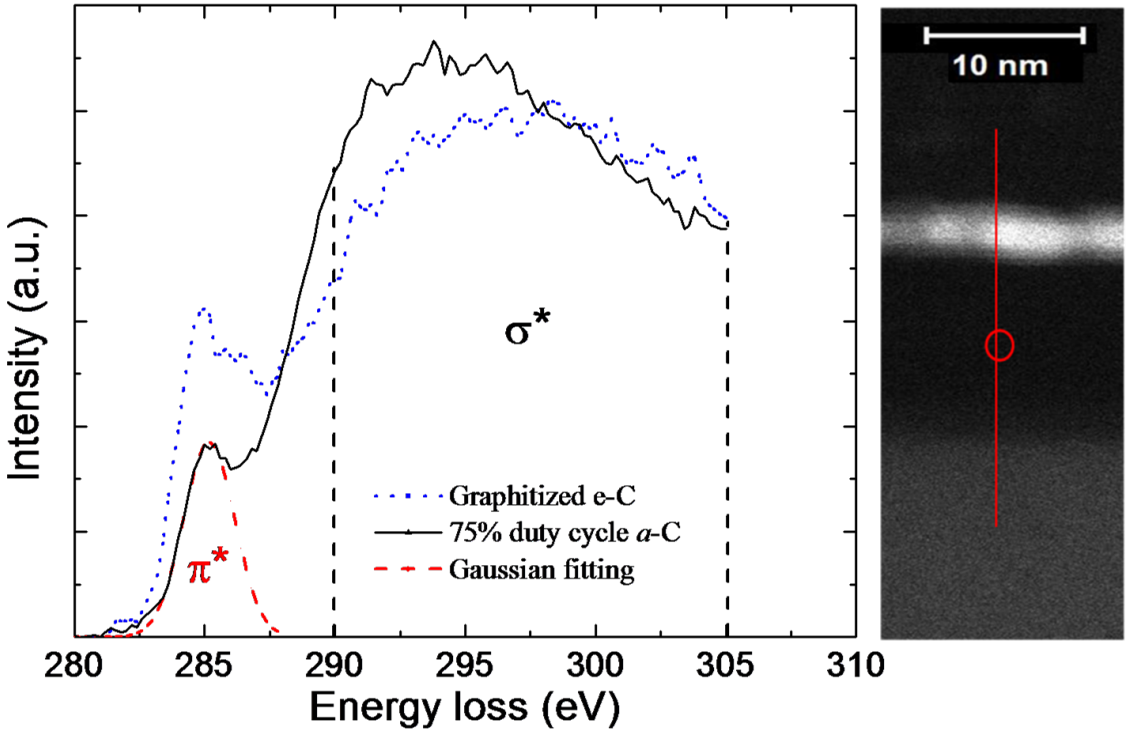

Fig. 4.5 C K-edge EELS spectrum with fitted π^* and σ^* peaks of the bulk layer of *a*-C film deposited under FCVA conditions of 75% duty cycle of substrate pulse biasing. The location from where the spectrum was obtained is marked by a circle in the STEM image shown on the right. The π^* peak is represented by a Gaussian distribution from 282 to 287.5 eV, whereas the σ^* peak is defined as the spectrum in the energy loss range of 290–305 eV. The spectrum of the standard sample (graphitized evaporated carbon (e-C) with 100% sp^2 carbon bonding) is also shown for comparison.

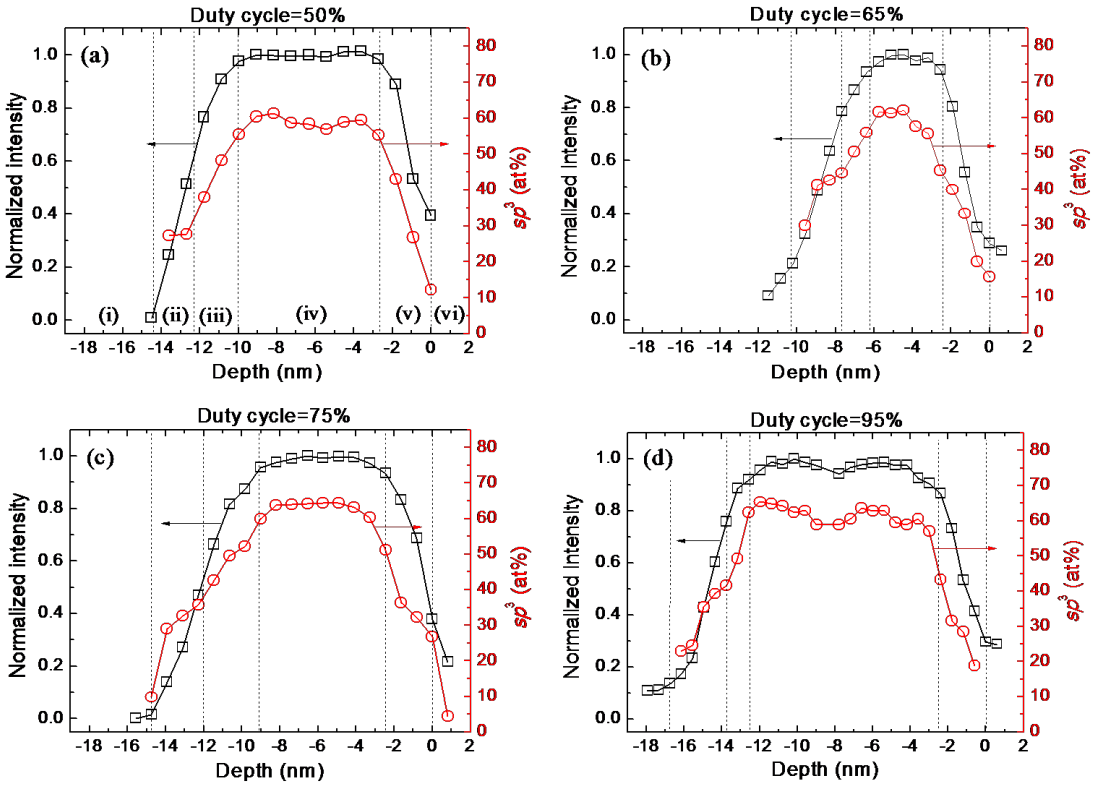

Fig. 4.6 Depth profiles of C-K edge normalized intensity and sp^3 fraction calculated from C K-edge EELS spectra of *a*-C films deposited under FCVA conditions of duty cycle of substrate pulse biasing equal to (a) 50%, (b) 65%, (c) 75%, and (d) 95%. The boundaries between neighboring regions are indicated by dashed lines.

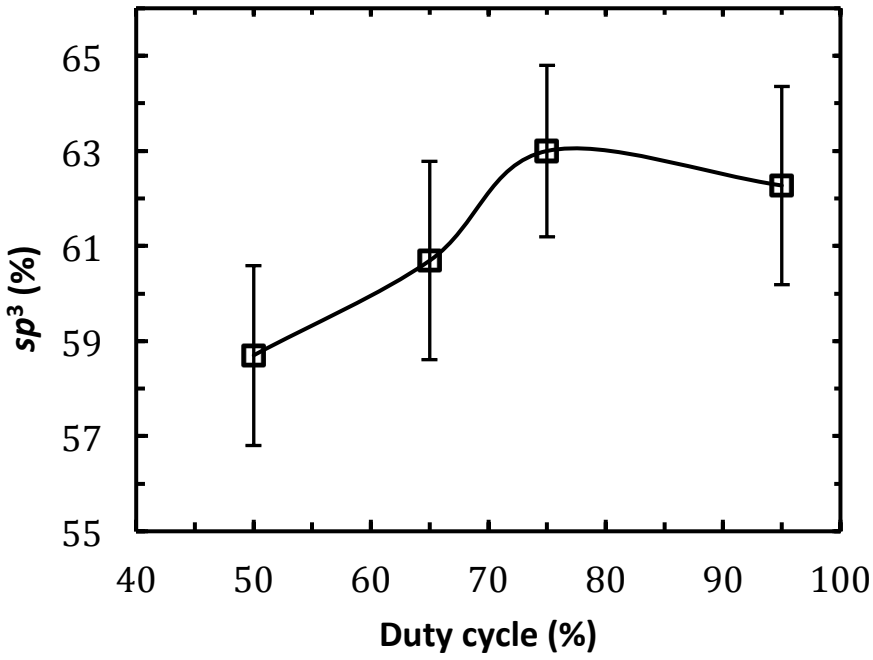

Fig. 4.7 Variation of sp^3 fraction of *a*-C films with duty cycle of substrate pulse biasing.

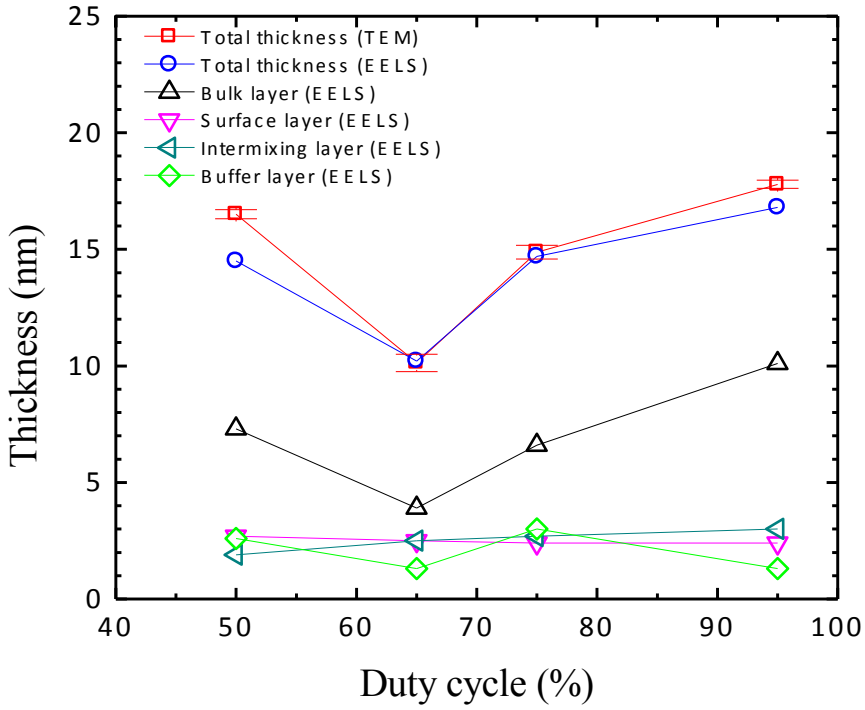

Fig. 4.8 Total thickness determined from HRTEM and EELS analyses and thickness of interface, buffer, bulk, and surface layers determined from EELS analysis versus duty cycle of substrate pulse biasing.

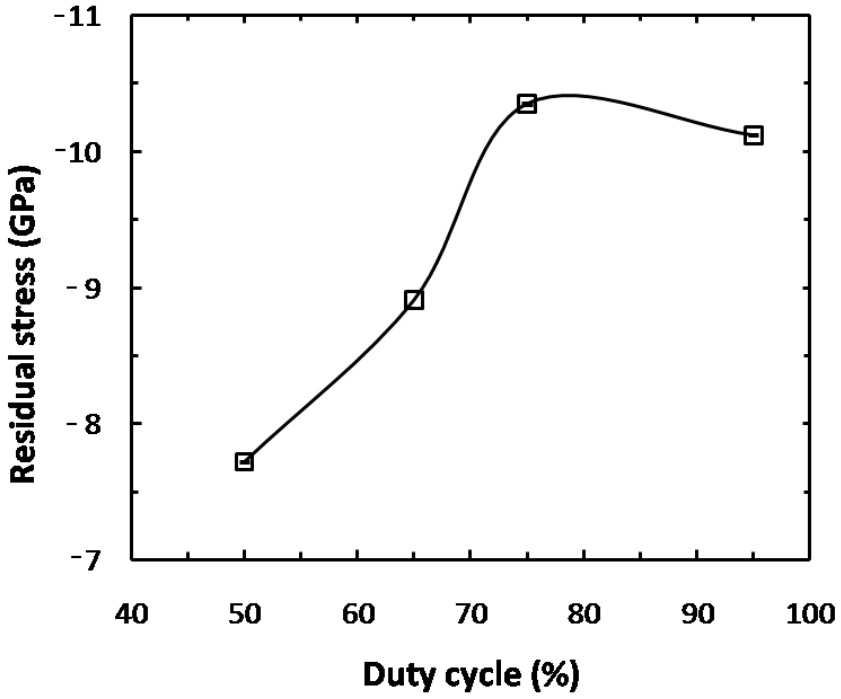

Fig. 4.9 Residual stress of *a*-C films versus duty cycle of substrate pulse biasing.

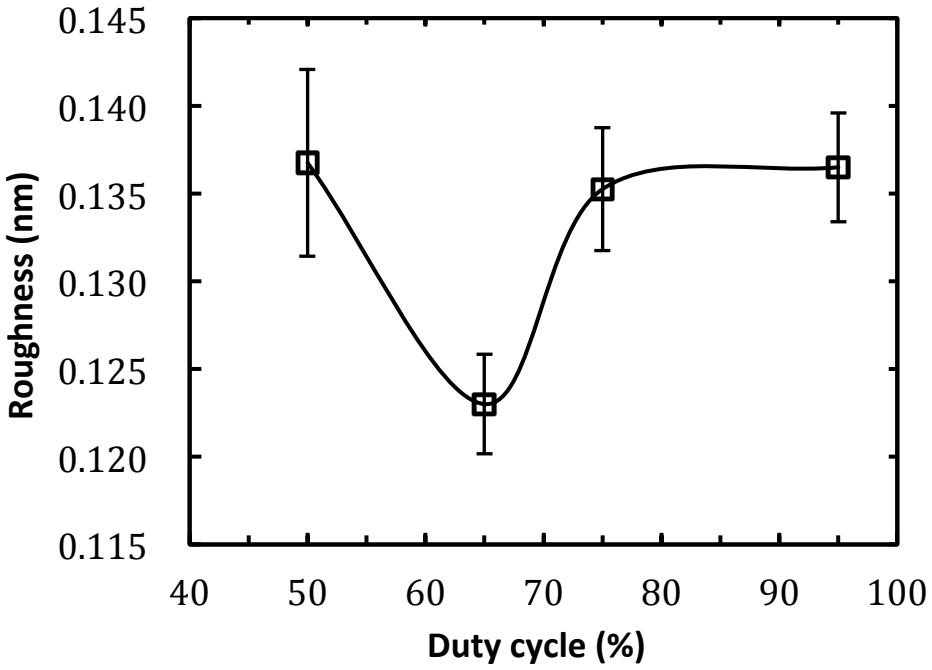

Fig. 4.10 Roughness (rms) of *a*-C films versus duty cycle of substrate pulse biasing.

Chapter 5 The effect of Argon ion beam irradiation on the thickness and structure of ultrathin amorphous carbon films

5.1 Introduction

The characteristics of *a*-C films strongly depend on the dominance of trigonal (sp^2) or tetrahedral (sp^3) atomic carbon hybridization. To evaluate the performance of *a*-C films as protective overcoats, dense and hard *a*-C films possess high sp^3 contents in general, considered to result in better protection. The type of atomic carbon hybridization in *a*-C films greatly depends on the process conditions and method of film deposition. Plasma-enhanced chemical vapor deposition (PECVD) and filtered cathodic vacuum arc (FCVA) are effective methods for depositing ultrathin *a*-C films. [Grill & Meyerson, 1994; Robertson, 2001; Anders, 2008] However, the structure, thickness, and properties of the *a*-C films deposited by these methods may significantly vary due to fundamental differences in film growth conditions.

Ultrathin *a*-C films are of particular importance in storage technology, where they are extensively used as protective overcoats of magnetic media and heads. In response to constantly increasing demands for even higher storage densities in magnetic recording, the distance between the magnetic medium of the hard disk and the read/write transducer embedded at the trailing edge of the head has been greatly reduced in contemporary hard-disk drives. This has been largely accomplished by depositing ultrathin *a*-C overcoats on the disk and head media mainly by PECVD and FCVA techniques. [Grill & Meyerson, 1994; Robertson, 2001; Anders, 2008; Zhang & Komvopoulos, 2009; Xu et al., 1996] However, extremely small thickness may negatively impact the protective capability of the overcoat. Considering the existence of chemical and structural gradients through the thickness of *a*-C films, which result in a multi-layer cross-sectional structure consisting of interface, bulk, and surface layers with markedly different structures and thicknesses, [Riedo et al., 2000; Wan & Komvopoulos, 2004; Wang & Komvopoulos, 2013] excessive overcoat thinning may yield media with significantly altered mechanical, tribological, and corrosion characteristics. In particular, the decrease of the overcoat thickness may come at the expense of the sp^3-rich bulk layer. An ultrathin (<5 nm) *a*-C film with a very thin bulk layer of thickness comparable to those of the sp^2-rich interface and surface layers implies a decrease in film density and mechanical strength and, presumably, inadequate corrosion and wear resistance. Therefore, reducing the *a*-C film thickness without degrading its protective capability is of paramount importance in contemporary magnetic recording technology.

Ion beam irradiation is a promising post-deposition method for decreasing the overcoat thickness and tuning the film structure *in situ*. Previous studies dealing with post-growth film treatment have focused on the effect of surface modification on the overall film properties. For example, Cheah et al. [Cheah et al., 1999] reported that ion beam irradiation of tetrahedral *a*-C films increased the sp^3 content and the density of sp^3-rich nanoclusters having sp^2-rich boundaries. Patsalas and Logothetidis [Patsalas & Logothetidis, 2000(A) & 2000(B)] irradiated sputtered *a*-C films with 0.5- and 1.5-keV Ar^+ ion beams and observed that sp^2-rich *a*-C films deposited under

floating substrate bias exhibited surface smoothing, densification, and diamond crystallization, whereas sp^3-rich *a*-C films deposited under negative substrate bias voltage demonstrated relatively less change. Silinskas and Grigonis [Silinskas and Grigonis, 2002] reported that exposure of hydrogenated *a*-C (*a*-C:H) films to low energy (0.1–0.7 keV) Ar^+ ion beams caused damage to the graphite clusters and sputter etching of the graphite phase; in particular, *a*-C:H films of thickness <300 nm became more diamond-like and their graphite clusters exhibited more disordering. Vinnichenko et al. [Vinnichenko et al., 2004] observed that 15-min Ar^+ ion beam irradiation of 10-nm-thick *a*-C films deposited by FCVA under a substrate bias voltage of –500 V decreased the film thickness without altering the surface roughness.

The aforementioned studies and several others in the literature indicate that understanding of the effect of Ar^+ ion beam irradiation on the structure and thickness of ultrathin *a*-C films is rather sparse. In particular, a comprehensive study of the changes in carbon atom hybridization and thickness of interface, bulk, and surface structural layers of *a*-C films of thickness <5 nm due to the effect of ion beam irradiation has not been performed yet. Such study requires the use of high-resolution techniques, such as transmission electron microscopy (TEM) and electron energy loss spectroscopy (EELS). The high spatial and energy resolution of EELS makes it suitable for measuring the atomic carbon distribution and sp^3 content through the thickness of ultrathin *a*-C films and, consequently, identify changes in the structure and thickness of structural layers.

The objective of this investigation is to elucidate the effect of Ar^+ ion beam irradiation on the thickness and structure of ultrathin carbon films deposited by PECVD and FCVA. Changes in through-thickness carbon concentration and hybridization as well as film thickness were studied by high-resolution TEM (HRTEM) and cross-sectional EELS. Results from these analyses are contrasted to show differences between ultrathin films deposited by PECVD and FCVA, elucidate the effect of Ar^+ ion beam irradiation on the quality of the produced films, and provide insight into the decrease of film thickness by post-deposition Ar^+ ion beam irradiation.

5.2 Experimental procedure

5.2.1 Film deposition

Glass disks of 2.5-in. diameter coated with a ~100-nm-thick NiTa layer were cut into 1 × 1 cm^2 pieces, which were then used as substrates. Ultrathin (~5 nm) *a*-C:H films were deposited onto the NiTa/glass substrates by PECVD using acetylene (C_2H_2) as the film precursor. The density (obtained from X-ray reflectivity measurements using a standard procedure) and hydrogen content of the PECVD *a*-C films, as determined by the manufacturer, are equal to ~2.0–2.1 g/cm^3 and 30–40 at%, respectively.

To deposit *a*-C films on similar substrates by FCVA, NiTa/glass substrates coated with a PECVD *a*-C film were loaded onto the substrate stage of a custom-made FCVA system [Zhang & Komvopoulos, 2008; Zhang & Komvopoulos, 2009] and the film was removed by sputter etching with a 500-eV Ar^+ ion beam generated by a 64-mm Kaufman ion source (Commonwealth Scientific, Alexandria, VA) at a working pressure of ~2 × 10^{-4} Torr and Ar^+ ion incidence angle (measured from the normal to the substrate surface) equal to 60^o. Under these

sputtering conditions, the PECVD *a*-C film is completely removed after 6 min of Ar^+ ion bombardment, as confirmed by X-ray photoelectron spectroscopy full-spectrum scanning shown in Fig. 5.1. After allowing the chamber to cool down for 5 min and the base pressure to decrease to $<5 \times 10^{-7}$ Torr, plasma arcing at the cathode (99.99% pure graphite) surface was initiated by a mechanical striker, while the substrate stage was oriented normal to the C^+ ion flux. An optimum pulsed bias voltage of –100 V and frequency of 25 kHz was used to control the C^+ ion energy during film synthesis by FCVA. To produce ultrathin *a*-C films of similar thickness with those deposited by PECVD, the deposition time was fixed at 12 s. For uniform sputter etching and film deposition in the radical direction, the substrate stage was rotated at 60 rpm during both ion beam irradiation and FCVA deposition. Details on the FCVA deposition system are described in the Chapter 4.

5.2.2 Post deposition Ar^+ ion beam irradiation

The *a*-C films were sputter etched in the same FCVA chamber with a 500-eV Ar^+ ion beam under a working pressure of $\sim 2 \times 10^{-4}$ Torr and ion beam incidence angle (measured from the normal to the substrate surface) equal to 60^o. The beam voltage was fixed at 17 mA, while the etching time was set equal to 2 or 4 min.

5.2.3 Microanalysis methods

Cross-sections of films deposited by PECVD and FCVA were examined with the high-resolution TEM (Tecnai) to measure the film thickness. Details about the TEM sample preparation and the TEM system can be found in chapter 2.

The cross-sectional elemental composition of the *a*-C films was investigated by analytical EELS. For carbon atoms, the range of the characteristic K-edge spectra for determining the sp^2 and sp^3 fractions of *a*-C films is from 280 to 305 eV. The pre-edge peak at 285 eV is due to the excitation of electrons from the ground-state 1s core level to the vacant π^*-like anti-bonding states, whereas the edge from 290 eV is due to the excitation of electrons from the 1s core level to the σ^* states. [Cuomo et al., 1991] Therefore, information about the elemental composition can be extracted from the ionization edges. The π^* peak is fitted with a Gaussian distribution, while the σ^* peak is integrated in the energy range from 290 to 305 eV, to minimize plural scattering effects. The area ratio of these two peaks is proportional to the relative number of π^* and σ^* orbitals, which is 1/3 for 100% sp^2 and 0/4 for 100% sp^3. Therefore, the fraction x of sp^2 bonded carbon atoms in the *a*-C films can be obtained by using Eq. 4.2. [Cuomo et al., 1991] More details about the curve fitting method and calculation of the sp^3 fraction are given in Chapter 4.

5.3 Results and discussion

To determine the amount of carbon removed by Ar^+ ion sputter etching, cross-sectional TEM samples obtained before and after Ar^+ ion beam irradiation for 2 and 4 min were examined. Fig. 5.2 shows cross-sectional HRTEM images of as-deposited and Ar^+ ion irradiated specimens

coated with *a*-C films deposited by PECVD. The *a*-C/NiTa and *a*-C/Au interfaces are indicated by dashed lines. The different material layers through the specimen thickness are labeled in Fig. 5.2(b). The images reveal a layered cross-sectional structure consisting of (1) NiTa layer, (2) *a*-C film, (3) Au capping layer, and (4) epoxy glue [Fig. 5.2(b)]. The average film thickness measured from the TEM images shown in Fig. 5.2 is given in Table 5.1. Sputter etching during Ar^+ ion beam irradiation for 2 and 4 min reduced the average film thickness of PECVD *a*-C films was from 4.6 to 2.8 and 1.1 nm, respectively. Thus, for the present Ar^+ ion irradiation conditions, the average etching rate of the PECVD *a*-C films estimated from HRTEM images is equal to ~0.9 nm/s.

A comparison of the EELS results shown in Fig. 5.3 shows the effect Ar^+ ion beam irradiation on the structure of *a*-C films deposited by PECVD. Because 4-min Ar^+ ion irradiation yielded low carbon intensity, only results for 2-min Ar^+ ion irradiation are included in Fig. 5.3(b). The normalized carbon intensity was obtained by integrating the EELS spectrum from 280 to 305 eV and then dividing it by the maximum carbon intensity, whereas the sp^3 depth profiles were determined from the C K-edge spectra using Eq. (1). The vertical dashed lines indicate the boundaries between different cross-sectional regions. The carbon concentration and sp^3 depth profiles shown in Fig. 5.3 reveal the existence of the five regions: (i) *substrate* (the carbon signal intensity and sp^3 content are almost zero because this region corresponds to the NiTa layer); (ii) *interface layer* (both the carbon concentration and the sp^3 content show a sharp increase), (iii) *bulk film* (the carbon concentration stabilizes at ~100%, while the sp^3 fraction remains fairly constant); (iv) *surface layer* (both the carbon concentration and the sp^3 fraction show a sharp decrease); and (v) *capping layer* (the low carbon intensity is due to adventitious carbon physically adsorbed onto the surface of the Au capping layer). While 2-min Ar^+ ion irradiation barely affected the thickness and sp^3 content of the bulk layer, it significantly reduced the thickness of the interface and surface layers and shifted the carbon peak intensity deeper into the bulk layer.

Table 5.1 gives the thickness of the PECVD *a*-C film and each structural layer and the average sp^3 content of the bulk layer before and after Ar^+ ion irradiation for 2 min. The sum of the layer thicknesses is referred to as the film thickness. The agreement between TEM and EELS measurements of the film thickness is fair. The average etching rate of PECVD *a*-C films predicted from EELS analysis is equal to ~0.9 nm/s, which is in excellent agreement with the HRTEM estimate. While sputter etching did not affect the bulk layer thickness, it reduced the thicknesses of the surface and interface layers from 2.0 to 0.9 nm and 2.0 to 1.4 nm, respectively, resulting in the decrease of film thickness from 5.5 to 3.7 nm. However, despite the significant decrease in film thickness, the effect of Ar^+ ion beam irradiation on the sp^3 content of the PECVD *a*-C films was secondary.

Fig. 5.4 shows cross-sectional HRTEM images of FCVA *a*-C films obtained before and after Ar^+ ion beam irradiation for 2 and 4 min. The dashed lines indicate the interfaces of the *a*-C film with the NiTa layer and evaporated Au capping layer. The images show a NiTa/*a*-C/Au/epoxy layered structure. The average film thickness measured from the TEM images shown in Fig. 5.4 is given in Table 5.1. The results show a decrease in film thickness due to Ar^+ ion beam irradiation for 2 and 4 min from 4.6 to 3.7 and 2.3 nm, respectively, representing an average etching rate of FCVA *a*-C films equal to ~0.5 nm/s.

Fig. 5.5 shows EELS results of FCVA *a*-C films obtained before and after Ar^+ ion beam irradiation for 2 and 4 min. Again, the normalized carbon intensity was obtained by integrating the EELS spectrum from 280 to 305 eV and then dividing by the peak intensity, while the sp^3 depth profiles were calculated from the corresponding C K-edge spectra using Eq. (1). Similar with the PECVD films, the EELS results shown in Fig. 5.5 reveal the existence of a multi-layer film structure consisting of interface layer, bulk film, and surface layer and a secondary effect of Ar^+ ion sputter etching on the sp^3 content of the bulk layer. However, the effect of sputter etching, especially for 4-min Ar^+ ion irradiation, on the film thickness and structure is significant. The trend is for the film thickness to decrease with increasing time of Ar^+ ion irradiation, mainly at the expense of the thickness of surface and interface layers.

As shown in Table 5.1, the agreement between TEM and EELS predictions of the as-deposited film thickness is fair. Ar^+ ion irradiation for 2 and 4 min resulted in the decrease of the average film thickness of FCVA *a*-C films from 5.8 to 4.9 and 3.6 nm, respectively, corresponding to an average etching rate of FCVA *a*-C films equal to ~0.5 nm/s, which is in excellent agreement with the HRTEM result. The lower etching rate of FCVA films compared to PECVD films is attributed to the significantly higher (by ~22 at%) sp^3 content of the corresponding bulk layer (Table 5.1). While sputter etching during 2-min Ar^+ ion irradiation mainly caused thinning of the surface and interface layers, sputter etching during 4-min Ar^+ ion irradiation resulted in significant thinning of all the layers of FCVA *a*-C films. In particular, 2-min Ar^+ ion irradiation resulted in thinning of the surface, bulk, and interface layers by about 18%, 5.6%, and 22%, respectively, whereas for 4-min Ar^+ ion irradiation the corresponding thickness decrease was about 29%, 33%, and ~65%. Thus, it may be inferred that sputter etching during 2-min Ar^+ ion irradiation resulted in the decrease of the film thickness mainly due to the suppression of the surface and interface layers, whereas for sputter etching during 4-min Ar^+ ion irradiation all layers contributed significantly to the decrease of the film thickness. In addition, 4-min Ar^+ ion irradiation resulted in the decrease of the sp^3 content of the bulk layer by ~12 at%.

5.4 Conclusion

The effect of Ar^+ ion beam irradiation on the structure, composition, and thickness of ultrathin *a*-C films deposited onto NiTa-coated glass substrates by PECVD and FCVA was examined by TEM and EELS. The results confirmed the existence of a multi-layer film structure consisting of interface, bulk, and surface layers of thickness in the range of 1–2.5 nm, depending on the deposition method and time of Ar^+ ion irradiation. While sputter etching during 2-min Ar^+ ion irradiation produced insignificant structural/compositional changes (e.g., sp^3 content), it induced significant thinning of the *a*-C films (about 28% and 16% for PECVD and FCVA films, respectively), mainly by reducing the thickness of the surface and interface layers and marginally the thickness of the bulk layer. However, sputter etching during 4-min Ar^+ ion irradiation resulted in significant thinning of all layers comprising the FCVA *a*-C films and a decrease of the sp^3 content by ~9%. The TEM and EELS results of this study demonstrate that *in-situ* Ar^+ ion beam irradiation is an effective post-deposition process for reducing the thickness of *a*-C films, without inducing significant structural changes.

Table 5.1 Film thickness, surface, bulk, and interface layer thickness, and average sp^3 content of bulk layer of *a*-C:H and *a*-C films deposited by PECVD and FCVA, respectively, obtained before (as-deposited) and after Ar^+ ion beam irradiation for 2 and 4 min.

Measurement	Film (deposition method)					
	a-C:H (PECVD)			*a*-C (FCVA)		
	as-deposited	Ar^+ ion irradiated[(a)]		as-deposited	Ar^+ ion irradiated[(a)]	
		2 min	4 min		2 min	4 min
Film thickness[(b)] (nm)	4.6 ± 0.2	2.8 ± 0.4	1.1 ± 0.3	4.6 ± 0.1	3.7 ± 0.3	2.3 ± 0.3
Film thickness[(c)] (nm)	5.5	3.7	–	5.8	4.9	3.6
Surface layer thickness[(c)] (nm)	2.0	0.9	–	1.7	1.4	1.2
Bulk layer thickness[(c)] (nm)	1.5	1.4	–	1.8	1.7	1.2
Interface layer thickness[(c)] (nm)	2.0	1.4	–	2.3	1.8	1.2
Average sp^3 in bulk layer[(c)] (at%)	37.6 ± 0.4	36.6 ± 0.4	–	59.1 ± 1.4	57.5 ± 1.9	51.9 ± 1.4

[(a)]Ion kinetic energy = 500 eV, ion incidence angle = 30°, working pressure = 2×10^{-4} Torr;
[(b)]TEM; [(c)]EELS

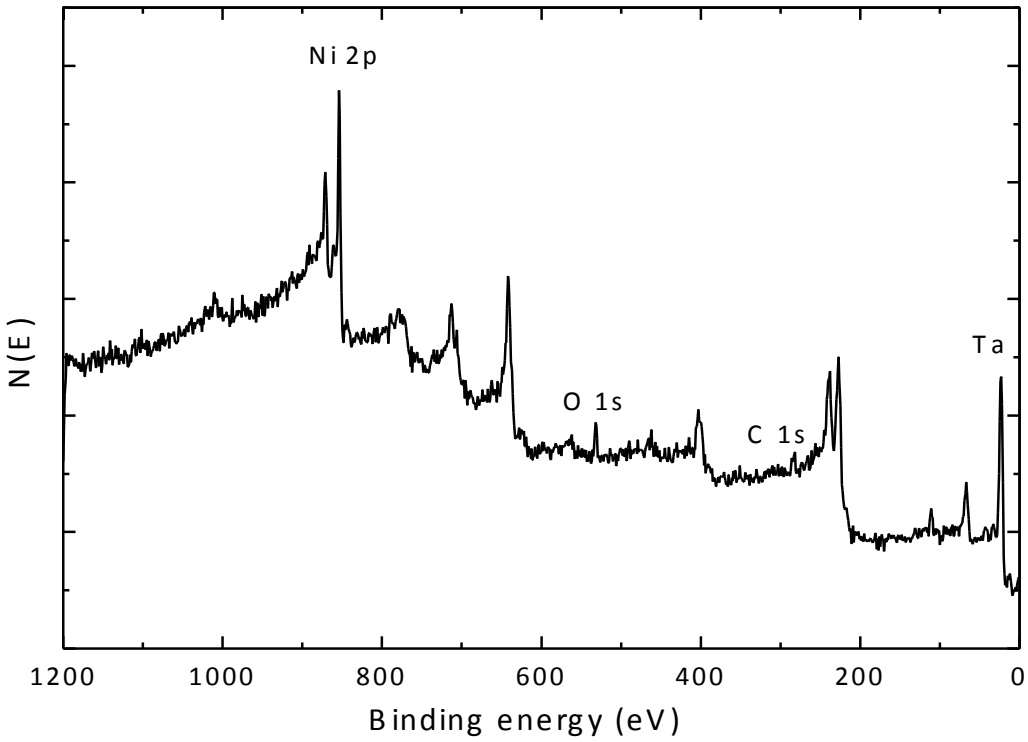

Fig. 5.1 XPS spectrum of obtained after 6 min of 500-eV Ar^+ ion bombardment. The spectrum confirms the complete removal of the PECVD *a*-C:H film from the NiTa/glass substrate.

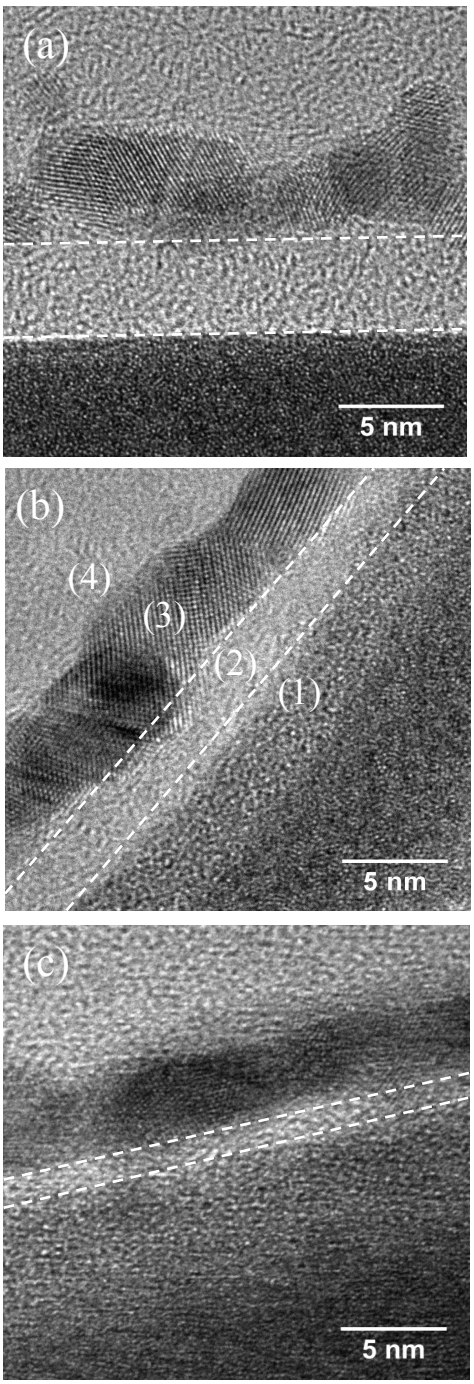

Fig. 5.2 Cross-sectional HRTEM images of *a*-C:H films deposited by PECVD obtained (a) before and after Ar^+ ion beam irradiation for (b) 2 min and (c) 4 min. Contrast and structure differences reveal the following regions: (1) NiTa layer, (2) *a*-C film, (3) Au capping layer, and (4) epoxy mounting material (marked only in (b)).

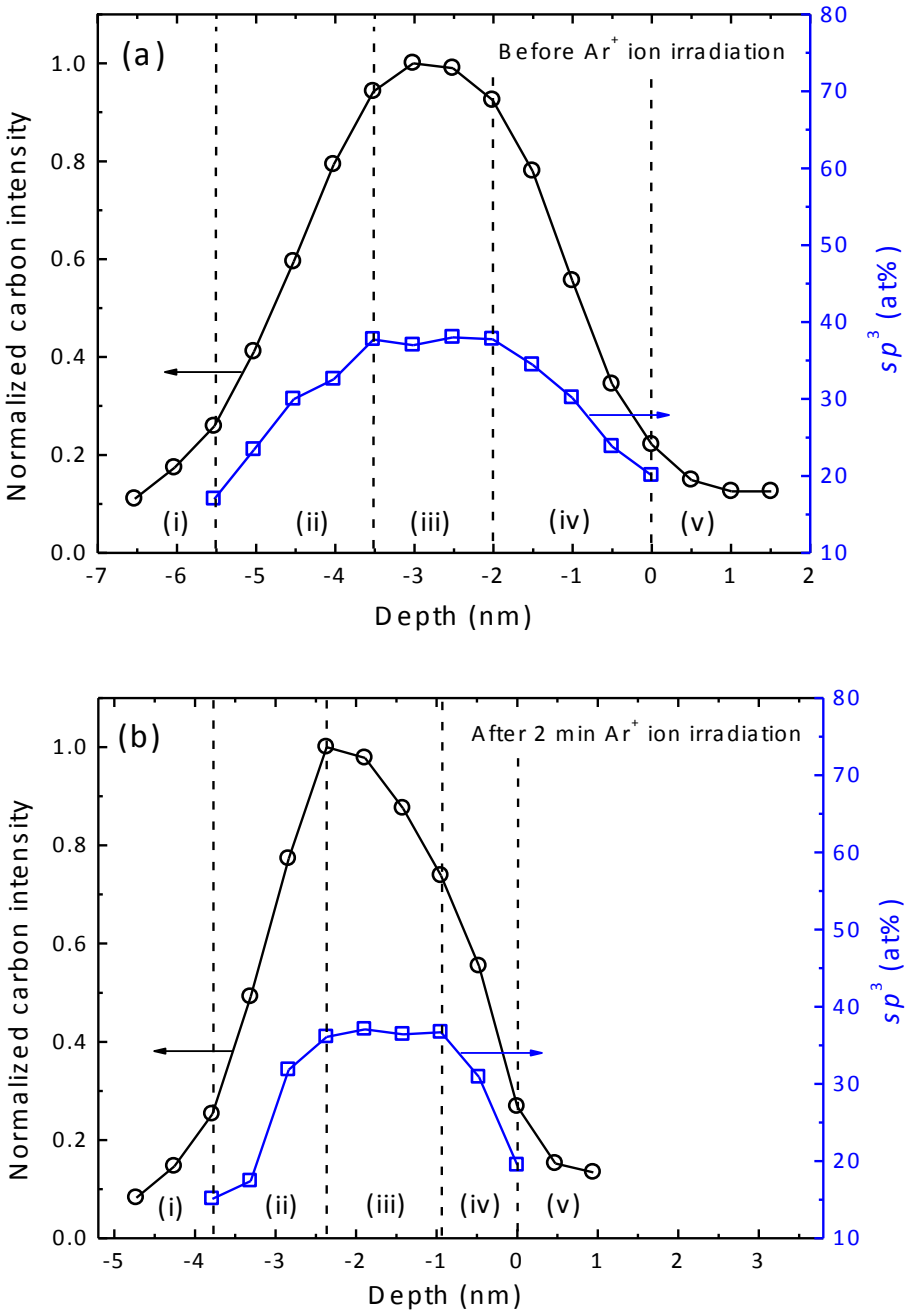

Fig. 5.3 Depth profiles of normalized carbon intensity and sp^3 content calculated from the C K-edge spectra of *a*-C:H films deposited by PECVD. The figure shows variations in the film structure (a) before and (b) after Ar^+ ion beam irradiation for 2 min. The boundaries between different regions are distinguished by dashed lines.

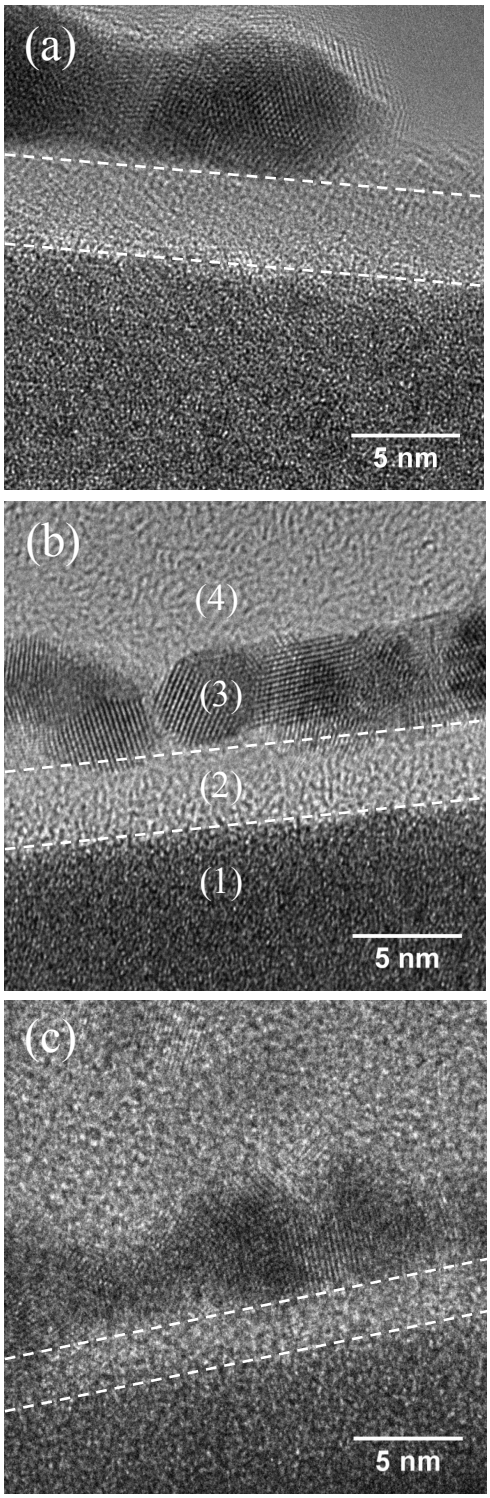

Fig. 5.4 Cross-sectional HRTEM images of *a*-C films deposited by FCVA obtained (a) before and after Ar^+ ion beam irradiation for (b) 2 min and (c) 4 min. Contrast and structure differences reveal the following regions: (1) NiTa layer, (2) *a*-C film, (3) Au capping layer, and (4) epoxy mounting material (marked only in (b)).

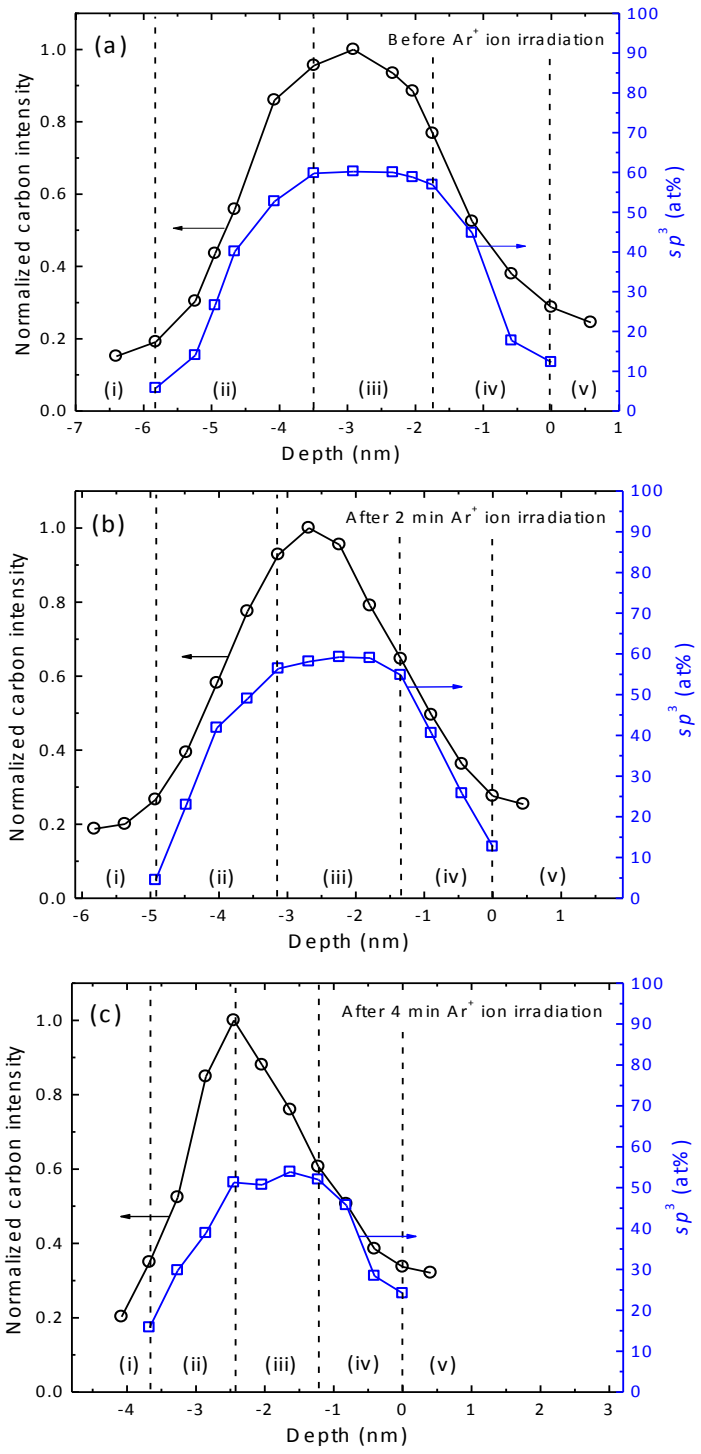

Fig. 5.5 Depth profiles of normalized carbon intensity and sp^3 content calculated from the C K-edge spectra for *a*-C films deposited by FCVA. The figure shows variations in the film structure (a) before and after Ar^+ ion beam irradiation for (b) 2 min and (c) 4 min. The boundaries between different regions are distinguished by dashed lines.

Chapter 6 Bilayer ultrathin amorphous carbon films synthesized by filtered cathodic vacuum arc for magnetic storage technology

6.1 Introduction

The origin of the good tribomechanical properties of *a*-C films is the relatively high content of tetrahedral (sp^3) atomic carbon hybridization, which controls the density, elasticity, and hardness. The sp^3 content shows a strong dependence on the process conditions and deposition method. Energetic film deposition methods, such as filtered cathodic vacuum arc (FCVA) [Anders, 2009], which use ions as film-forming precursors, are particularly effective in producing ultrathin *a*-C films with high sp^3 contents. This is because the C^+ ion kinetic energy can be tuned by biasing the substrate holder with an optimum pulsed voltage to control direct and recoil ion implantation, sputtering of weakly bonded surface atoms (densification), and deposition. However, partial backscattering of the C^+ ions and reduced ion bombardment on the surface of the growing film during the final stage of film deposition yield a multilayered film structure consisting of interface and surface layers of relatively low and varying sp^3 contents and intermediate (bulk) layer rich in sp^3 hybridization [Wang & Komvopoulos, 2013; Siegal et al., 2000; Davis et al., 1995; Davis et al., 1998; Riedo et al., 2000; Lifshitz et al., 1990].

Current trends in magnetic recording necessitate the decrease of the physical spacing between the magnetic media and read/write transducer embedded into the flying head to ~5 nm [Robertson 2003; Goglia et al., 2001]. To achieve such a small physical spacing, the overcoat thickness must be reduced to ~2–3 nm. However, decreasing the film thickness to such extremely low levels raises a concern about its uniformity, density, and overall protective capacity because it will enhance the dominance of the ~1–2-nm-thick interface and surface layers, which are rich in sp^2 hybridization. Indeed, it has been reported that the tribomechanical properties (e.g., elastic modulus and wear rate) and sp^3 content show a dependence on film thickness when the films are <4 nm thick [Ferrari, 2004; Casiraghi et al., 2004(A); Casiraghi et al., 2004(B); Beghi et al., 2002; Zhong et al., 2009]. Moreover, the important effect of sp^3 content on the thermal stability of *a*-C films used in heat-assisted magnetic recording (HAMR) has been elucidated by molecular dynamic simulation results [Marchon et al., 2004]. Thus, it is necessary to develop a film deposition method, which can produce ultrathin *a*-C films with structures and properties predominantly controlled by the sp^3-rich bulk layer and interface and surface layers of minimal thickness.

Previous studies dealing with the adhesion of *a*-C films to different substrate materials examined relatively thick films. The increase of the substrate bias voltage promotes intermixing of carbon with the substrate atoms, which is conducive to the development of a strong film/substrate interface [Sheeja et al., 2001; Davis et al., 1998; Chhowalla & Amaratunga, 2001; Rismani et al., 2012]. However, this will also increase the thickness of the interface layer, which may negatively impact he magnetics of the media [Anders, 2009; Ferrari, 2004] and degrade the quality of the ultrathin film as a result of the intense C^+ ion bombardment [Ferrari, 2004; Han et al., 1999].

The main objective of this study is to introduce a multi-step FCVA deposition process which can overcome the aforementioned problems. The main concept is to synthesize bilayer ultrathin *a*-C films with structure and properties dominated by the sp^3-rich bulk layer. An initial low ion energy deposition step (no substrate biasing) and a final process step of Ar^+ ion sputter etching are used before and after *a*-C film deposition under optimum FCVA conditions of substrate biasing, respectively. The initial deposition step leads to the formation of an extremely thin buffer layer that acts as a buffer layer in the subsequent process step of bulk layer deposition under energetic C^+ ion bombardment (substrate biasing). Therefore, another principal objective is to examine the through-thickness structure and composition of bilayer ultrathin (~2–3 nm) *a*-C films deposited by this method using high-resolution transmission electron microscopy (HRTEM) and electron energy loss spectroscopy (EELS). To illustrate the capability of the present multi-step FCVA process to synthesize ultrathin *a*-C films mainly consisting of sp^3-rich bulk layer, representative HRTEM and EELS results of bilayer *a*-C films are contrasted with those of single-layer *a*-C films deposited under the same FCVA conditions as the bulk layer of the bilayer films.

6.2 Experimental procedure

6.2.1 Film deposition

Substrates (1×1 cm^2) cut from a 2.5-in.-diameter disk coated with a ~100-nm-thick NiTa layer were loaded onto a custom-made FCVA system [Zhang & Komvopoulos, 2008; Zhang & Komvopoulos, 2009] and etched for 6 min in vacuum (~2×10^{-4} Torr) with a 500-eV Ar^+ ion beam of 60^o incidence angle (measured from the normal to the substrate surface) generated by a 64-mm Kaufman ion source (Commonwealth Scientific, Alexandria, VA). Details on the FCVA deposition system are described in the Chapter 4.

To control the C^+ ion energy during the first deposition step and minimize the thickness of the buffer layer, the substrate stage was oriented at an angle of 20° with respect to incoming C^+ ions without applying a bias voltage. To produce a buffer layer of thickness <1 nm, the deposition time was fixed at 6 s. During the second step of deposition, which also lasted for 6 s, an optimal pulsed bias voltage of –100 V and 75% duty cycle was applied to the substrate stage which was placed perpendicular to the incoming C^+ ions to favor ion subplantation into the buffer layer and promote sp^3 hybridization in the bulk layer accordingly to the results in Chapter 4. In the third deposition step, 500-eV Ar^+ ion sputter etching was performed for 6 min to reduce the film thickness to 2–3 nm, as demonstrated in the previous Chapter. The process conditions of each deposition step are summarized in Table 6.1. For comparison, a single-layer *a*-C film was deposited in 12 s under optimal FCVA conditions (i.e., substrate bias voltage = –100 V, duty cycle = 75%, ion incidence angle = 90^o) and etched to a similar thickness as the bilayer films by a 4-min Ar^+ ion sputter etching.

6.2.2 Microanalysis methods

Cross-sections of films deposited by FCVA were examined with the high-resolution TEM (Tecnai) to measure the film thickness. Details about the TEM sample preparation and the TEM system can be found in chapter 2. The details about the curve fitting method and calculation of the sp^3 fraction from EELS are given in Chapter 4.

6.3 Results and discussion

Cross-sectional HRTEM specimens were used to determine the *a*-C film thickness after each process step. Fig. 6.1 shows cross-sectional HRTEM images of *a*-C films obtained after each step. (The different layers within the cross-sectional structure are labeled in Fig. 6.1). All images reveal a multi-layer structure consisting of (1) NiTa layer, (2) *a*-C film, (3) Au capping layer, and (4) epoxy glue. The average film thickness corresponding to the first, second, and third process step is equal to 0.96, 5.89, and 2.50 nm, respectively (Table 6.1).

Fig. 6.2 shows the cross-sectional structure of *a*-C films after each process step. The normalized carbon intensity is obtained by integrating the EELS spectrum from 280 to 305 eV and then dividing the result with the peak intensity obtained across the depth profile. The sp^3 fraction is calculated from C K-edge spectra using Eq. (1). The carbon concentration and sp^3 fraction depth profiles reveal the existence of five distinct layers with the following characteristics: (i) *substrate* (the carbon signal intensity is almost zero because the signal corresponds to the NiTa layer); (ii) *interface (buffer) layer* (the carbon concentration and sp^3 content increases sharply); (iii) *bulk layer* (the carbon concentration stabilizes at ~100% while the sp^3 fraction remains almost constant); (iv) *surface layer* (both the carbon concentration and the sp^3 fraction decrease sharply); and (v) *capping layer* (the weak carbon signal intensity is attributed to physisorption of adventitious carbon to the surface of the Au layer surface). The dashed lines shown in Fig. 6.2 denote the boundaries of neighboring layers. A comparison of the results shown in Fig. 6.2 indicates that the bilayer film structure exhibits a sharp increase in sp^3 content in the buffer (interface) layer and that Ar^+ ion sputter etching effectively reduced the thickness of the surface layer, consistent with previous findings in Chapter 5.

Fig. 6.3 shows a comparison of cross-sectional HRTEM images for a single-layer and bilayer *a*-C films of similar thickness. The corresponding depth profiles of the normalized carbon intensity and sp^3 content, obtained from cross-sectional scanning of the EELS spectra, are contrasted in Fig. 6.4. It can be seen that the thickness of interface layer is significantly reduced and the change (slope) of the sp^3 content in the interface layer is much larger in the bilayer *a*-C film.

The thickness of the interface (buffer), bulk, and surface layers and the average sp^3 content of the bulk layer of single-layer and bilayer *a*-C films are given in Table 6.2. The sum of the thicknesses of all layers is termed total thickness. The HRTEM and EELS results of the total thickness are in good agreement. The difference of the total thickness measured from the HRTEM and EELS results indicates some intermixing of carbon with the NiTa layer, which is not captured in the HRTEM images. Therefore, the carbon signal detected by EELS provides a more accurate measurement of the total thickness. Table 6.2 shows that the surface and total

thickness of the single-layer and bilayer *a*-C films are similar; however, the interface layer in the bilayer films has a much smaller thickness. The similar thickness of the surface layer is expected because both single-lay and bilayer *a*-C films were subjected to the same Ar^+ ion sputter etching post-deposition treatment. Thus, the interface layer thickness decreases from 31.6% (single-layer film) to 13.1% (bilayer film) of the total film thickness, while the bulk layer thickness increases from 36.8% (single-layer film) to 55.3% (bilayer film) of the total film thickness. In addition, the slope of the sp^3 depth profile in the interface layer changes from 31.4%/nm (single-lay film) to 60%/nm (bilayer film) and the sp^3 content of the bulk layer increases from 51.9% (single-layer film) to 53% (bilayer film). These results demonstrate the high potential of bilayer *a*-C film deposition by FCVA.

6.4 Conclusion

The thickness, structure, and composition of single- and bilayer *a*-C films synthesized by FCVA were characterized by cross-sectional HRTEM and EELS. Depositing first an ultrathin (~1 nm) buffer layer under zero substrate bias voltage, the thickness of the interface (intermixing) layer was reduced by 58%, which is critical to preserving the properties of magnetic media. In addition, the sp^3 fraction in the bulk layer of the bilayer *a*-C films was slightly increased. The obtained HRTEM and EELS results indicate that the bilayer film deposition technique developed in this study can effectively reduce the overcoat thickness in magnetic recording, while preserving the overcoat quality and enhancing cross-sectional film uniformity.

Table 6.1 Deposition conditions of bilayer *a*-C films.

Process step	Process conditions				Characteristics	Film thickness (nm)
	Duty cycle (%)	Substrate bias voltage (V)	Ar^+ ion incidence angle (^{o})	Time (s)		
1	-	0	20	6	thin buffer layer	0.96
2	75	-100	90	6	high sp^3 bulk layer	5.89
3	Ar^+ ion etch: 500 eV, 6 min, 30°, 2×10^{-4} Torr				etched to ~ 2nm	2.50

Table 6.2 Total thickness, surface, bulk, and interface (buffer) layer thickness, and average sp^3 content of bulk layer of single-layer and bilayer *a*-C films synthesized by FCVA.

Properties	Bi-layer	Single-layer
Total thickness from TEM (nm)	2.5	2.3
Total thickness from EELS (nm)	3.7	3.7
Surface layer thickness from EELS (nm)	1.2	1.2
Bulk layer thickness from EELS (nm)	2.1	1.2
Bulk layer-to-total thickness percentage ratio (%)	56.8	32.4
Interface layer thickness from EELS (nm)	0.4	1.3
Interface layer-to-total thickness percentage ratio (%)	10.8	35.1
Change in slope of sp^3 profile in the interface layer (%/nm)	60.0	31.4
Average bulk sp^3 fraction (%)	53.0±3.6	51.9±1.4

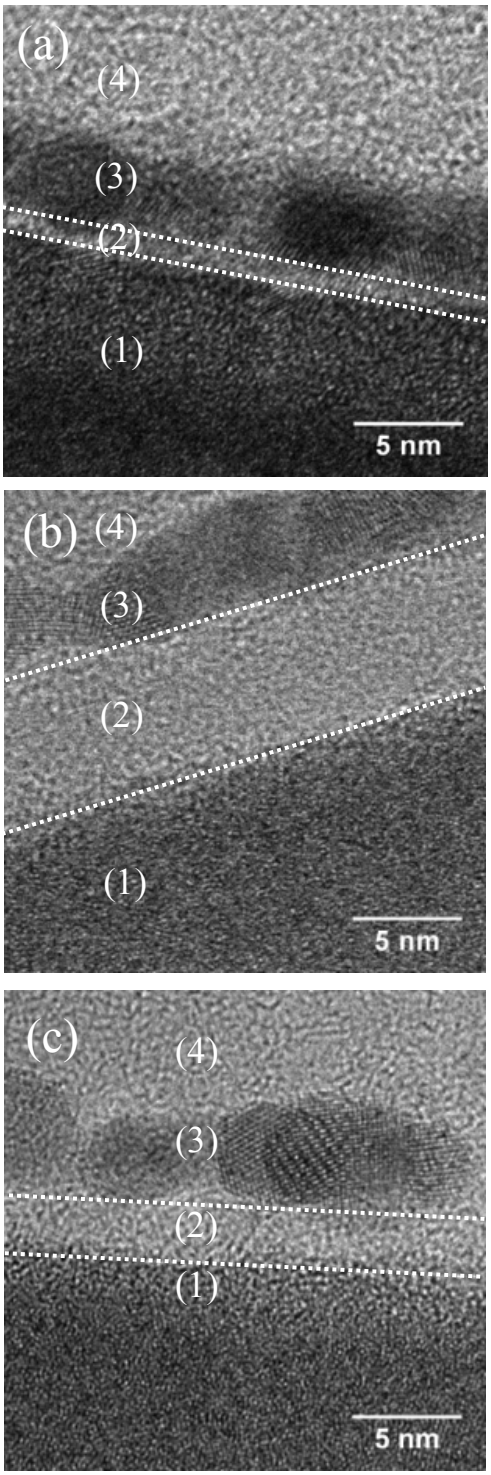

Fig. 6.1 Cross-sectional HRTEM images of *a*-C films deposited by FCVA after the deposition of (a) a buffer (interface) layer and (b) a bulk layer and (c) after 6-min of Ar^+ ion etching post-deposition treatment. Contrast and structure differences reveal (1) NiTa layer, (2) *a*-C film, (3) Au capping layer, and (4) epoxy mounting material.

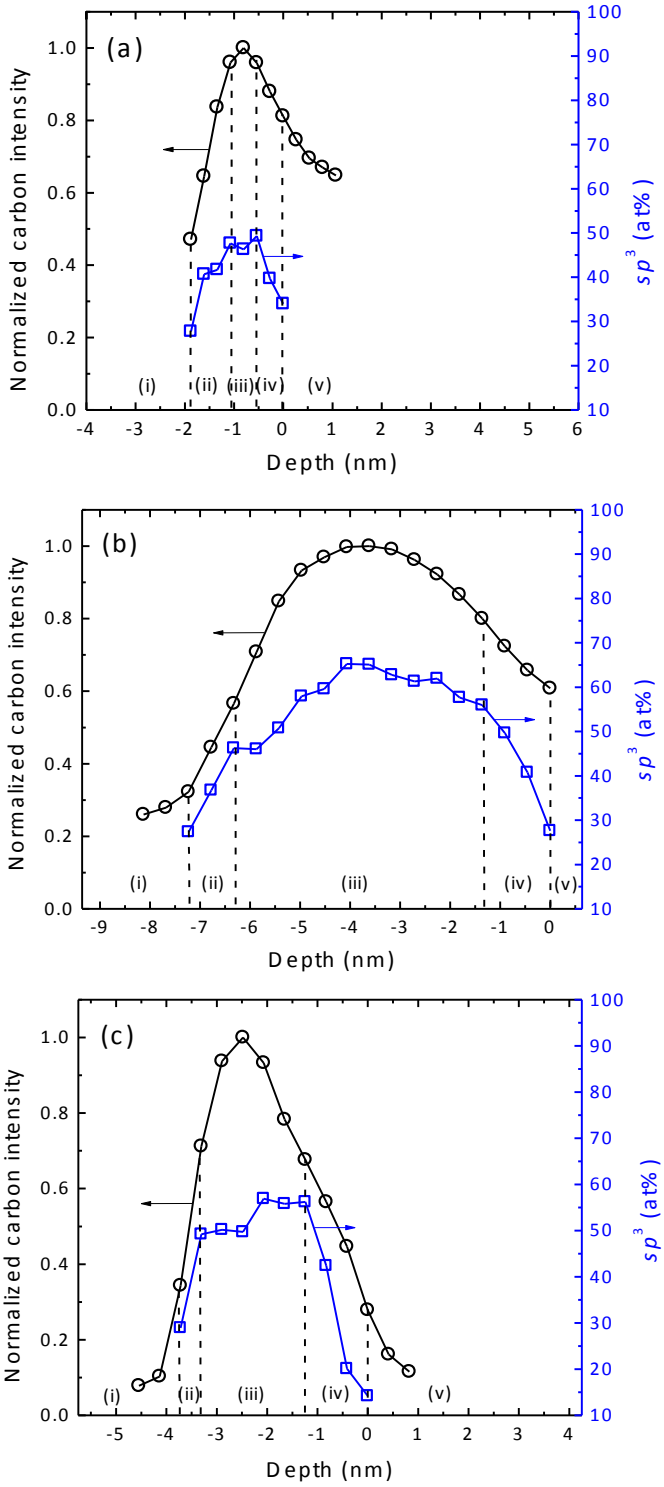

Fig. 6.2 Depth profiles of normalized carbon intensity of C-K edge and sp^3 content calculated from the C K-edge spectra of *a*-C films deposited by FCVA after deposition of a buffer (interface) layer and a bulk layer, and after 6-min of Ar^+ ion etching post-deposition treatment. The dashed lines indicate the boundaries between neighboring regions.

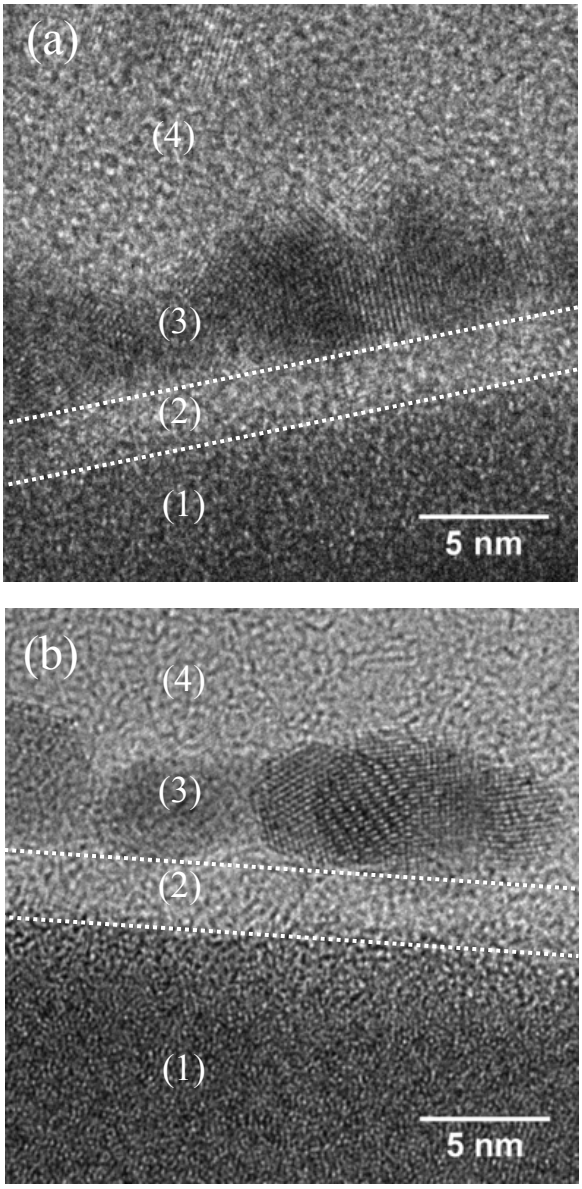

Fig. 6.3 Cross-sectional HRTEM images of (a) single-layer and (b) bilayer *a*-C films deposited by FCVA obtained after 6-min of Ar^+ ion etching post-deposition treatment.

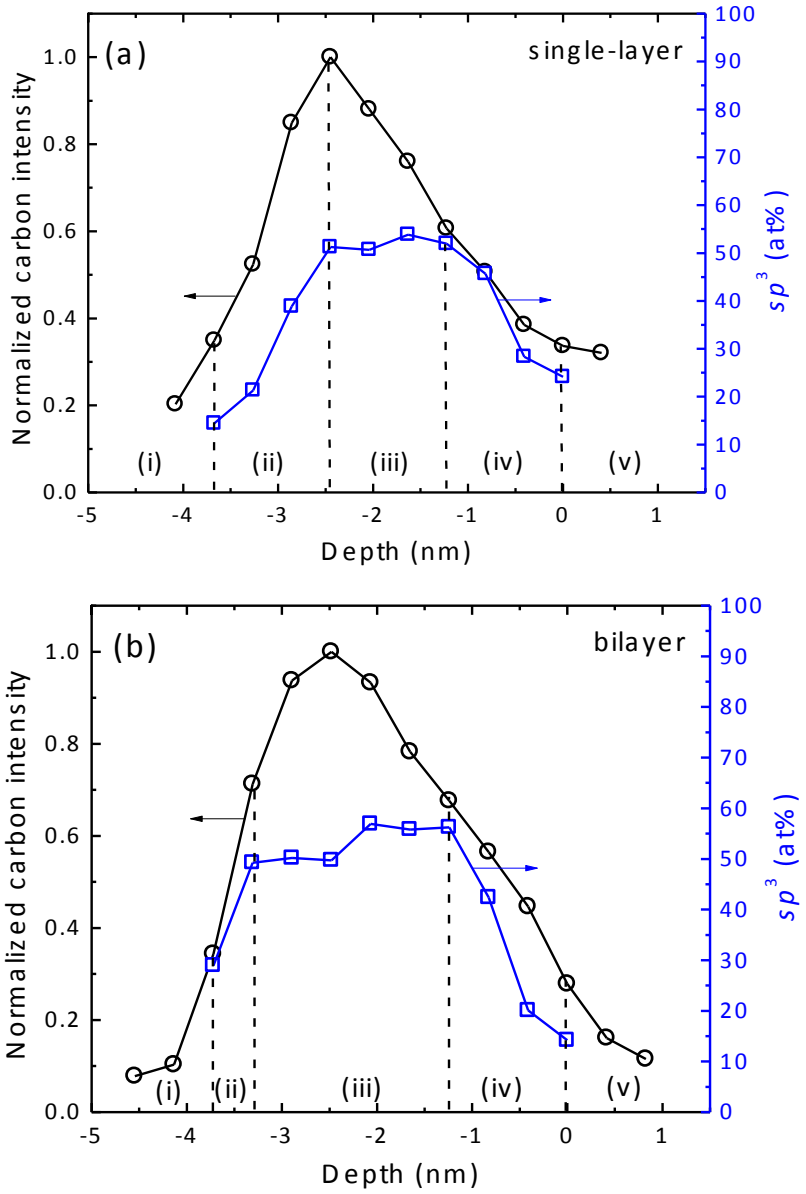

Fig. 6.4 Depth profiles of normalized carbon intensity of C-K edge and sp^3 content calculated from the C K-edge spectra of *a*-C films deposited by FCVA. The depth profiles reveal significant differences between single-layer and bilayer *a*-C films after 6-min of Ar^+ ion etching post-deposition treatment. The dashed lines indicate the boundaries between neighboring regions.

Chapter 7 Structural stability of ultrathin amorphous carbon films subjected to rapid thermal annealing

7.1 Introduction

The demands for ultrahigh storage densities [Wood, 2009; Bandic & Victora, 2008; Yuan et al., 2009] have motivated the evolution of new information storage technologies that are not restricted by the superparamagnetic limit, such as heat-assisted magnetic recording, [Kryder et al., 2008; Stipe, 2010] which uses a laser-optical system integrated into the magnetic head to locally heat a fine-grained magnetic medium of high magnetic anisotropy energy density above its Curie temperature in order to instantaneously decrease its coercivity and enable information to be stored in the form of single bits by the transducer of the magnetic head. However, the rapid and repetitive temperature excursions encountered with this technology may degrade the structure of the ultrathin *a*-C film by destabilizing atomic carbon bonding. [Grierson et al., 2010; Kalish et al., 1999]

The structure of *a*-C films can be characterized by the dominance of trigonal (sp^2) and tetrahedral (sp^3) carbon atom bonding, which strongly depends on the deposition process. Plasma-enhanced chemical vapor deposition (PECVD) [Robertson, 2001; Choy, 2003] and filtered cathodic vacuum arc (FCVA) [Petereit et al., 2003; Anders, 2009; Xu et al., 1996] are considered to be the most effective deposition methods for synthesizing continuous ultrathin (≤5 nm thick) *a*-C films with good mechanical properties, although thin carbon films have also been deposited by other less common methods such as pulsed laser deposition [Kovarik at al., 1993]. However, because the surface and intermixing layers of FCVA *a*-C films exhibit a lower sp^3 content than the bulk layer, [Wang & Komvopoulos, 2013; Siegal et al., 2000; Davis et al., 1995; Davis et al., 1998; Riedo et al., 2000; Lifshitz et al., 1990] the overall structure, composition, and nanomechanical properties of ultrathin FCVA *a*-C films might be inferior compared with those of relatively thick *a*-C films because their structure is dominated by those of the surface and intermixing layers which possess low sp^3 contents. As a result, variations in the cross-sectional uniformity of ultrathin *a*-C films may negatively impact their mechanical behavior. [Ferrari, 2004; Casiraghi et al., 2004(A); Casiraghi et al., 2004(B); Beghi et al., 2002]

In previous studies focused on the structural stability of ultrathin *a*-C films, X-ray photoelectron spectroscopy (XPS), X-ray reflectivity (XRR), and visible resonant Raman spectroscopy were used to discern structural differences between as-deposited and thermally treated (annealed) *a*-C films. For example, a Raman spectroscopy study [Kundu et al., 2014] dealing with the structural stability of 1.5-nm-thick diamondlike carbon (DLC) films revealed that rapid heating in air for 2 s (~10^6 °C/s heating rate; ~500 μs dwell time; >427 °C peak temperature) produced insignificant changes in the structure of FCVA DLC films, but significant carbon loss due to oxidation for sputtered DLC films. In another study, [Jones et al., 2014] rapid laser heating (10^6 °C/s heating rate; ~500 μs dwell time; 450 °C media temperature) of 5-nm-thick PECVD carbon films yielded an increase in sp^2 hybridization and a decrease in film thickness. Multi-wavelength

Raman, XRR, and XPS investigations [Rose et al., 2014] have shown that rapid heating to 659 °C for 1 s of hydrogenated DLC films synthesized by PECVD, sputtering, and FCVA causes a decrease in sp^3 fraction and small changes in film density and hydrogen content. Structure changes in *a*-C:H films synthesized by PECVD caused by slow (10 ° C/min) heating from 150 to 500 °C and cooling below 40 °C were studied *in situ* by XPS [Mangolini et al., 2013] to elucidate the energetics of sp^2 phase clustering and sp^3 rehybridization to sp^2. In another study, [Wang et al., 2013] rapid thermal annealing (RTA) at 660 °C for 1 s did not cause film graphitization or oxidation of 9.5-nm-thick PECVD *a*-C:H films; however, RTA above ~400–450 °C produced significant structural changes in thinner (3.4 nm) *a*-C:H films, indicative of hydrogen depletion, sp^2 cluster enlargement, and increased carbon network ordering. Despite important insight into the effect of heating on the quality of ultrathin carbon films obtained from these studies, the used characterization methods are subjected to film thickness and signal intensity limitations. In particular, XPS cannot provide detailed information about the structure of each layer existing in ultrathin FCVA *a*-C films, XRR fails to accurately measure the density of ultrathin films possessing a multilayered structure, [Ferrari et al., 2000; Mate et al., 2000] and Raman analysis uses an extrapolation method to indirectly estimate the sp^3 fraction. To detect changes in the cross-sectional film structure, it is necessary to directly measure the sp^3 content with nanometer resolution. Cross-sectional electron energy loss spectroscopy (EELS) is a suitable method for studying the through-thickness structure of ultrathin films because it provides high spatial and energy resolution.

A review of the literature, including the studies mentioned above, indicates that information about structural changes (e.g., sp^3 content) of the interface (intermixing), bulk, and surface layers of *a*-C films subjected to rapid heating is sparse. Therefore, knowledge of the structural stability of ultrathin *a*-C films subjected to rapid thermal annealing (RTA), as revealed by cross-sectional structural and compositional changes, is of particular importance. The objective of this study is to elucidate and compare the structural stability of ultrathin *a*-C:H or *a*-C films deposited by two competing methods, i.e., PECVD and FCVA. Changes in carbon concentration, atomic carbon hybridization, and thickness of *a*-C films subjected to RTA were studied by high-resolution transmission electron microscopy (HRTEM) and cross-sectional EELS. HRTEM and EELS results are contrasted to quantify differences in the structural stability of PECVD and FCVA ultrathin *a*-C:H or *a*-C films.

7.2 Experimental procedure

7.2.1 Film deposition

Substrates (1 × 1 cm^2) cut from the 2.5-in.-diameter glass disks coated with a ~100-nm-thick NiTa alloy were coated with ~5-nm-thick *a*-C:H films deposited by PECVD or FCVA. In all the PECVD depositions, the film precursor was acetylene (C_2H_2) and the acceleration bias of ions was set at 120 V. The density (determined from XRR measurements) and hydrogen content of the PECVD *a*-C:H films (measured by the manufacturer) are equal to ~2.0–2.1 g/cm^3 and 30–40%, respectively. To deposit *a*-C films on similar substrates by the FCVA technique, *a*-C:H/NiTa/glass substrates were loaded onto the substrate stage of a custom-made FCVA system [Zhang & Komvopoulos, 2008; Zhang & Komvopoulos, 2009] and the *a*-C:H overcoat was

sputtered off by bombarding with 500-eV Ar^+ ions generated by a 64-mm Kaufman ion source (Commonwealth Scientific, Alexandria, VA) under a working pressure of ~2×10^{-4} Torr and a 60° Ar^+ ion incidence angle measured from the normal to the substrate surface. XPS analysis confirmed that, under these conditions, the *a*-C:H film was fully removed after 6 min of Ar^+ ion sputtering (Fig. 5.1). To control the C^+ ion energy during film deposition, an optimum pulsed bias voltage of –100 V magnitude and 25 kHz frequency was applied to the substrate. To deposit ultrathin FCVA films of thickness similar to that of the PECVD films, the deposition time was fixed at 12 s. All other details on the deposition process are given in Chapter 5.

7.2.2 Rapid thermal annealing (RTA)

RTA experiments were performed in a heating chamber integrated with a computer control system (RTP-600xp, Modular Process Technology). The specimen was heated by tungsten-halogen lamps and the temperature rise was measured with a thermocouple placed in contact with the backside of the specimen holder. The heating rate during RTA was equal to 105 ± 8.5 °C/s. During RTA, the equipment was purged with a gas mixture of 8000 sccm N_2 and 2000 sccm O_2. The maximum temperature and time during RTA were equal to 650 °C and 1 s, respectively. Further details on the RTA equipment are given elsewhere. [Wang et al., 2013]

7.2.3 Microanalysis methods

Cross-sections of films deposited by PECVD and FCVA were examined with the high-resolution TEM (Tecnai) to measure the film thickness. Details about the TEM sample preparation and the TEM system can be found in chapter 2. The details about the curve fitting method and calculation of the sp^3 fraction from EELS are given in Chapter 4.

7.3 Results and discussion

Fig. 7.1 shows cross-sectional HRTEM images of PECVD *a*-C:H and FCVA *a*-C films obtained before and after RTA. (The different layers in each image are labeled in Fig. 7.1(b)). All images show four distinct regions: (1) NiTa alloy layer, (2) *a*-C:H or *a*-C film, (3) Au capping layer, and (4) epoxy glue. A comparison of the HRTEM images shown in Fig. 7.1 does not show any apparent changes in film thickness or sp^2 clustering due to RTA in either type of film. Thus, it may be interpreted that film oxidation and dissociation did not occur under the present RTA conditions. However, Table 7.1 shows a notable change in the average thickness of the PECVD films. While the average thickness of the FCVA *a*-C films was not affected by RTA, the mean thickness of the PECVD *a*-C:H films increased from 4.61 to 5.45 nm.

Fig. 7.2 shows the effect of RTA on the structure of the PECVD *a*-C:H and FCVA *a*-C films. The normalized intensity was obtained by integrating the EELS spectrum in the range of 280–305 eV, whereas the depth profiles of the sp^3 fraction were calculated from the C K-edge spectra using Eq. 4.2. It can be seen that RTA decreased the sp^3 fraction of the PECVD *a*-C:H films and the carbon intensity shifted to the inner layer, presumable due to hydrogen depletion, as shown by Raman spectroscopy. [Wang et al., 2013] The sp^3 fraction and carbon concentration reveal the

existence of the five distinct regions: (1) *substrate* (the carbon signal intensity is almost zero because it originates from the NiTa alloy); (2) *intermixing layer* (both the carbon concentration and sp^3 content increase rapidly); (3) *bulk film* (the carbon concentration stabilizes at ~100%, whereas the sp^3 fraction remains fairly constant); (4) *surface layer* (both the carbon concentration and the sp^3 fraction decrease sharply); (5) *capping layer* (the low intensity of the carbon signal is attributed to carbon from the ambient adsorbed onto the surface of the Au capping layer).

Table 7.1 gives the thickness of the intermixing, bulk, and surface layers and the average sp^3 fraction of the bulk layer of the *a*-C films before and after RTA. The sum of the thicknesses of all the layers comprising the *a*-C films is referred to as the total thickness. The agreement between TEM and EELS results of the total film thickness is fairly good. The thickness of the surface and bulk layers of PECVD *a*-C:H films are similar before and after RTA, while the intermixing layer thickness increased from 2.5 nm to 3.6 nm, presumably a result of carbon diffusion. The bulk layer of the FCVA *a*-C films exhibits a higher sp^3 fraction relatively to the PECVD *a*-C:H films. Moreover, RTA caused the sp^3 fraction of the bulk layer of PECVD films to decrease by 4.5%, indicating the occurrence of carbon graphitization and/or $sp^3 \rightarrow sp^2$ rehybridization. In contrast, RTA did not affect the thickness, carbon intensity, or sp^3 content of the FCVA *a*-C films.

7.4 Conclusion

Summarizing, the effect of RTA on the structure, composition, and thickness of PECVD *a*-C:H and FCVA *a*-C films was examined by HRTEM and EELS. It was shown that RTA at 650 °C for 1 s increases the thickness of the intermixing layer by ~1.1 nm and reduces the sp^3 fraction of the bulk layer of PECVD films by 4.5%. Under the same RTA conditions, the FCVA *a*-C films exhibited insignificant changes in both thickness and sp^3 content, revealing a superior structural stability over PECVD films.

Table 7.1 Comparison of total thickness, layer thickness, and sp^3 content of bulk layer of *a*-C:H films deposited by PECVD and *a*-C films deposited by FCVA obtained before and after rapid thermal annealing at 650 °C for 1 s.

Deposition method	Rapid thermal annealing	Thickness (nm)					sp^3 (%) bulk layer
		total (TEM)	total (EELS)	intermixing layer	bulk layer	surface layer	
PECVD	before	4.56 ± 0.24	5.5	2.5	1.5	1.5	37.63 ± 0.44
	after	5.47 ± 0.50	6.5	3.6	1.5	1.4	33.10 ± 1.24
FCVA	before	4.61 ± 0.13	5.8	1.7	2.1	2.0	59.14 ± 1.36
	after	4.63 ± 0.26	6.1	2.0	2.4	1.7	58.07 ± 1.44

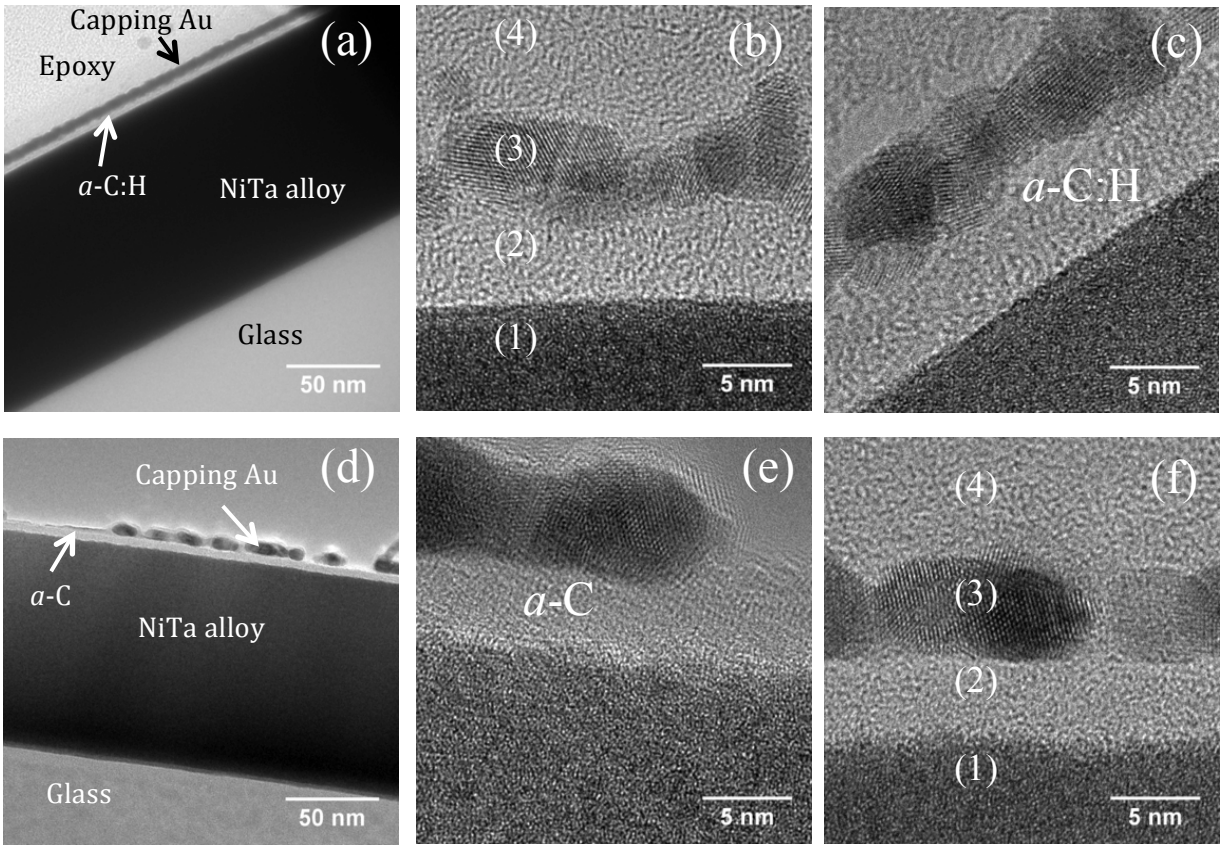

Fig. 7.1 Cross-sectional HRTEM images of *a*-C:H or *a*-C films deposited by (a–c) PECVD and (d–f) FCVA, respectively. Overview images of *a*-C films deposited on NiTa/glass substrates (a, d) and close-up views of *a*-C films obtained (b, e) before and (c, f) after RTA. Contrast and structural differences reveal four distinct regions: (1) NiTa alloy layer, (2) *a*-C:H or *a*-C film, (3) Au capping layer, and (4) epoxy glue.

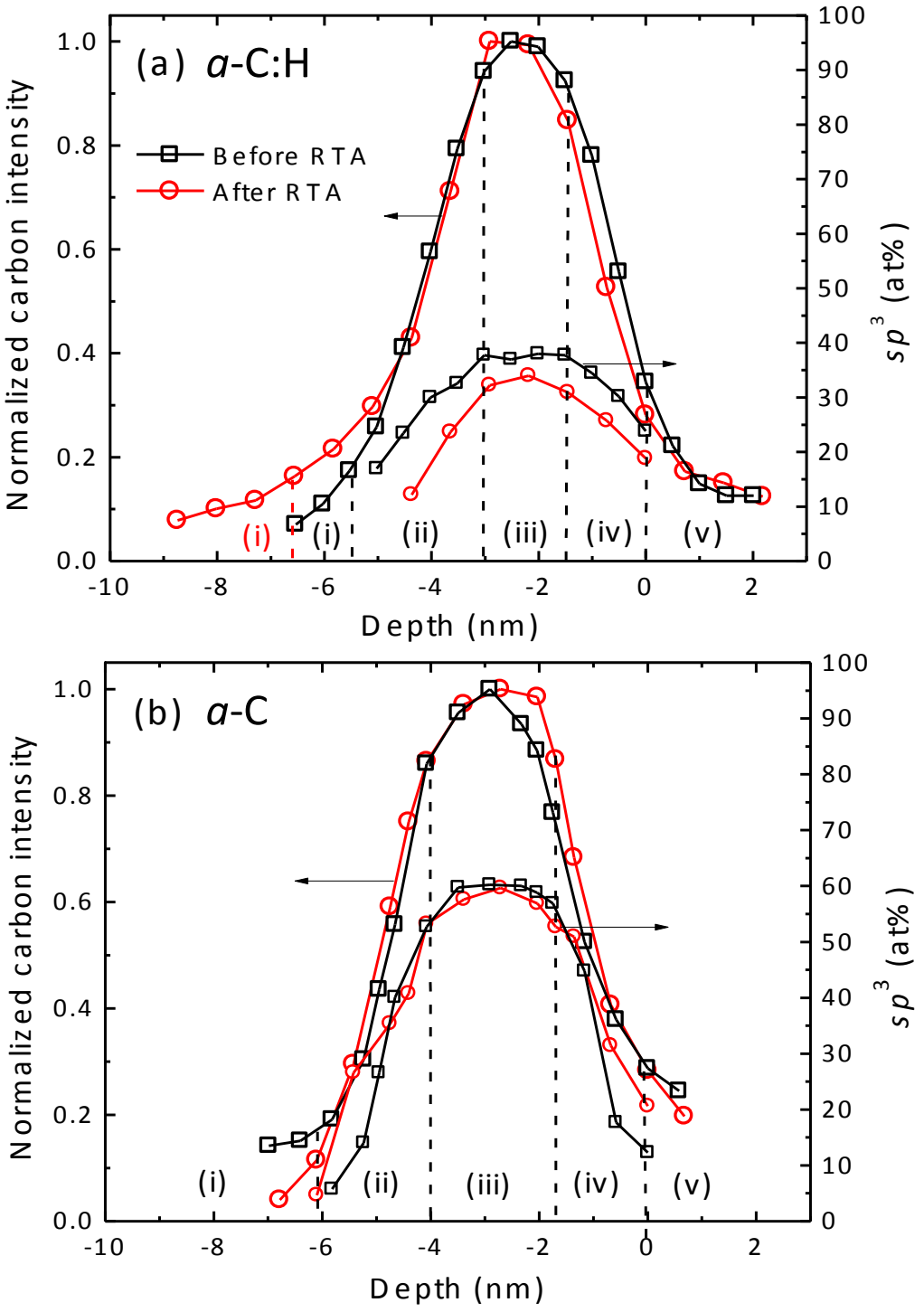

Fig. 7.2 Cross-sectional depth profiles of normalized intensity of C-K edge and sp^3 fraction calculated from the C K-edge spectra of *a*-C:H or *a*-C films deposited by (a) PECVD and (b) FCVA showing differences before and after RTA. The dashed lines indicate the boundaries between adjacent regions.

Chapter 8 Friction, nanostructure, and residual stress of single-layer and multi-layer amorphous carbon films deposited by radio-frequency sputtering

8.1 Introduction

Among various film deposition techniques to synthesize the *a*-C films, [Ishikawa et al., 1987; McKenzie et al., 1991; Kovarik et al., 1993; Lu & Komvopoulos, 1999] radio-frequency (rf) sputtering is a widely used film deposition method because the film precursors (i.e., atoms and/or clusters of atoms) require low input energy compared to deposition methods using energetic ions as film-forming precursors. Moreover, inert ion bombardment of the film surface during sputtering enables the film properties to be tailored without changing the film chemical environment. Energetic Ar^+ ion bombardment of the growing film is commonly used in sputtering to enhance the film density and hardness; [Lu & Komvopoulos, 1999; Lifshitz et al., 1994; Schwan et al., 1997] however, ion bombardment usually produces films possessing high residual stress and different microstructures, depending on the competing kinetic processes encountered under nonequilibrium film-growth conditions. [Lu & Komvopoulos, 1999; Schwan et al., 1996; Ohring, 1992; Lu & Komvopoulos, 2000] Previous studies have shown that ion bombardment may produce compressive residual stresses up to about −16 GPa, [Schwan et al., 1996; Lu & Komvopoulos, 2000; Lu et al., 2001] which may result in film delamination, buckling, agglomeration (clustering), and other adhesion failures when the film is grown to a critical thickness. [Ohring, 1992; Lu et al., 2001; Srolovitz & Goldiner, 1995] Therefore, preventing the development of high residual (intrinsic) stresses in films deposited under sputtering conditions of energetic ion bombardment is critical to the applications, such as cutting tools or biomedical overcoat that maximum film thickness is desired.

Because the film roughness and friction characteristics affect the tribological performance of contacting surfaces, methods of depositing relatively smooth and hard films are of particular importance. Several methods have been used to prevent the development of undesirable high residual stresses in carbon films, such as post-process treatment like thermal annealing, [Friedmann et al., 1997; Ferrari et al., 1999; Kalish et al., 1999; Sullivan et al., 1997] addition of various elements (e.g., Si, Al, W, and Ti) to modify the film structure, [Chhowalla et al., 1996; Dai & Wang, 2011; Lee et al., 2002; Wang et al., 2006; Shi & Meng, 2003; Zhang et al., 2002] and deposition of multi-layer films consisting of alternating hard/soft *a*-C layers. [Logothetidis et al., 2000; Lu et al., 2003]

The structure and properties of sputtered *a*-C films greatly depend on deposition conditions. For example, ultrathin *a*-C films with sp^3 contents of ~50 at% and nanohardness as high as ~39 GPa can be synthesized under optimum conditions of absorbed rf power, substrate bias voltage, working pressure, and gas flow rate. [Lu & Komvopoulos, 1999] The substrate bias voltage is of particular importance because it controls the kinetic energy of bombarding Ar^+ ions. The very low roughness and high hardness of *a*-C films synthesized under rf sputtering conditions of

optimum substrate bias voltage (typically, –200 V) may be attributed to the competing effects of ion bombardment, re-sputtering, and irradiation damage by the highly energetic Ar^+ ions. [Lu & Komvopoulos, 1999; Wan & Komvopoulos, 2006(A)]

The deposition of multi-layer *a*-C films comprising alternating hard/soft ultrathin carbon layers has been the objective of several previous studies. The low residual stress of multi-layer carbon films consisting of alternating sp^2- and sp^3-rich carbon layers has been attributed to stress relaxation induced by the soft (sp^2-rich) buffer layers; [Logothetidis et al., 2000] however, X-ray photoelectron spectroscopy (XPS) used in the former study to examine the cross-sectional structure of the ultrathin layers comprising the film has limited resolution for nanoscale structural analysis. Nanoindentation, XPS, and X-ray reflectivity (XRR) studies [Lu et al., 2003; Patsalas et al., 2005] of the microstructure and nanomechanical properties of multi-layer films consisting of alternating soft/hard *a*-C layers (deposited under rf sputtering conditions of zero (or floating) and –200 V substrate bias voltage, respectively) showed a film hardness of ~20 GPa, mass density of soft and hard layers equal to 2.0–2.2 and 2.5 g/cm^3, respectively, and an average sp^3 content of ~46 at%. Although the growth and physical properties of single *a*-C films deposited by rf sputtering have been thoroughly studied, a comprehensive analysis of the cross-sectional nanostructure of multi-layer soft/hard *a*-C films has not been reported.

The main objective of this study is to investigate the friction characteristics and nanostructure of multi-layer *a*-C films and compare them to those of single-layer *a*-C films deposited under similar rf sputtering conditions. The interdependence of surface morphology (roughness), friction properties (coefficient of friction), cross-sectional nanostructure (sp^2 and sp^3 hybridization), and residual stress is examined in the context of atomic force microscopy (AFM), surface force microscopy (SFM), transmission electron microscopy (TEM), electron energy loss spectroscopy (EELS), and curvature method results.

8.2 Experimental procedure

8.2.1 Film deposition

Single- and multi-layer *a*-C films of different thickness were deposited on smooth Si(100) substrates (root-mean-square (rms) roughness ≈ 0.1 nm) by sputtering a high-purity (~99.99%) graphite target with Ar^+ ions in a low-pressure sputtering system (Randex-2400 model, Perkin-Elmer). Before film deposition, the graphite target was cleaned by sputter-etching for 15 min and then the Si(100) substrate was sputtered for 3 min under conditions of forward rf power P_f = 250 W, working pressure p = 3 mTorr, and Ar gas flow rate f = 20 sccm to produce a clean and oxygen-free silicon surface. The multi-layer film comprised five alternating hard/soft ultrathin *a*-C layers, with the first layer deposited onto the Si(100) substrate and the last (top) layer being hard *a*-C layers. All depositions were performed in a pure Ar atmosphere under sputtering conditions of P_f = 750 W, p = 3 mTorr, and f = 20 sccm. Soft and hard *a*-C layers were synthesized under a substrate bias voltage V_s = 0 and –200 V, respectively. Besides the substrate bias voltage, all other deposition parameters of soft and hard *a*-C layers were identical. Single-layer *a*-C film deposition was performed under the same plasma discharge conditions with the hard layers of the multi-layer films (i.e., V_s = –200 V). The aforementioned plasma discharge

conditions have been found to produce *a*-C films exhibiting optimum properties. [Lu & Komvopoulos, 1999; Lu et al., 2001] For single-layer *a*-C films, the deposition time was $t \approx 4$, 6, and 12 min, corresponding to a film thickness $h \approx 30$, 60, and 120 nm, respectively. To obtain a total deposition time equal to that of single-layer *a*-C films of thickness $h \approx 30$, 60, and 120 nm, the deposition time of the soft and hard layers of the multi-layer *a*-C films was set at 36, 72, and 144 s, respectively. The effective hardness of single-layer *a*-C films deposited under the same sputtering conditions as the soft and hard *a*-C layers is equal to 19.7 and 39.2 GPa, respectively. [Lu & Komvopoulos, 2001]

8.2.2 Atomic force microscopy

The film surface roughness was determined from 2 × 2 μm^2 images acquired with an AFM (NanoScope II, Digital Instruments) operated in tapping mode. The film roughness was calculated as the mean value of at least four measurements obtained from different AFM surface images of each film. All the AFM images were obtained with Si tips having a nominal radius of curvature equal to ~10 nm.

8.2.3 Friction testing

The coefficient of friction of the synthesized *a*-C films was measured with a surface force microscope (SFM) consisting of a force transducer (Triboscope, Hysitron) interfaced with an AFM (NanoScope Ⅱ, Digital Instruments). The friction experiments were performed with a conical diamond tip having a nominal radius of curvature equal to ~20 μm, using a normal force in the range of 50–1200 μN, a constant sliding speed of 0.4 μm/s, and a lateral displacement (sliding distance) equal to 4 μm. The coefficient of friction was calculated as the ratio of the measured lateral (friction) force to the applied normal force. For statistical analysis, at least five friction tests were performed at different locations of each film surface and 300 coefficient of friction measurements obtained along the sliding track were used to calculate the steady-state coefficient of friction.

8.2.4 Microanalysis methods

Cross-sections of single- and multi-layer films deposited by RF sputtering were examined with the high-resolution TEM (Tecnai) to measure the film thickness. Details about the TEM sample preparation and the TEM system can be found in chapter 2. The details about the curve fitting method and calculation of the sp^3 fraction from EELS are given in Chapter 4.

8.2.5 Film thickness measurement

Film thickness measurements were obtained with a mechanical stylus profilometer (Dektak IID, Veeco Instruments) with 0.5 nm vertical resolution. The film thickness was determined by traversing the lightly loaded stylus over a step produced by partially masking the Si(100) substrate with a small piece of a sharply cleaved silicon wafer. To validate the profilometry

measurements, the thickness of single- and multi-layer *a*-C films ($t \approx 6$ min) measured with the profilometer was confirmed by cross-sectional HRTEM and EELS.

8.2.5 Residual stress

The residual stress in the films was determined from the sample curvature measured with a Flexus system (KLA-Tencor FLX-2320). For these measurements, 4-inch-diameter p-type Si(100) wafers were coated with 60-nm-thick *a*-C films synthesized under deposition conditions identical to those of single- and multi-layer *a*-C films of same thickness. The residual stress σ in the films was calculated from Stoney's equation (Eq. 2.7 in Chapter 2).

8.3 Results and discussion

Fig. 8.1 shows that, for a fixed forward rf power, the thickness of both single- and multi-layer *a*-C films varies linearly with the deposition time, in accord with previous studies. [Wan & Komvopoulos, 2006(A)] The close agreement of the data implies a similar deposition rate of ~9.2 nm/min for both types of *a*-C films deposited under the present sputtering conditions.

Fig. 8.2 shows the variation of the coefficient of friction of single- and multi-layer *a*-C films with the normal force and film thickness. The results indicate that in the low-force range (i.e., <600 μN) the coefficient of friction decreases with the increase of the normal force in a nonlinear fashion. This trend indicates predominantly elastic deformation under sliding conditions of normal force <600 μN. It is well-known that the friction coefficient of elastic spherical contacts is inversely proportional to the cubic root of the normal force and that the friction force is mainly due to adhesion and roughness effects. [Lu et al., 2001] Fig. 8.3 shows a log-log plot of the coefficient of friction of ~120-nm-thick single-layer *a*-C films versus normal force. The slope of the best-fit line shown in Fig. 8.3 is equal to –0.34, confirming the dominance of elastic deformation at the sliding interface in the low-force range (<600 μN).

Fig. 8.2 also shows that the multi-layer *a*-C films consistently demonstrate lower friction than the single-layer *a*-C films regardless of the film thickness. This result may be explained by considering the surface roughness effect on friction. Fig. 8.4(a) and 8.4(b) show the coefficient of friction and rms roughness of single- and multi-layer *a*-C films versus film thickness, respectively, for a normal force of 150 μN. The coefficient of friction of both film types increases with the rms roughness; however, the rougher single-layer films yield significantly higher coefficients of friction than the multi-layer films.

Fig. 8.5 shows cross-sectional HRTEM images of single- and multi-layer *a*-C films of total thickness equal to ~60 nm. Figs. 8.5(a) and 8.5(c) show overall cross-sectional views, while Fig. 8.5(b) and 8.5(d) show high-magnification images of the interface between the Si(100) substrate and the bottom of *a*-C films. The single-layer film shows an overall uniform thickness (Fig. 8.5(a)), whereas the multi-layer film consists of five alternating hard/soft *a*-C layers distinguished by contrast differences (the three hard layers are darker than the two soft layers) (Fig. 8.5(c)). High-magnification images reveal the formation of crystalline nanodomains in both

single- and multi-layer *a*-C films (e.g., circled areas in Figs. 8.5(b) and 8.5(d), respectively). The formation of crystalline nanodomains has also been observed in a previous TEM study and have been attributed to carbon atom clusters ejected from the graphite target by the bombarding Ar^+ ions. [Wan & Komvopoulos, 2004] In addition, an intermixing ultrathin layer (~2–3 nm thick) can be observed at the interface of both films with the crystalline Si(100) substrate, also in agreement with previous findings. [Wan & Komvopoulos, 2004]

Figs. 8.6(a) and 8.6(b) show the through-thickness structure of ~60-nm-thick single- and multi-layer *a*-C films, respectively. The normalized carbon intensity was obtained by integrating the EELS spectrum from 280 to 305 eV, while the sp^3 depth profiles were calculated from the C K-edge spectra using Eq. 4.2. The carbon atom concentration and sp^3 distribution through the film thickness reveal the existence of different regions. Fig. 8.6(a) indicates that the single-layer *a*-C film comprises the following five distinct regions: (i) *crystalline substrate* (the carbon signal intensity is not detectable because the substrate consists of silicon); (ii) *interface layer* (both the carbon concentration and the sp^3 content increase sharply); (iii) *bulk film* (small variation in carbon concentration and almost constant sp^3 content); (iv) *surface layer* (both the carbon concentration and the sp^3 fraction decrease sharply); (v) *capping layer* (the carbon intensity is not detectable because of the Au capping layer). Fig. 8.6(b) shows that within the bulk layer of the multi-layer *a*-C film, the carbon intensity changes periodically. The carbon intensity shows a positive slope in the hard layers and a negative slope in the soft layers, whereas the sp^3 fraction remains almost constant and there are no obvious differences between hard and soft layers. In addition, a comparison of the depth distributions shown in Figs. 8.6(a) and 8.6(b) indicates that the low in sp^3 intermixing and surface layers in the multi-layer film are thinner than those in the single-layer film.

Table 8.1 shows a comparison between the film thickness (measured from TEM and EELS), rms roughness, coefficient of friction, average sp^3 content of the bulk layer, and residual stress (Eq. 2.7) of ~60-nm-thick single- and multi-layer *a*-C films. The sum of the thicknesses of all the layers (i.e., intermixing, bulk, and surface layers) is referred to as the film thickness. The agreement between TEM and EELS results is fairly good. The surface roughness of multi-layer films is ~50% lower than that of the single-layer films, consistent with the lower coefficient of friction of multi-layer *a*-C films in the low range of normal force (Fig. 8.2). The similar sp^3 contents of single- and multi-layer films are also consistent with the similar coefficients of friction in the high normal force range (Fig. 8.2), where plastic shearing (plowing) is the dominant mode of deformation. Film plastic shearing greatly depends on the film nanostructure, particularly the type of carbon atom bonding. Since the sp^3 fraction controls the nanomechanical properties, the single- and multi-layer films should exhibit similar plastic shear resistance, which explains the similar coefficients of friction in the high normal force range (i.e., >600 μN). In addition, despite the slightly higher sp^3 content of the bulk layer of multi-layer *a*-C films, the residual stress in these films is ~55% lower than that in single-layer *a*-C films. Thus, rf sputtering of alternating hard (V_s = –200 V) and soft (V_s = 0) ultrathin (~10 nm) *a*-C layers produces smoother carbon films possessing lower friction and significantly reduced residual stress and preserves the overall nanostructure (hybridization state) compared to single-layer films of same thickness deposited under the same sputtering conditions.

8.4 Conclusion

The deposition rate, roughness, coefficient of friction, residual stress and nanostructure of single- and multi-layer *a*-C films were examined in the light of profilometry, AFM, SFM, curvature method, HRTEM, and EELS results. The multi-layer films synthesized under low-pressure plasma discharge conditions of substrate bias voltage of 0 V (soft layers) and –200 V (hard layers) demonstrate smoother surface topographies, lower coefficient of friction, significantly reduced residual stress, and slightly higher sp^3 content compared to single-layer *a*-C films deposited under –200 V substrate bias voltage. Sliding under a normal force of <600 μN resulted in predominantly elastic deformation of both films; however, the multi-layer films exhibited significantly lower friction than single-layer films of similar thickness. TEM revealed the existence of crystalline nanodomains in both films, whereas EELS confirmed the existence of a layered structure consisting of intermixing, bulk, and surface layers. The results of this study show that the surface roughness, friction, and residual stress of rf sputtered *a*-C films can be greatly reduced by depositing alternating hard and soft ultrathin *a*-C layers.

Table 8.1 Total thickness determined from TEM and EELS analysis, rms roughness, coefficient of friction, average sp^3 fraction in bulk layer, and residual stress of ~60-nm-thick single- and multi-layer *a*-C films deposited by RF sputtering.

Film type	Film thickness (nm)		Roughness (nm)	Coefficient of friction	sp^3 in bulk layer (%)	Compressive residual stress (GPa)
	Measurement method					
	TEM	EELS				
single-layer	63.1	59.1	0.23 ± 0.02	0.17 ± 0.01	43.05 ± 0.90	7.20 ± 0.01
multi-layer	65.0	60.9	0.14 ± 0.01	0.13 ± 0.01	44.39 ± 1.59	3.26 ± 0.01

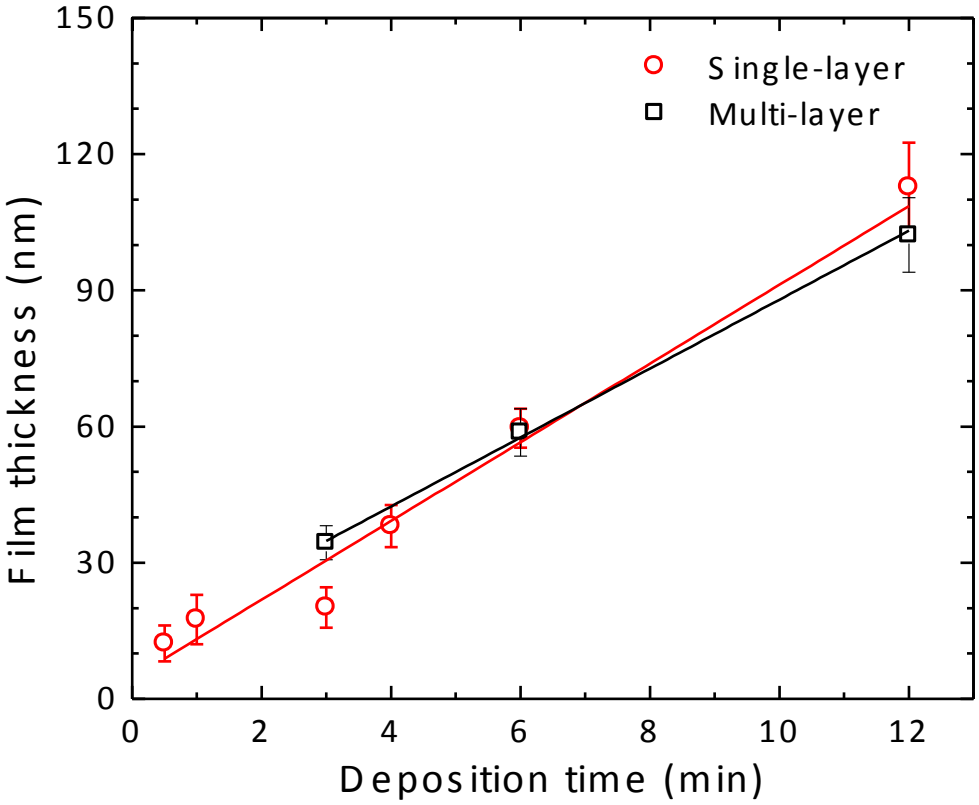

Fig. 8.1 Thickness of single- and multi-layer *a*-C films versus deposition time.

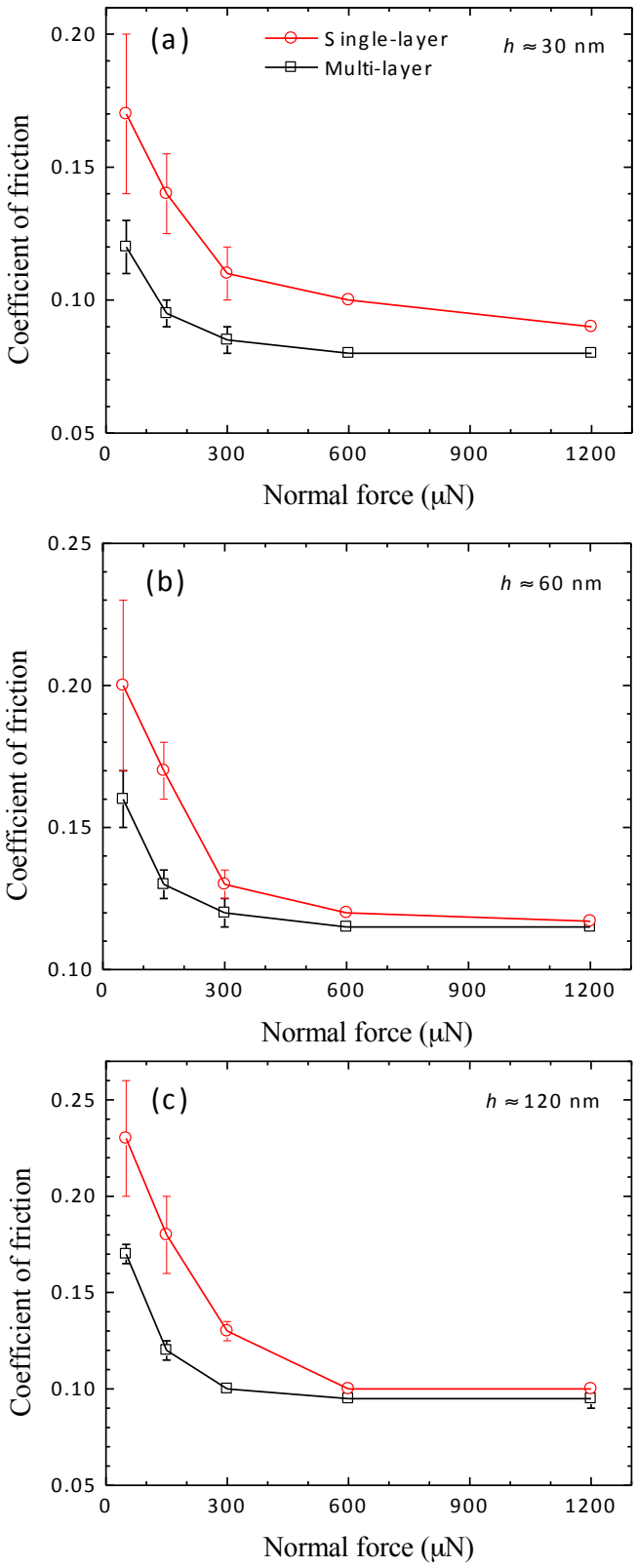

Fig. 8.2 Coefficient of friction of single- and multi-layer *a*-C films of thickness *h* approximately equal to (a) 30, (b) 60, and (c) 120 nm.

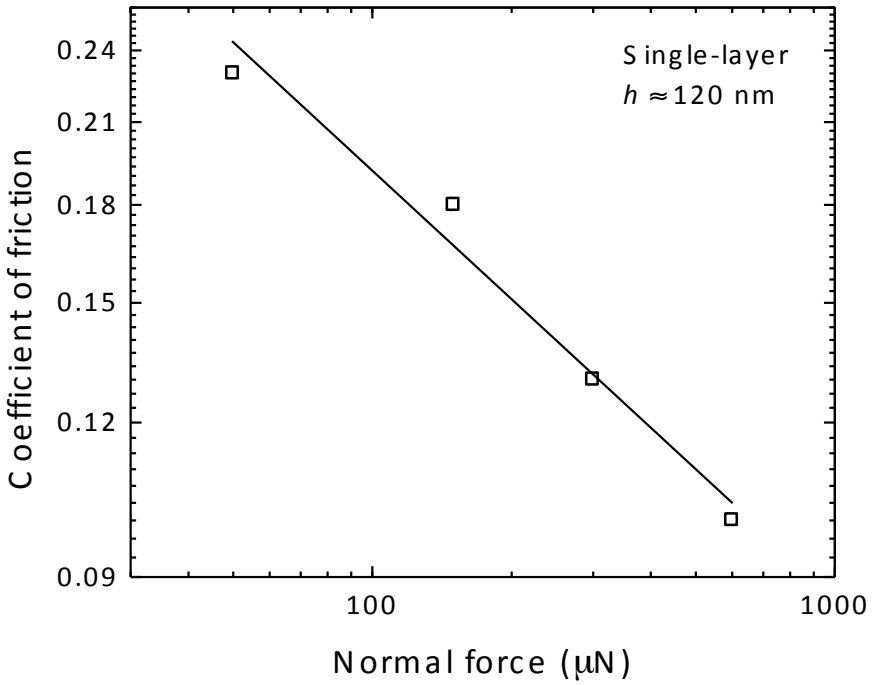

Fig. 8.3 Coefficient of friction of ~120-nm-thick single-layer *a*-C films versus normal force.

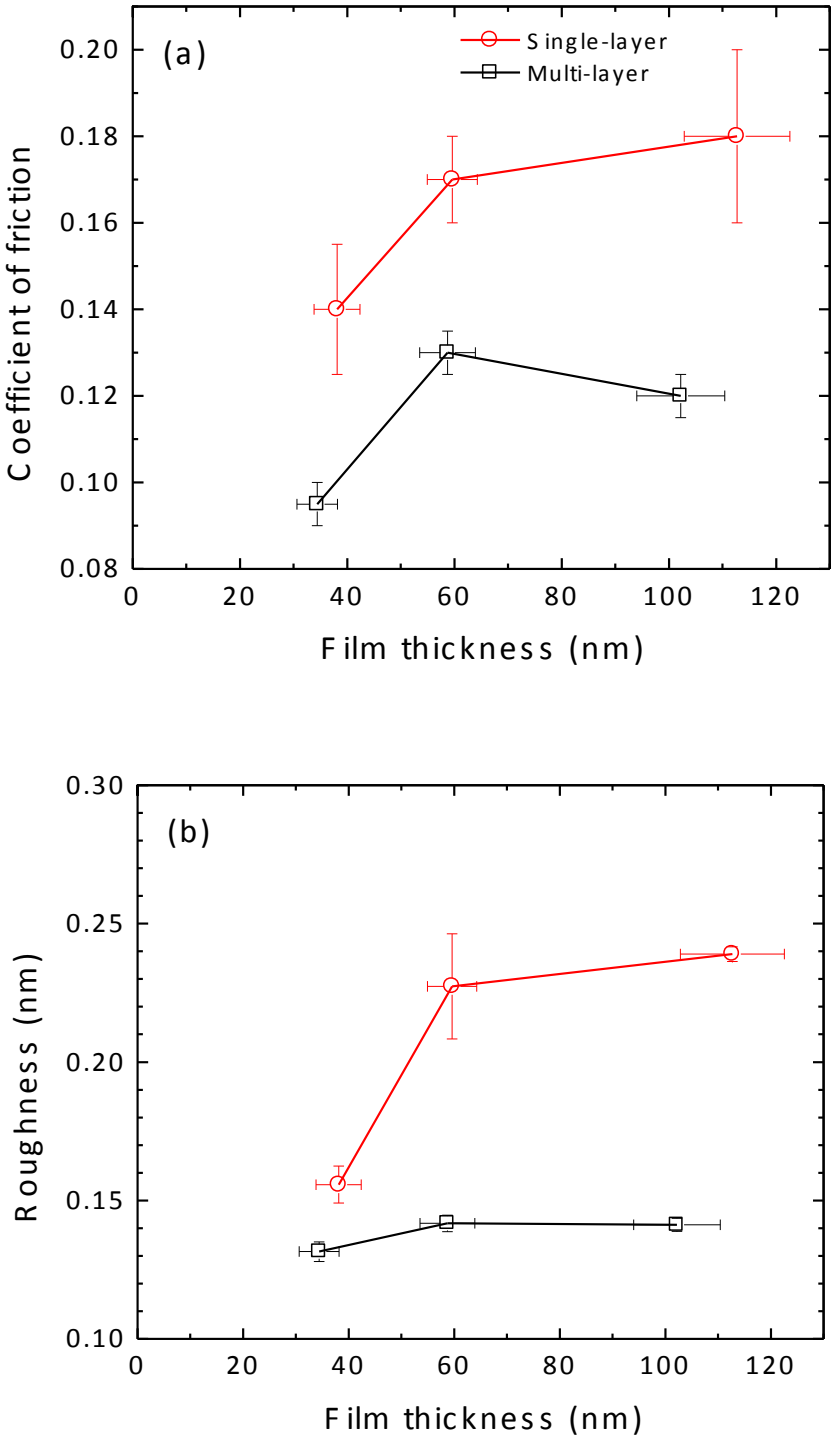

Fig. 8.4 (a) Coefficient of friction (normal force = 150 μN) and (b) rms roughness of single- and multi-layer *a*-C films versus film thickness.

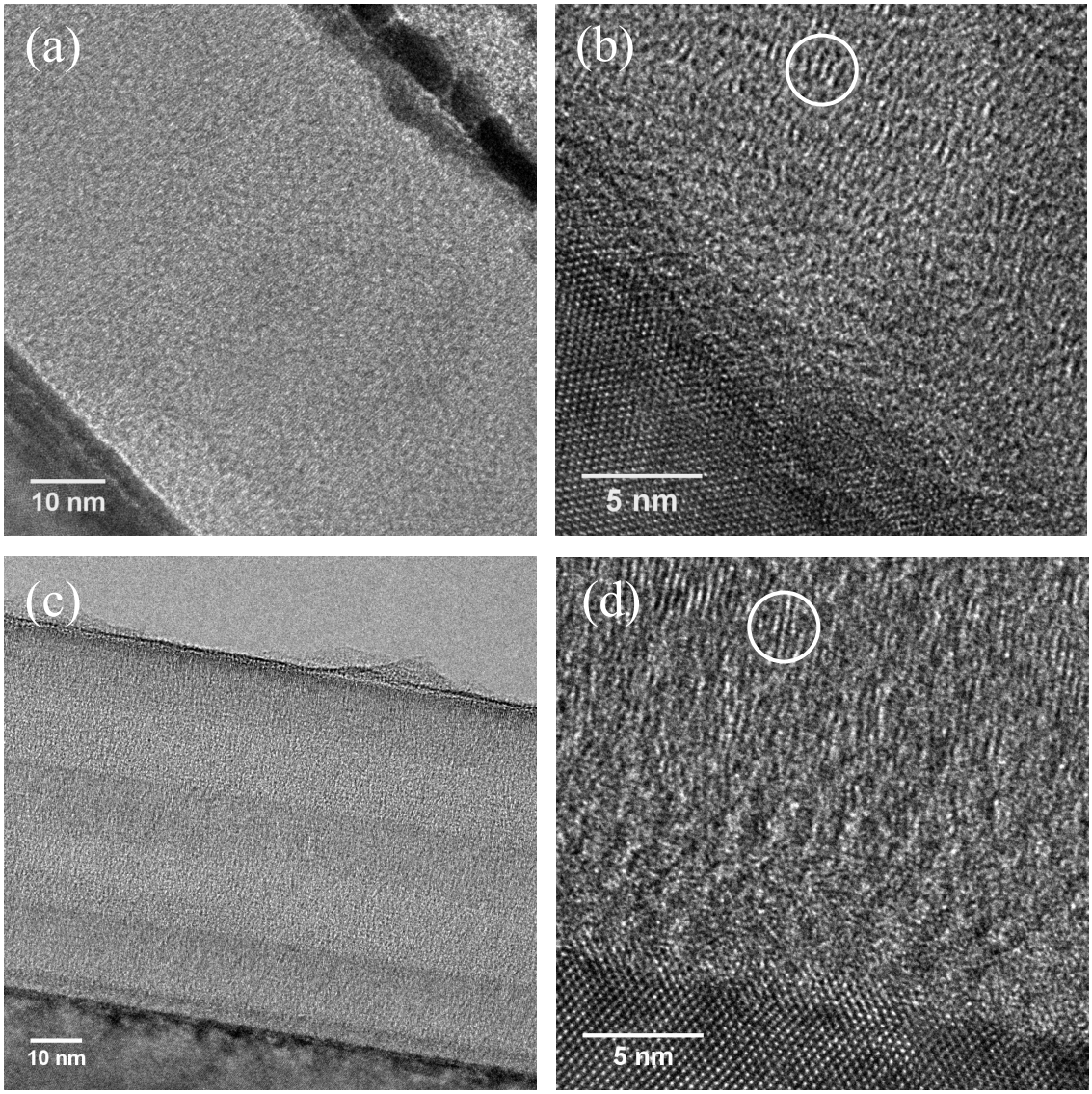

Fig. 8.5 Cross-sectional TEM images of ~60-nm-thick single- and multi-layer *a*-C films: (a, c) overviews of through-thickness film structure and (b, d) high-magnification images showing the formation of an intermixing layer at the film/substrate interface. The three hard layers appear as darker than the two soft layers in (c). The circles in (b) and (d) reveal the formation of crystalline nanodomains in the amorphous film structure.

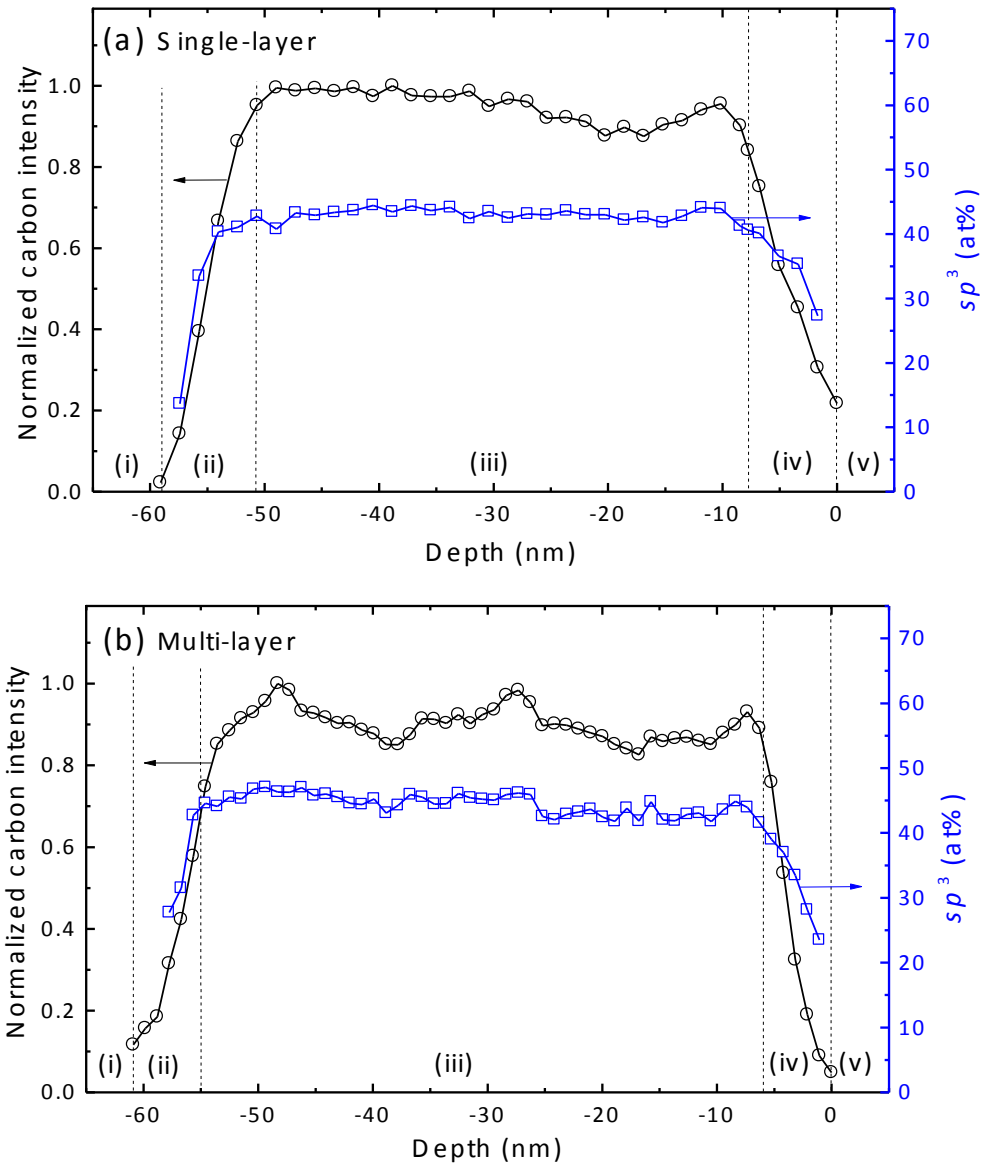

Fig. 8.6 Depth distributions of normalized intensity of C-K edge and sp^3 content calculated from the C K-edge EELS spectra of ~60-nm-thick (a) single- and (b) multi-layer *a*-C films. Dashed lines indicate the boundaries between (i) Si(100) substrate, (ii) intermixing layer, (iii) bulk layer, (iv) surface layer, and (v) capping Au layer.

Chapter 9 Conclusions

Comprehensive experimental studies of the structure, composition, properties, and stability of the ultrathin *a*-C films used as protective overcoats in hard disks were carried out in this dissertation. The *a*-C film characteristics were studied with various analytical characterization methods, including AFM, XPS, Raman spectroscopy, TEM, STEM/EELS, nanoindentation/scratch, and stress measurement. The FCVA deposition process parameters were optimized to minimize the thickness, in particular, that of the interface and surface layers of the *a*-C films, while maintaining the protective properties of the films. The thermal stability of both PECVD- and FCVA-deposited carbon films was studied under rapid thermal annealing conditions. The effect of the substrate bias voltage was given special consideration, and multi-layer carbon films were deposited to improve the tribomechanical properties and reduce the residual stress of RF sputtered *a*-C films. The main conclusions of this dissertation can be summarized as following:

RF sputtered *a*-C films synthesized under low-pressure discharge conditions of substrate bias voltage equal to –200 V demonstrate minimum surface roughness and maximum reduced elastic modulus, hardness, and sp^3 content, whereas films deposited under discharge conditions of –100 V substrate bias voltage exhibit minimum coefficient of friction. A particle collision analysis was introduced, which yields a proportionality relation of the sp^3 fraction with the average kinetic energy of surface carbon atoms, Ar^+ ion flux, and sputtering yield, and shows a similar trend with the variation of experimentally measured sp^3 fraction with substrate bias voltage. The optimum substrate bias voltage determined from this analysis was shown to be in good agreement with experimental findings. The dependence of the tribomechanical properties of *a*-C films on sp^3 content was revealed and various competing effects, such as re-sputtering, irradiation damage, and thermal spikes caused by impinging energetic Ar^+ ions, on the structural integrity of *a*-C films were elucidated in the context of obtained results.

A 65% duty cycle of substrate pulse biasing in FCVA deposition produces the smoothest and thinnest *a*-C films having a relatively high sp^3 content, whereas a 75% duty cycle of substrate pulse biasing yields *a*-C films with the highest sp^3 content and residual stress as well as thicker interface and buffer layers. These findings reveal a strong effect of the duty cycle of substrate pulse biasing on carbon atom hybridization and growth, development of compressive residual stress, and surface roughness of FCVA *a*-C films. The obtained results suggest that *a*-C films of thickness only a few nanometers can be deposited under optimum substrate pulse biasing FCVA conditions of 65% duty cycle.

Ar^+ ion sputter etching at 500 eV for 2 min changes the carbon film thickness and structure as well as the thickness of the surface and intermixing (interface) layers of PECVD *a*-C films; however, the effect on the thickness of FCVA *a*-Cs film was secondary. In addition, the thickness and sp^3 fraction in the bulk layer of PECVD and FCVA *a*-C films subjected to a 2-min 500-eV Ar^+ ion bombardment show no obvious changes. For longer sputter etching time (4 min), the thickness of all layers decreased and the average sp^3 fraction decreased from 59.1 to 51.9 at% for FCVA *a*-C films. The results of the present study indicate that, within an appropriate treatment time, Ar^+ ion sputter etching can reduce the thickness of the surface and intermixing layers, while preserving the sp^3 fraction and thickness of the bulk layer of both PECVD and

FCVA *a*-C films. The results also show that post-deposition Ar^+ ion sputter etching is a feasible method for improving the cross-sectional uniformity of *a*-C films.

With the introduction of an ultrathin (~1 nm) buffer layer under zero substrate bias voltage, the thickness of the interface (intermixing) layer was reduced by 58% and the sp^3 content of the bulk layer of bilayer *a*-C films was not affected, which is critical to preserving the properties of magnetic media. The results indicate that bilayer deposition helps to largely reduce the thickness of the intermixing layer, while preserving the sp^3 content of the bulk layer of *a*-C films. This provides a valuable method for improving the cross-sectional uniformity of *a*-C films, increase the average sp^3 content of the film, and, potentially, increase the resistance to corrosion and mechanical deformation/scratching and wear damage.

RTA treatment at 650 ℃ for 1 s of PECVD *a*-C:H films yielded an increase in the intermixing layer thickness by ~0.9 nm and a decrease in sp^3 content of the bulk layer of PECVD films by 4.5%. Under the same RTA conditions, the FCVA *a*-C films exhibited insignificant changes in both thickness and sp^3 content, revealing a superior structural stability over the PECVD films.

The multi-layer films synthesized by RF sputtering under low-pressure plasma discharge conditions of substrate bias voltage of 0 V (soft layers) and –200 V (hard layers) demonstrated smoother surface topographies, lower coefficient of friction, significantly reduced residual stress, and slightly higher sp^3 content compared to single-layer *a*-C films deposited under –200 V substrate bias voltage. Sliding under a normal force of <600 μN resulted in predominantly elastic deformation of both films; however, the multi-layer films exhibited significantly lower friction than single-layer films of similar thickness. The existence of crystalline nanodomains in both films and a layered structure consisting of intermixing, bulk, and surface layers were revealed in this study. It was shown that the surface roughness, friction, and residual stress of RF sputtered *a*-C films can be greatly reduced by depositing alternating hard and soft ultrathin (~10 nm) *a*-C layers.

References

Aisenberg, S., & Chabot, R. (1971). Ion-Beam Deposition of Thin Films of Diamondlike Carbon. *Journal of applied physics*, *42*(7), 2953-2958.

Anders, S., Anders, A., Brown, I. G., Wei, B., Komvopoulos, K., Ager, J. W., & Yu, K. M. (1994). Effect of vacuum arc deposition parameters on the properties of amorphous carbon thin films. *Surface and Coatings Technology*, *68*, 388-393.

Anders, A., Fong, W., Kulkarni, A. V., Ryan, F. W., & Bhatia, C. S. (2001). Ultrathin diamond-like carbon films deposited by filtered carbon vacuum arcs. *Plasma Science, IEEE Transactions on*, *29*(5), 768-775.

Anders, A. (2002). Energetic deposition using filtered cathodic arc plasmas. *Vacuum*, *67*(3), 673-686.

Anders, A. (2009). *Cathodic arcs: from fractal spots to energetic condensation*(Vol. 50). Springer Science & Business Media.

Baibich, M. N., Broto, J. M., Fert, A., Van Dau, F. N., Petroff, F., Etienne, P., ... & Chazelas, J. (1988). Giant magnetoresistance of (001) Fe/(001) Cr magnetic superlattices. *Physical review letters*, *61*(21), 2472.

Bandić, Z. Z., & Victora, R. H. (2008). Advances in magnetic data storage technologies. *Proceedings of the IEEE*, *11*(96), 1749-1753.

Beghi, M. G., Ferrari, A. C., Teo, K. B. K., Robertson, J., Bottani, C. E., Libassi, A., & Tanner, B. K. (2002). Bonding and mechanical properties of ultrathin diamond-like carbon films. *Applied physics letters*, *81*(20), 3804-3806.

Bhushan, B. (2010). Nanotribology of ultrathin and hard amorphous carbon films. In *Springer Handbook of Nanotechnology* (pp. 1269-1308). Springer Berlin Heidelberg.

Binnig, G., Quate, C. F., & Gerber, C. (1986). Atomic force microscope. *Physical review letters*, *56*(9), 930.

Brown, I. G. (1998). Cathodic arc deposition of films. *Annual review of materials science*, *28*(1), 243-269.

Casiraghi, C., Ferrari, A. C., Ohr, R., Chu, D., & Robertson, J. (2004A). Surface properties of ultra-thin tetrahedral amorphous carbon films for magnetic storage technology. *Diamond and related materials*, *13*(4), 1416-1421.

Casiraghi, C., Ferrari, A. C., Robertson, J., Ohr, R., Gradowski, M. V., Schneider, D., & Hilgers, H. (2004B). Ultra-thin carbon layer for high density magnetic storage devices. *Diamond and related materials*, *13*(4), 1480-1485.

Cheah, L. K., Shi, X., Liu, E., & Tay, B. K. (1999). Electron field emission properties of tetrahedral amorphous carbon films. *Journal of applied physics*, *85*(9), 6816-6821.

Chhowalla, M., Yin, Y., Amaratunga, G. A. J., McKenzie, D. R., & Frauenheim, T. (1996). Highly tetrahedral amorphous carbon films with low stress. *Applied physics letters*, *69*(16), 2344-2346.

Chhowalla, M., & Amaratunga, G. A. J. (2001). Strongly adhering and thick highly tetrahedral amorphous carbon (ta–C) thin films via surface modification by implantation. *Journal of Materials Research*, *16*(01), 5-8.

Choy, K. L. (2003). Chemical vapour deposition of coatings. *Progress in materials science*, *48*(2), 57-170.

Chu, P. K., & Li, L. (2006). Characterization of amorphous and nanocrystalline carbon films. *Materials Chemistry and Physics*, *96*(2), 253-277.

Chung, C. K., Peng, C. C., Wu, B. H., & Chen, T. S. (2007). Residual stress and hardness behaviors of the two-layer C/Si films. *Surface and Coatings Technology*, *202*(4), 1149-1153.

Coburn, J. W., & Kay, E. (1972). Positive-ion bombardment of substrates in rf diode glow discharge sputtering. *Journal of Applied Physics*, *43*(12), 4965-4971.

Collins, C. B., Davanloo, F., Jander, D. R., Lee, T. J., Park, H., & You, J. H. (1991). Microstructure of amorphic diamond films. Journal of applied physics, 69(11), 7862-7870.

Collins, C. B., Davanloo, F., Lee, T. J., Park, H., & You, J. H. (1993). Noncrystalline films with the chemistry, bonding, and properties of diamond.*Journal of Vacuum Science & Technology B*, *11*(5), 1936-1941.

Cuomo, J. J., Doyle, J. P., Bruley, J., & Liu, J. C. (1991). Sputter deposition of dense diamond-like carbon films at low temperature. *Applied physics letters*,*58*(5), 466-468.

Dai, W., & Wang, A. (2011). Deposition and properties of Al-containing diamond-like carbon films by a hybrid ion beam sources. *Journal of Alloys and Compounds*, *509*(13), 4626-4631.

Daughton, J., Brown, J., Chen, E., Beech, R., Pohm, A., & Kude, W. (1994). Magnetic field sensors using GMR multilayer. *Magnetics, IEEE Transactions on*, *30*(6), 4608-4610.

Davanloo, F., Juengerman, E. M., Jander, D. R., Lee, T. J., & Collins, C. B. (1990). Amorphic diamond films produced by a laser plasma source. *Journal of Applied Physics*, *67*(4), 2081-2087.

Davanloo, F., Lee, T. J., Jander, D. R., You, J. H., Park, H., & Collins, C. B. (1992). Mechanical and adhesion properties of amorphic diamond films. *Thin Solid Films*, *212*(1), 216-219.

Davis, C. A. (1993). A simple model for the formation of compressive stress in thin films by ion bombardment. *Thin solid films*, *226*(1), 30 -34.

Davis, C. A., Knowles, K. M., & Amaratunga, G. A. J. (1995). Cross-sectional structure of tetrahedral amorphous carbon thin films. *Surface and Coatings Technology*, *76*, 316-321.

Davis, C. A., Amaratunga, G. A. J., & Knowles, K. M. (1998). Growth mechanism and cross-sectional structure of tetrahedral amorphous carbon thin films. *Physical review letters*, *80*(15), 3280.

Egerton, R. (2011). *Electron energy-loss spectroscopy in the electron microscope*. (3rd ed., Springer Science & Business Media, New York), Ch. 3, 111–229.

Erdemir, A., & Donnet, C. (2006). Tribology of diamond-like carbon films: recent progress and future prospects. *Journal of Physics D: Applied Physics*, *39*(18), R311.

Fallon, P. J., Veerasamy, V. S., Davis, C. A., Robertson, J., Amaratunga, G. A. J., Milne, W. I., & Koskinen, J. (1993). Properties of filtered-ion-beam-deposited diamondlike carbon as a function of ion energy. *Physical Review B*, *48*(7), 4777.

Ferrari, A. C., Libassi, A., Tanner, B. K., Stolojan, V., Yuan, J., Brown, L. M., Rodil, S. E., Kleinsorge. B., & Robertson, J. (2000). Density, sp^3 fraction, and cross-sectional structure of amorphous carbon films determined by X-ray reflectivity and electron energy-loss spectroscopy. *Physical Review B*, *62*(16), 11089.

Ferrari, A. C. (2004). Diamond-like carbon for magnetic storage disks. *Surface and Coatings Technology*, *180*, 190-206.

Field, J. E. (1993) *Properties of Diamond* (Academic Press, London, UK).

Friedmann, T. A., Sullivan, J. P., Knapp, J. A., Tallant, D. R., Follstaedt, D. M., Medlin, D. L., & Mirkarimi, P. B. (1997). Thick stress-free amorphous-tetrahedral carbon films with hardness near that of diamond. *Applied Physics Letters*, *71*(26), 3820-3822.

Fung, M. K., Lai, K . H., Chan, C. Y., Bello, I., Lee, C. S., Lee, S. T., Mao, D. S. and Wang, X. (2000). Mechanical properties and corrosion studies of amorphous carbon on magnetic disks prepared by ECR plasma technique. *Thin Solid Films*, 368, 198-202.

Geim, A. K., & Novoselov, K. S. (2007). The rise of graphene. *Nature materials*, *6*(3), 183-191.

Goglia, P. R., Berkowitz, J., Hoehn, J., Xidis, A., & Stover, L. (2001). Diamond-like carbon applications in high density hard disc recording heads. *Diamond and Related Materials*, *10*(2), 271-277.

Grierson, D. S., Sumant, A. V., Konicek, A. R., Friedmann, T. A., Sullivan, J. P., & Carpick, R. W. (2010). Thermal stability and rehybridization of carbon bonding in tetrahedral amorphous carbon. *Journal of Applied Physics*, *107*(3), 033523.

Grill, A. (1999). Diamond-like carbon: state of the art. *Diamond and related materials*, *8*(2), 428-434.

Grill, A., & Meyerson, B. S. (1994). Development and status of diamondlike carbon. *Synthetic diamond: Emerging CVD science and technology*, 91-141.

Han, H., Ryan, F., & McClure, M. (1999). Ultra-thin tetrahedral amorphous carbon film as slider overcoat for high areal density magnetic recording. *Surface and Coatings Technology*, *120*, 579-584.

Hauert, R. (2004). An overview on the tribological behavior of diamond-like carbon in technical and medical applications. *Tribology International*, *37*(11), 991-1003.

Hauert, R. (2008). DLC films in biomedical applications. In *Tribology of Diamond-Like Carbon Films* (pp. 494-509). Springer US.

He, H., & Thorpe, M. F. (1985). Elastic properties of glasses. *Physical Review Letters*, *54*(19), 2107.

Hofsäss, H., Feldermann, H., Merk, R., Sebastian, M., & Ronning, C. (1998). Cylindrical spike model for the formation of diamondlike thin films by ion deposition. *Applied Physics A*, *66*(2), 153-181.

Hsu, C. Y., Chen, L. Y., & Hong, F. C. N. (1998). Properties of diamond-like carbon films deposited by ion plating with a pulsed substrate bias. *Diamond and related materials*, *7*(6), 884-891.

Iijima, S. (1991). Helical microtubules of graphitic carbon. *Nature*, *354*(6348), 56-58.

Ishikawa, J., Takeiri, Y., Ogawa, K., & Takagi, T. (1987). Transparent carbon film prepared by mass-separated negative-carbon-ion-beam deposition. *Journal of applied physics*, *61*(7), 2509-2515.

Jalili, N., & Laxminarayana, K. (2004). A review of atomic force microscopy imaging systems: application to molecular metrology and biological sciences. *Mechatronics*, *14*(8), 907-945.

Jones, P. M., Ahner, J., Platt, C. L., Tang, H., & Hohlfeld, J. (2014). Understanding Disk Carbon Loss Kinetics for Heat Assisted Magnetic Recording. *Magnetics, IEEE Transactions on*, *50*(3), 144-147.

Jungnickel, G., Kühn, M., Deutschmann, S., Richter, F., Stephan, U., Blaudeck, P., & Frauenheim, T. (1994). Structure and chemical bonding in high density amorphous carbon. *Diamond and Related Materials*, *3*(7), 1056-1065.

Kalish, R., Lifshitz, Y., Nugent, K., & Prawer, S. (1999). Thermal stability and relaxation in diamond-like-carbon. A Raman study of films with different sp^3 fractions (ta-C to aC). *Applied physics letters*, *74*, 2936.

Keller, J. H., & Pennebaker, W. B. (1979). Electrical properties of RF sputtering systems. *IBM Journal of Research and Development*, *23*(1), 3-15.

Kelly, B. T. (1981). *Physics of Graphite*, Applied Science Publishers. London, UK.

Khizroev, S. K., Kryder, M. H., Ikeda, Y., Rubin, K., Arnett, P., Best, M., & Thompson, D. A. (1999). Recording heads with track widths suitable for 100 Gbit/in^2 density. *Magnetics, IEEE Transactions on*, 35(5), 2544-2546.

Koenig, H. R., & Maissel, L. I. (1970). Application of rf discharges to sputtering. *IBM Journal of research and development*, *14*(2), 168-171.

Köhler, K., Coburn, J. W., Horne, D. E., Kay, E., & Keller, J. H. (1985). Plasma potentials of 13.56-MHz rf argon glow discharges in a planar system. *Journal of applied physics*, *57*(1), 59-66.

Kovarik, P., Bourdon, E. B. D., & Prince, R. H. (1993). Electron-energy-loss characterization of laser-deposited *a*-C, *a*-C:H, and diamond films. *Physical Review B*, *48*(16), 12123.

Kryder, M. H., Gage, E. C., McDaniel, T. W., Challener, W., Rottmayer, R. E., Ju, G., Hsia, Y.-T. & Erden, M. F. (2008). Heat assisted magnetic recording. *Proceedings of the IEEE*, *96*(11), 1810-1835.

Kumar, S., Dixit, P. N., Sarangi, D., & Bhattacharyya, R. (1999). Possible solution to the problem of high built-up stresses in diamond-like carbon films. *Journal of applied physics*, *85*(7), 3866-3876.

Kundu, S., Dwivedi, N., Satyanarayana, N., Yeo, R. J., Ahner, J., Jones, P. M., & Bhatia, C. S. (2014). Probing the Role of Carbon Microstructure on the Thermal Stability and Performance of Ultrathin (< 2 nm) Overcoats on $L1_0$ FePt Media for Heat-Assisted Magnetic Recording. *ACS applied materials & interfaces*, *7*(1), 158-165.

Lee, C. S., Lee, K. R., Eun, K. Y., Yoon, K. H., & Han, J. H. (2002). Structure and properties of Si incorporated tetrahedral amorphous carbon films prepared by hybrid filtered vacuum arc process. *Diamond and Related Materials*, *11*(2), 198-203.

Leng, Q., Han, H., Mao, M., Hiner, C., & Ryan, F. (2000). Magnetic dead layers in NiFe/Ta and NiFe/Si/diamond-like carbon films. *Journal of Applied Physics*, *87*(9), 6621-6623.

Lifshitz, Y., Kasi, S. R., & Rabalais, J. W. (1989). Subplantation model for film growth from hyperthermal species: Application to diamond. *Physical review letters*, *62*(11), 1290.

Lifshitz, Y., Kasi, S. R., Rabalais, J. W., & Eckstein, W. (1990). Subplantation model for film growth from hyperthermal species. *Physical Review B*, *41*(15), 10468.

Lifshitz, Y., Lempert, G. D., & Grossman, E. (1994). Substantiation of subplantation model for diamondlike film growth by atomic force microscopy. *Physical review letters*, *72*(17), 2753.

Lifshitz, Y. (1999). Diamond-like carbon—present status. *Diamond and Related materials*, *8*(8), 1659-1676.

Lieberman, M. A., & Lichtenberg, A. J. (1994). *Principles of plasma discharges and materials processing*. John Wiley, New York.

Lindhard, J., Nielsen, V., Scharff, M., & Thomsen, P. V. (1963A). *Integral equations governing radiation effects*. *Matematisk-fysiske Meddelelser Danske Videnskabernes Selskab,* 33(10) 1–42.

Lindhard, J., Scharff, M., & Schiøtt, H. E. (1963). *Range concepts and heavy ion ranges*. Munksgaard. *Matematisk-fysiske Meddelelser Danske Videnskabernes Selskab,* 33(14) 1–42.

Linhard, J., Nielsen, V., & Scharff, M. (1968). Approximation method in classical scattering by screened coulomb fields. *Matematisk-fysiske Meddelelser Danske Videnskabernes Selskab,* 36(10) 1–32

Logothetidis, S., Charitidis, C., Gioti, M., Panayiotatos, Y., Handrea, M., & Kautek, W. (2000). Comprehensive study on the properties of multilayered amorphous carbon films. *Diamond and Related Materials*, *9*(3), 756-760.

Lu, W., & Komvopoulos, K. (1999). Dependence of growth and nanomechanical properties of ultrathin amorphous carbon films on radio frequency sputtering conditions. *Journal of applied physics*, *86*(4), 2268-2277.

Lu, W., & Komvopoulos, K. (2000). Implanted argon atoms as sensing probes of residual stress in ultrathin films. *Applied Physics Letters*, *76*, 3206.

Lu, W., Komvopoulos, K., & Yeh, S. W. (2001). Stability of ultrathin amorphous carbon films deposited on smooth silicon substrates by radio frequency sputtering. *Journal of Applied Physics*, *89*, 2422-2433.

Lu, W., & Komvopoulos, K. (2001). Nanotribological and nanomechanical properties of ultrathin amorphous carbon films synthesized by radio frequency sputtering. *Journal of tribology*, *123*(3), 641-650.

Lu, W., Komvopoulos, K., Patsalas, P., Charitidis, C., Gioti, M., & Logothetidis, S. (2003). Microstructure and nanomechanical and optical properties of single-and multi-layer carbon films synthesized by radio frequency sputtering. *Surface and Coatings Technology*, *168*(1), 12-22.

Ma, X. G., Komvopoulos, K., Wan, D., Bogy, D. B., & Kim, Y. S. (2003). Effects of film thickness and contact load on nanotribological properties of sputtered amorphous carbon thin films. *Wear*, *254*(10), 1010-1018.

Mangolini, F., Rose, F., Hilbert, J., & Carpick, R. W. (2013). Thermally induced evolution of hydrogenated amorphous carbon. *Applied Physics Letters*, *103*(16), 161605.

Marchon, B., Guo, X. C., Pathem, B. K., Rose, F., Dai, Q., Feliss, N., Schreck, E. ; Reiner, J. ; Mosendz, O.; Takano, K. ; Hoa Do ; Burns, J. ; Saito, Y. (2014). Head–Disk Interface Materials Issues in Heat-Assisted Magnetic Recording. *Magnetics, IEEE Transactions on*, *50*(3), 137-143.

Mate, C. M., Yen, B. K., Miller, D. C., Toney, M. F., Scarpulla, M., & Frommer, J. E. (2000). New methodologies for measuring film thickness, coverage, and topography. *IEEE transactions on magnetics*, *36*(1), 110-114.

Matsunami, N., Yamamura, Y., Itikawa, Y., Itoh, N., Kazumata, Y., Miyagawa, S., Morita, K., Shimizu, R., Tawara, H. (1984). Energy dependence of the ion-induced sputtering yields of monatomic solids. *Atomic Data and Nuclear Data Tables*, *31*(1), 1-80.

McKenzie, D. R., Muller, D., & Pailthorpe, B. A. (1991). Compressive-stress-induced formation of thin-film tetrahedral amorphous carbon. *Physical review letters*, *67*(6), 773.

McKenzie, D. R. (1996). Tetrahedral bonding in amorphous carbon. *Reports on Progress in Physics*, *59*(12), 1611-1664.

Monteiro, O. R. (2001). Thin Film Synthesis by Energetic Condensation 1. *Annual Review of Materials Research*, *31*(1), 111-137.

Nastasi, M. A., & Mayer, J. W. (2006). *Ion implantation and synthesis of materials* (Vol. 80). Springer-Verlag, Berlin Heidelberg, Germany, 49–61.

Novoselov, K. S., Geim, A. K., Morozov, S. V., Jiang, D., Zhang, Y., Dubonos, S. A., Grigorieva, I. V., & Firsov, A. A. (2004). Electric field effect in atomically thin carbon films. *Science*, *306*(5696), 666-669.

Orhing, M. (2001). *Materials Science of Thin Films: Deposition and Structure*, 2nd ed., Academic, New York, 1992.

Oliver, W. C., & Pharr, G. M. (1992). An improved technique for determining hardness and elastic modulus using load and displacement sensing indentation experiments. *Journal of materials research*, *7*(06), 1564-1583.

Oliver, W. C., & Pharr, G. M. (2004). Measurement of hardness and elastic modulus by instrumented indentation: Advances in understanding and refinements to methodology. *Journal of materials research*, *19*(01), 3-20.

Patsalas, P., & Logothetidis, S. (2000). Surface and Bulk Microstructural Modifications in Amorphous Carbon Films after Post-Growth Low Energy Ion Beam Irradiation. In *MRS Proceedings* (Vol. 650, pp. R3-42). Cambridge University Press.

Patsalas, P., & Logothetidis, S. (2000). The effect of postgrowth ion irradiation on the microstructure and the interface properties of amorphous carbon films on silicon. *Journal of Applied Physics*, *88*(11), 6346-6354.

Patsalas, P., Logothetidis, S., & Kelires, P. C. (2005). Surface and interface morphology and structure of amorphous carbon thin and multilayer films. *Diamond and related materials*, *14*(8), 1241-1254.

Petereit, B., Siemroth, P., Schneider, H. H., & Hilgers, H. (2003). High current filtered arc deposition for ultra thin carbon overcoats on magnetic hard disks and read-write heads. *Surface and Coatings Technology*, *174*, 648-650.

Pharr, G. M., Callahan, D. L., McAdams, S. D., Tsui, T. Y., Anders, S., Anders, A., Ager III, J. W., Brown, I. G., Bhatia, C. S., Silva, S. R. P., & Robertson, J. (1996). Hardness, elastic modulus, and structure of very hard carbon films produced by cathodic-arc deposition with substrate pulse biasing. *Applied physics letters*, *68*(6), 779-781.

Riedo, E., Comin, F., Chevrier, J., Schmithusen, F., Decossas, S., & Sancrotti, M. (2000). Structural properties and surface morphology of laser-deposited amorphous carbon and carbon nitride films. *Surface and Coatings Technology*,*125*(1), 124-128.

Rismani, E., Sinha, S. K., Yang, H., & Bhatia, C. S. (2012). Effect of pretreatment of Si interlayer by energetic C^+ ions on the improved nanotribological properties of magnetic head overcoat. *Journal of Applied Physics*, *111*(8), 084902.

Robertson, J. (1992). Mechanical properties and coordinations of amorphous carbons. *Physical review letters*, *68*(2), 220.

Robertson, J. (1993). Deposition mechanisms for promoting sp 3 bonding in diamond-like carbon. *Diamond and Related Materials*, *2*(5), 984-989.

Robertson, J. (1994A). Diamond-like carbon. *Pure and applied chemistry*, *66*(9), 1789-1796.

Robertson, J. (1994B). The deposition mechanism of diamond-like *a*-C and *a*-C:H. *Diamond and Related Materials*, *3*(4), 361-368.

Robertson, J. (1996). Deposition mechanism of cubic boron nitride. *Diamond and related materials*, *5*(3), 519-524.

Robertson, J. (2001). Ultrathin carbon coatings for magnetic storage technology. *Thin Solid Films*, *383*(1), 81-88.

Robertson, J. (2002). Diamond-like amorphous carbon. *Materials Science and Engineering: R: Reports*, *37*(4), 129-281.

Robertson, J. (2003). Requirements of ultrathin carbon coatings for magnetic storage technology. *Tribology International*, *36*(4), 405-415.

Rohlfing, E. A., Cox, D. M., & Kaldor, A. (1984). Production and characterization of supersonic carbon cluster beams. *The Journal of chemical physics*, *81*(7), 3322-3330.

Rose, F., Wang, N., Smith, R., Xiao, Q. F., Inaba, H., Matsumura, T., Saito, Y., Matsumoto, H., Dai Q., Marchon, B., Mangolini, F., & Carpick, R. W. (2014). Complete characterization by Raman spectroscopy of the structural properties of thin hydrogenated diamond-like carbon films exposed to rapid thermal annealing. *Journal of Applied Physics*, *116*(12), 123516.

Savvides, N., & Window, B. (1985). Diamondlike amorphous carbon films prepared by magnetron sputtering of graphite. *Journal of Vacuum Science & Technology A*, *3*(6), 2386-2390.

Schwan, J., Ulrich, S., Roth, H., Ehrhardt, H., Silva, S. R. P., Robertson, J., ... & Brenn, R. (1996). Tetrahedral amorphous carbon films prepared by magnetron sputtering and dc ion plating. *Journal of applied physics*, *79*(3), 1416-1422.

Schwan, J., Ulrich, S., Theel, T., Roth, H., Ehrhardt, H., Becker, P., & Silva, S. R. P. (1997). Stress-induced formation of high-density amorphous carbon thin films. *Journal of applied physics*, *82*(12), 6024-6030.

Sheeja, D., Tay, B. K., Lau, S. P., & Shi, X. (2001). Tribological properties and adhesive strength of DLC coatings prepared under different substrate bias voltages. *Wear*, *249*(5), 433-439.

Sheeja, D., Tay, B. K., Yu, L. J., Lau, S. P., Sze, J. Y., & Cheong, C. K. (2002). Effect of frequency and pulse width on the properties of ta: C films prepared by FCVA together with substrate pulse biasing. *Thin Solid Films*, *420*, 62-69.

Shi, B., & Meng, W. J. (2003). Intrinsic stresses and mechanical properties of Ti-containing hydrocarbon coatings. *Journal of applied physics*, *94*(1), 186-194.

Shin, J. K., Lee, C. S., Lee, K. R., & Eun, K. Y. (2001). Effect of residual stress on the Raman-spectrum analysis of tetrahedral amorphous carbon films. *Applied Physics Letters*, *78*(5), 631-633.

Shirley, D. A. (1972). High-resolution X-ray photoemission spectrum of the valence bands of gold. *Physical Review B*, *5*(12), 4709–4714.

Siegal, M. P., Provencio, P. N., Tallant, D. R., Simpson, R. L., Kleinsorge, B., & Milne, W. I. (2000). Bonding topologies in diamondlike amorphous-carbon films. *Applied Physics Letters*, *76*(15), 2047-2049.

Sigmund, P. (1969). Theory of sputtering. I. Sputtering yield of amorphous and polycrystalline targets. *Physical review*, *184*(2), 383-416

Silinskas, M., & Grigonis, A. (2002). Low energy post-growth irradiation of amorphous hydrogenated carbon (*a*-C:H) films. *Diamond and related materials*,*11*(3), 1026-1030.

Ravi, S., Silva, P., Xu, S., Tay, B. X., Tan, H. S., & Milne, W. I. (1996). Nanocrystallites in tetrahedral amorphous carbon films. *Applied physics letters*,*69*(4), 491-493.

Smith, E. and Dent, G. (2005). *Modern Raman spectroscopy: a practical approach.* John Wiley & Sons, Hoboken, NJ.

Srolovitz, D. J., & Goldiner, M. G. (1995). The thermodynamics and kinetics of film agglomeration. *JOM*, *47*(3), 31-36.

Stipe, B. C., Strand, T. C., Poon, C. C., Balamane, H., Boone, T. D., Katine, J. A., Li, J. L., Rawat, V., Nemoto, H., Hirotsune, A., Hellwig, O., Ruiz, R., Dobisz, E., Kercher, D. S., Robertson, N., Albrecht, T. R. & Terris, B. D. (2010). Magnetic recording at 1.5 Pb m^{-2} using an integrated plasmonic antenna. *Nature Photonics*, *4*(7), 484-488.

Sullivan, J. P., Friedmann, T. A., & Baca, A. G. (1997). Stress relaxation and thermal evolution of film properties in amorphous carbon. *Journal of Electronic Materials*, *26*(9), 1021-1029.

Tsai, H. C., & Bogy, D. B. (1987). Characterization of diamondlike carbon films and their application as overcoats on thin-film media for magnetic recording. *Journal of Vacuum Science & Technology A*, *5*(6), 3287-3312.

Vinnichenko, M., Gago, R., Huang, N., Leng, Y. X., Sun, H., Kreissig, U., ... & Maitz, M. F. (2004). Spectroscopic ellipsometry investigation of amorphous carbon films with different sp^3 content: relation with protein adsorption. *Thin Solid Films*, *455*, 530-534.

Voevodin, A. A., & Donley, M. S. (1996). Preparation of amorphous diamond-like carbon by pulsed laser deposition: a critical review. *Surface and Coatings Technology*, *82*(3), 199-213.

Wallace, R. L. (1951). The reproduction of magnetically recorded signals. *Bell System Technical Journal*, *30*(4), 1145-1173.

Wan, D., & Komvopoulos, K. (2004). Transmission electron microscopy and electron energy loss spectroscopy analysis of ultrathin amorphous carbon films. *Journal of materials research*, *19*(07), 2131-2136.

Wan, D., & Komvopoulos, K. (2006A). Effect of low-pressure plasma discharge conditions on the thickness and roughness of ultrathin films of amorphous carbon. *Journal of applied physics*, *100*(6), 063307.

Wan, D., & Komvopoulos, K. (2006B). Probabilistic analysis of tetrahedral carbon hybridization in amorphous carbon films. *Applied physics letters*, *88*(22), 221908.

Wan, D., & Komvopoulos, K. (2007). Tetrahedral and trigonal carbon atom hybridization in thin amorphous carbon films synthesized by radio-frequency sputtering. *The Journal of Physical Chemistry C*, *111*(27), 9891-9896.

Wang, N., & Komvopoulos, K. (2011). Thermal stability of ultrathin amorphous carbon films for energy-assisted magnetic recording. *Magnetics, IEEE Transactions on*, *47*(9), 2277-2282.

Wang, N., & Komvopoulos, K. (2012). Incidence angle effect of energetic carbon ions on deposition rate, topography, and structure of ultrathin amorphous carbon films deposited by filtered cathodic vacuum arc. *Magnetics, IEEE Transactions on*, *48*(7), 2220-2227.

Wang, N., & Komvopoulos, K. (2013). The multilayered structure of ultrathin amorphous carbon films synthesized by filtered cathodic vacuum arc deposition. *Journal of Materials Research*, *28*(16), 2124-2131.

Wang, N., Komvopoulos, K., Rose, F., & Marchon, B. (2013). Structural stability of hydrogenated amorphous carbon overcoats used in heat-assisted magnetic recording investigated by rapid thermal annealing. *Journal of Applied Physics*,*113*(8), 083517.

Wang, A. Y., Lee, K. R., Ahn, J. P., & Han, J. H. (2006). Structure and mechanical properties of W incorporated diamond-like carbon films prepared by a hybrid ion beam deposition technique. *Carbon*, *44*(9), 1826-1832.

Wang, Y., Li, H., Ji, L., Zhao, F., Liu, X., Kong, Q., Wang, Y., Quan, W., Zhou, H. & Chen, J. (2010). The effect of duty cycle on the microstructure and properties of graphite-like amorphous carbon films prepared by unbalanced magnetron sputtering. *Journal of Physics D: Applied Physics*, *43*(50), 505401.

Williams, D. B., & Carter, C. B., (2009) *Transmission Electron Microscopy: A Textbook for Materials Science*, Springer, New York, Ch. 37, pp. 679–681.

Winterbon, K. B., Sigmund, P., & Sanders, J. B. (1970). Spatial distribution of energy deposited by atomic particles in elastic collisions, *Matematisk-fysiske Meddelelser Danske Videnskabernes Selskab,* 37(14) 1–73.

Wood, R. (2009). Future hard disk drive systems. *Journal of magnetism and magnetic materials*, *321*(6), 555-561.

Wu, J. B., Chang, J. J., Li, M. Y., Leu, M. S., & Li, A. K. (2007). Characterization of diamond-like carbon coatings prepared by pulsed bias cathodic vacuum arc deposition. *Thin Solid Films*, *516*(2), 243-247.

Xu, S., Tay, B. K., Tan, H. S., Zhong, L., Tu, Y. Q., Silva, S. R. P., & Milne, W. I. (1996). Properties of carbon ion deposited tetrahedral amorphous carbon films as a function of ion energy. *Journal of applied physics*, *79*(9), 7234-7240.

Yamamura, Y., Matsunami, N., & Itoh, N. (1983). Theoretical studies on an empirical formula for sputtering yield at normal incidence. *Radiation Effects*,*71*(1-2), 65-86.

Yasui, N., Inaba, H., Furusawa, K., Saito, M., & Ohtake, N. (2009). Characterization of head overcoat for 1 Tb/in^2 magnetic recording. *Magnetics, IEEE Transactions on*, *45*(2), 805-809.

Yuan, Z. M., Liu, B., Zhou, T., Goh, C. K., Ong, C. L., Cheong, C. M., & Wang, L. (2009). Perspectives of magnetic recording system at 10 Tb/in^2. *Magnetics, IEEE Transactions on*, *45*(11), 5038-5043.

Zeng, Z. M., Tian, X. B., Kwok, T. K., Tang, B. Y., Fung, M. K., & Chu, P. K. (2000). Effects of plasma excitation power, sample bias, and duty cycle on the structure and surface properties of amorphous carbon thin films fabricated on AISI440 steel by plasma immersion ion implantation. *Journal of Vacuum Science & Technology A*, *18*(5), 2164-2168.

Zhang, H. S., & Komvopoulos, K. (2008). Direct-current cathodic vacuum arc system with magnetic-field mechanism for plasma stabilization. *Review of scientific instruments*, *79*(7), 073905(1-7).

Zhang, H. S., & Komvopoulos, K. (2009). Synthesis of ultrathin carbon films by direct current filtered cathodic vacuum arc. *Journal of Applied Physics*, *105*(8), 3305(1-7).

Zhang, P., Tay, B. K., Sun, C. Q., & Lau, S. P. (2002). Microstructure and mechanical properties of nanocomposite amorphous carbon films. *Journal of Vacuum Science & Technology A*, *20*(4), 1390-1394.

Zhong, M., Zhang, C., Luo, J., & Lu, X. (2009). The protective properties of ultra-thin diamond like carbon films for high density magnetic storage devices. *Applied Surface Science*, *256*(1), 322-328.

Zhu, J., Han, J., Han, X., Schlaberg, H. I., & Wang, J. (2008). sp^3-rich deposition conditions and growth mechanism of tetrahedral amorphous carbon films deposited using filtered arc. *Journal of Applied Physics*, *104*(1), 013512(1-9).